Doctoral Dissertation
Doctoral Program in Metrology (33rd cycle)

Optical Fiber Sensors for Water Quality Monitoring

Andon Bano
* * * * * *

Supervisors
Prof. Perrone G., Supervisor
Prof. Vallan A., Co-supervisor

Doctoral Examination Committee:
Prof. Tosi D., Referee, Nazarbayev University
Prof. Blanc W., Referee, University of Côte d'Azur

Politecnico di Torino
October, 2020

I hereby declare that, the contents and organization of this dissertation constitute my own original work and does not compromise in any way the rights of third parties, including those relating to the security of personal data.

. . . . . .

Andon Bano

Turin, October, 2020

Summary

Clean water and sanitation is one of the 17 sustainable development goals set by United Nations in 2015, to be achieved within 2030. It is a problem that affects around half of the global population causing millions of deaths every year, and predicted to further worsen in the future without immediate interventions.This thesis investigates the possibility of exploiting optical fiber based sensors for real time continuous monitoring of water for the early detection of the onset of contaminants, especially focusing on low cost solutions to try to give a hand to solve the actual critical situation in low-income countries.

Optical fiber sensing techniques are well known for their advantages such as small dimensions, immunity to electro-magnetic fields and robustness to harsh environments; moreover they are able to perform real time analysis with remote interrogation and in a distributed way. All these advantages made them quite popular within the scientific community for more than two decades and lately they are receiving increasing attention also for real world applications. Therefore we thought of applying these benefits in a widely spread still open problem such as potable water quality analysis. With the advancements in the telecommunication field, today optical based setups can be deployed at relatively low costs, enabling the technology to reach even remote communities where there is no continuous water distribution, and regular quality checks are not easy.

In particular this thesis is a study of the viability of refractive index analysis of water as a fast quality check issuing instant warning should deviations occur from the normal situation. For this purpose an optical fiber sensing approach based surface plasmon resonance has been exploited as refractometer because such technique allows achieving very high sensitivity and low limit of detection, in principle capable to sense part per million (ppm) modifications in the water composition. Refractive index changes, however, are not enough for potable water monitoring in situations where the water distribution system is old and degraded. Therefore, in conjunction with the refractometer the proof of concept of a novel fiber based sensor is presented to sense the temperature and the velocity of a flowing fluid exploiting a configuration similar to that of conventional hot wire anemometers.

The obtained results show that optical fibers represent an excellent technological platform for widely deployable water quality monitoring solutions, but also that further research and improvements are necessary before actual system can be installed as routine procedures in water distribution and treatment plants.

Acknowledgements

The aim of this dissertation is to sum up the work and the results obtain during the three years of my Ph.D. career, nevertheless I want it to serve as a lifelong positive memory of this period of my life as well. I feel grateful to all the people that have been around me during this period, definitely they have been the ones who made everything more beautiful and full of life.

I would like to start by thanking my professor Guido Perrone, who gave me the opportunity to work with him, supported me in every step of this long path and made me feel free and independent on guiding my own project. Now that I am in the end of this journey, I have only positive memories coming to my mind out of this collaboration.

Definitely, I would like to thank Prof. Alberto Vallan and Dr. Massimo Olivero who have been my co-supervisors and have made everything to make me feel home working in their laboratories. Together with Guido they have always been there sharing their knowledge, giving me technical support and advices. I feel just gratitude and respect for the dedication you showed in your work day to day. Special thanks also go to Giancarlo Meneghini who helped me every time I went to prepare my sensors in Prima Electro.

I would like to thank every other person with whom our careers and thus our lives have crossed in the laboratories, offices, or even corridors of the Politecnico and what I am used to call Boella (previously Instituto Superiore Mario Boella, now Links Foundation). I would mention Giuseppe Franco, Antonio Nespola, Stefano Straullu, Nadia Boetti, Silvio Abrate, Valerio Miot, Sergio Perero, Luca Bertignono, with whom I have shared the working space at Boella every day. I would also mention all the master's students and short term researchers which have come and left while I have remained there witnessing their final step towards becoming engineers. Andrea Mereu, Albert Rama, Franceso Bozzi, Manuel Maggio, Viviana Cennamo, Vittorio Graglia, Michele Trotta, Alessandra Beccaria, Aurora Bellone, Eduardo Puleo, Francesco Ridolfi, Adem Hoxha, Laert Xhembulla; I am talking about you

with whom I shared laboratories, projects and even lunches in mensa. I would mention also Alessandro Mirigaldi, Valentina Serafini and Martina Riva which in this case are remaining while I am leaving before them. I'd like to thank also Riccardo Gassino and Enkeleda Balliu who have shared their advanced experiences with me and have had nice chats; Alessio Atzori and Prof. Alessio Carrullo with whom we have shared nice coffee breaks and unforgettable dinners.

The Ph.D. has given me opportunities to participate in several external courses and conferences and events where I have created friendships and networks hoping that our life will make us meet and be nostalgic once again in the future. I would mention the people I met at "Gorini School" organized by prof. Pasquale Arpaia and Umberto Cesaro, Abbas Ghaderi, Leila Es Sebar, Alessio Gullino, Alessandro Mingotta, Ruben Crispino etc. People I met at School of Biosensors in Naples, Giovanni Gallo, Gennaro Sanitá and Giulia Paiardi, and people I met in Washington DC Rosy Lawandi and Theodoros Bouloumis. I want to mention also a lot of people I met during the course "Innovation for Change"; the course was long and I created a connection with everybody, however I am mentioning only some of them, Francesco Giordano, Noemi Glisoni, Giovanni Bugnotto, Luca Pasqualone, Gabriele Basso, Giulia Zoppi, Edoardo Degli Innocenti, Sina Famouri, Raphael Sanchez etc. I will definitely want to remember the activities we have carried out with the OSA student Chapter and the people involved in those activities starting with Prof. Andrea Carena, and continuing with Alessio Ferrari, Ann Margareth Rosa Brusin, Emanuele Virgillito etc.

It seems that I can go on forever mentioning names of people I feel grateful and whose names I wish I will remember forever, despite my terrible memory. I could already notice that I had difficulties remembering some names, and I am sure I have forgotten someone, however I sincerely would like to remember and thank everyone with whom I have met because of my Ph.D. and I have exchanged some words during this period. I would also like to thank Lulezim, the Albanian man working as a cashier at CERN, who probably will never read this thesis, nevertheless I really wish to meet him anytime in the future again.

Now I want to shift the attention to the people who I have known or would have known anyways despite of my career. These are the people who have been there and have given the most important and the most beautiful support, they have shared their time, their love, they have cared, thus we have shared our lives together.

I will start to mention the list of friends that have accompanied me in Torino with whom we have had great times hanging out, playing and drinking continuously. Starting with the Albanian community Redon, Jona, Ermal, Lavdie, Rubin, Sara, Andi, Ira, Adem, Verena; I would say you can take the Albanians out of

Albania, but not the Albania out of the Albanians. The international community Lucas, Lalla, Bersy, Mohamed, Enrico, Rosy, Nadia, Jose, Ahmedino, Julio, Fued, Filippo, to them this thesis does not make sense, unless water is replaced by alcohol. The Egyptian gang Samy, Yousry, Shazly, Shady, Salem, Faisal, Suly, Honda, Amgad etc who have relative time concept. And finally, the football guys: Lao, Berti, Ledjus, Renato, Roxhers, Marsel, Gjergji, Klodi, Juan, Ilir, Igli1, Igli2, Orkid, Kevin, Albi, Flori etc. with whom I stayed in shape during this period.

I feel grateful for my family in every moment of my life, and surely I feel thankful to them especially during this period. They have been always there for me to give me the most genuine advices, looking for my best options, wishing for my best future. I thank you for your existence. What you have taught me will never be reached by any education I will ever get.

I want to close this letter with a dedication to the most special person that has been around me and within me during all this period. I cannot find the correct words to thank you for all the dedication, patience, care, happiness, motivation and support you have given to me. You have been my girlfriend, my friend, my comedy actor, my babysitter, my chef, my dance teacher, my shoulder angel, my secretary, my everything. Thank you for being with me. I feel loved and I love you.

Yours Sincerely,
Andon Bano
October 2020

Contents

List of Tables XI

List of Figures XII

List of Acronyms XV

1 Introduction 1

2 Theoretical Background 7
2.1 Surface Plasmon Resonance - SPR . . . 8
2.2 SPR as a Sensing Principle . . . 12
2.3 Optical Fiber Based SPR . . . 13
2.3.1 Fiber Modifications . . . 15
2.3.2 Transmission vs. Reflection . . . 17
2.3.3 Wavelength, Intensity, Angle or Phase . . . 19

3 Mathematical Model and Simulations 23
3.1 Mathematical and Physical Approach . . . 23
3.2 Design and Quality Parameters . . . 27
3.3 Simulation Results and Discussions . . . 30
3.4 Novel Five - Layer Design . . . 33

4 Experimental Work and Results 37
4.1 OFSPR Wavelength Interrogation . . . 37
4.1.1 Characterization of a Sensor in Wavelength Interrogation . . . 40
4.1.2 Stability Analysis . . . 45
4.2 OFSPR Intensity Interrogation . . . 50
4.2.1 Stability Analysis . . . 53
4.3 Middle Range Setup . . . 55

5 SMS Optical Fiber Sensors 61
5.1 Theoretical Background . . . 61
5.1.1 Interference . . . 63

5.1.2 Optical Fiber - Modes - V Number 63
5.2 Simulations 65
5.3 Experiments 68
5.3.1 Simulations Vs Experiments 68
5.3.2 Temperature Characterization 69
5.3.3 OF SMS Anemometer 70

6 Conclusions 73

A OFSPR Sensor Preparation 77

B Sensors' Characteristics 81

C MATLAB Functions 87

Bibliography 93

List of Tables

3.1 Sensor design parameters taken into consideration during simulations. 28
3.2 Design parameters of the sensors and characteristics of their respective SPR curves for the sensors with best performance according to each quality defining parameter. 32
3.3 Sensor design parameters considered during the simulations for the five-layer structure. 34
3.4 Impact of silica thickness on the sensor with the best performance. . 35
4.1 Properties of the curves plotted in Fig. 4.7. Metrological characterization. 44
4.2 Characteristics of the simulated sensor, with the same design parameters as the experimental one. 45
4.3 Experimental and simulated results of the PD array for 4 water-isopropanol solutions, RI = [1.333 1.3373 1.3416 1.3502] 58
5.1 Pump laser power and the respective temperatures of the MM fiber section. 71
6.1 Summary of OFSPR setup configurations; cost - performance analysis 74
B.1 Characteristics of 12 sensors prepared on 400 micron core fiber. . . 81

List of Figures

2.1 Wave vector of light propagating in water (green solid line) and wave vector of an SPW at the gold-water interface (red dashed line). . . 10
2.2 Wave vector of light propagating in water (green solid line); wave vector of light propagating in glass (blue dotted line); wave vector of an SPW at the gold-water interface (red dashed line). 11
2.3 Illustration of Kretschmann configuration (left) and Otto configuration (right) 12
2.4 Illustration of SPR curves obtained from angular and spectral interrogation. ($n_1 < n_2$) 14
2.5 Schematic illustration of the numerical aperture and the acceptance cone of an optical fiber. 14
2.6 Schematic illustration of a tapered SM fiber (top) and a D-shaped fiber bottom 17
2.7 Schematic illustration of a TFBG (tilted fiber Bragg grating) SPR sensor (top) and a hetero-structure (MM-SM-MM) SPR sensor (bottom) 18
2.8 Schematic illustration of a transmission based OFSPR sensor 18
2.9 Schematic illustration of a reflection based OFSPR sensor 19
2.10 Graphic illustration of the intensity interrogation principle. 20
3.1 Schematic illustration of the simulated three layered structure. . . . 24
3.2 Schematic illustration of the simulated four layered structure. . . . 25
3.3 SPR curve parameters illustrated. Depth of the curve, shift in resonance wavelength and the FWHM. 29
3.4 Simulated SPR plot of the sensor which performs the best in terms of DA (Top), FOM (middle) and QP (bottom); water (n=1.33) blue solid line, n=1.34 red dashed line 31
3.5 Comparison among the best FOM curve (red dashed line), the best DA curve (blue solid line) and the best QP curve (green line). All curves are simulated in a situation where the sensor is immersed in water (n=1.33). 33
3.6 Schematic illustration of a 5-layered structure. A silica nano-layer is added on top of the metal layer. 34

3.7 Impact of the silica layer on the SPR curve of the best QP sensor. 35
3.8 DA,FOM and QP of all the designed sensors. 36
4.1 Schematic illustration of non uniformly deposited metal layers (out of scale). 38
4.2 Screenshot of the Avasoft (the software of the Avantes spectrometer used to measure the spectral response) while plotting an SPR curve of a sensor immersed in water. 39
4.3 Setup of the wavelength interrogation system. 39
4.4 Example of a raw spectrum and the second degree polynomial fitted curve. Same spectrum show in Fig. 4.2. 41
4.5 SPR peak for different refractive index values obtained from different water and isopropanol mixtures. 42
4.6 Relatively long term (23 minutes) sensor characterization tests for different RI values. Water (n=1.333); 10% Isopropanol (n = 1.3373); 20% Isopropanol (n= 1.3416); 40% Isopropanol (n= 1.3502); each interval lasted approximately 5 minutes. 43
4.7 Experimental spectra and the respective 2^{nd} order polynomial fit of 4 different refractive indices. RI = [1.333 1.3373 1.3416 1.3502] from left to right. 44
4.8 Three day stability test using the wavelength interrogation technique: blue solid line is for raw data, while the red solid line is for the filtered data. 46
4.9 Temperature and SPR progress with respect to time during the three day stability test. 47
4.10 Normalized spectrum of the broadband LED for three different temperatures, respectively 25 °C, 30 °C, and 35 °C. 48
4.11 SPR curves while the sensor is immersed in water changing temperature in the range of 20 °C to 60 °C. 49
4.12 Electronic circuit schematics of the LED current driver 50
4.13 Photo of the intensiometric OFSPR device including the LED, PD, thermistor and the circuitry in a compact design. 51
4.14 Four SPR spectra with the respective 2nd polynomial fitting; LED at 700 nm simulated and experimental spectrum. 51
4.15 Characterization of the OFSPR in intensity interrogation for 3 different RI values (1.333, 1.3438, and 1.3545); test duration 1 hour; the red box shows a 1 minute zoom in. 52
4.16 Two day stability test of an intensiometric sensor immersed in a 50% concentrated Isopropanol/water mixture; the blue solid line is for the signal output, while the red dashed line is for the liquid temperature. 53
4.17 Output signal with respect to liquid temperature, during a 2 day test. 54

4.18 Spectral positioning of photodiodes, and LED spectrum (Graph); and spatial positioning in the photodiode array (bottom-left corner)[taken from the data sheet of manufacturer]. 56
4.19 Spectral positioning of photodiodes with respect to SPR curves obtained experimentally. 57
4.20 Normalized intensity of R (610 nm) and S (660 nm) over a 20 min characterization test with the sensor immersed in 4 different solutions. 59
5.1 Schematic illustration of a Mach-Zehnder Interferometer (left) and a SMS fiber interferometer (right). 62
5.2 Propagation constant β with respect to V number for the first 4 modes [48]. 64
5.3 Schematic illustration of an SMS sensor. 65
5.4 V number of the considered fibers with respect to wavelength. . . . 66
5.5 Interference pattern with respect to splicing offset, logarithmic scale. 67
5.6 Interference pattern for different MM fiber lengths, 1, 3, 6 and 12 cm. 68
5.7 FSR with respect to $1/L$ MM section length, theoretical - blue squares, experimental red crosses 69
5.8 Interference pattern and temperature dependence of a SMS sensor with 6 cm of MM section. 70
5.9 Schematic illustration of the OF SMS based hot wire anemometer. . 71
5.10 Graphic illustration of the interference pattern shift when exposed to air flow. 72
A.1 Coating and Cladding removal of a 400 micron core fiber 78
A.2 Photos taken before the deposition process 79
A.3 Schematic illustration of the non uniform deposited metal layers (out of scale). 80
A.4 Photo of the sensitive are of a OFSPR sensor produced on a 400 micron core fiber. 80
B.1 Experimentally obtained SPR curves of 4 different sensors while immersed in water and isopropanol. 83
B.2 Experimentally obtained SPR curves of 4 different sensors while immersed in water and isopropanol. 84
B.3 Experimentally obtained SPR curves of 4 different sensors while immersed in water and isopropanol. 85

Acronyms

ADC Analog to Digital Converter.

DA Detection Accuracy.

FBG Fiber Bragg Grating.

FOM Figure of Merit.

FSR Free Spectral Range.

FWHM Full Width at Half Maximum.

I2C Inter-Integrated Circuit.

LED Light Emitting Diode.

MM Multi Mode.

MZI Mach-Zehnder Interferometer.

NA Numerical Aperture.

NIR Near Infra-Red.

OF Optical Fiber.

OFSPR Optical Fiber Surface Plasmon Resonance.

OSA Optical Spectrum Analyzer.

PD Photo-Diode.

POF Plastic Optical Fiber.

QCM Quartz crystal Micro-Balance.

QP Quality Parameter.

RI Refractive Index.

RIU Refractive Index Unit.

SDG Sustainable Development Goal.

SM Single Mode.

SP Surface Plasma.

SPI Serial Peripheral Interface.

SPP Surface Plasmon Polariton.

SPR Surface Plasmon Resonance.

SPW Surface Plasma Wave.

TECS Technology Enhanced Clad Silica.

TFBG Tilted Fiber Bragg Grating.

TM Transverse Magnetic.

TRL Technology Readiness Level.

UN United Nations.

WHO World Health Organization.

Chapter 1

Introduction

"A clear liquid, without colour or taste, that falls from the sky as rain and is necessary for animal and plant life" - **Cambridge Dictionary**

"A liquid without colour, smell or taste that falls as rain, is in lakes, rivers and seas, and is used for drinking, washing, etc." - **Oxford Dictionary**

These are the definitions of **water** according to the two main English language dictionaries, Cambridge and Oxford. Yet water in our lives is much more than that. Even though 75% of the Earth's surface is covered with water, only 3% of that water can be used for our lives. In 2015 United Nations (UN) have prepared a list of 17 Sustainable Development Goals (SDGs) to be achieved within 2030 and "Clean Water and Sanitation" is the sixth (SDG6); actually, almost all the other 16 goals are somehow directly or indirectly related to water. For instance, *SDG2, Zero Hunger* and *SDG3, Good Health and Well-being* are directly related to the access to clean waters.

It is clear that the World needs to develop in a sustainable way, as facts show that Earth resources are not limitless, quite the opposite they are limited and require to be taken care of. Water is one of those resources, which, while for most of us is almost taken for granted and quite often misused, for under-developed and developing Countries it might even be considered a luxury. Indeed, ensuring availability and sustainable management of water and sanitation for all is the objective of the cited SDG6. As a matter of fact, 2.2 billion people lack access to safely managed drinking water services, while over half of the global population – 4.2 billion people – lacks safely managed sanitation services. Among these people, 297,000 children under five die every year from diarrhoeal diseases due to poor sanitation, poor hygiene, or unsafe drinking water [1]. These numbers are outrageous and call for immediate action: five years have already passed since the sustainable goals have been set and a lot of work has to be done in the next ten years in order for the SDG6 to be considered a success before the deadline.

The lack of water is not the only problem people are facing as most of them (more than half of the world population) lack water quality assurance. Quality is a relative parameter, which needs to be quantified according to the specific application. For instance, when considering industrial cases, the focus is mainly on the waste waters released in the environment and how they are impacting the global water management. But, when it comes to human consumption, the quality is a much more important concept than in agricultural and industrial applications, which also goes beyond the mere "safe for drinking" level. However, notwithstanding this, the use policies and the treatment and quality assurance processes are typically managed by local communities, often with few rules in common. In particular, much of the water quality depends on the choices made by the local institutions, the communities and sometimes also by the final consumers at their houses. As a result, local institutions analyze water periodically but there is no unique global agreement, likewise no database of the water quality and treatment worldwide [2]. Actually, the World Health Organization (WHO) has released guidelines for the drinking water quality, but it is the responsibility of local authorities to follow such guidelines [3].

It is important at this point to briefly analyze how the water quality management process works. In order to ensure the quality of the distributed water, water is periodically sampled in different parts of the distributing system and transported to the laboratory, where tests are performed and data are analyzed. Sampling and transportation are quite critical parts because it must be guaranteed that the sample represents the water it was taken from, maintaining at least the specific properties that are supposed to be analyzed. The most common tests are chemical (heavy metal ion concentration, ammonia, chloride etc.), bacteriological, radiological and acceptability (odor, taste, color) analyses. This at least in highly developed Countries. But, what about Countries or areas in which the water distribution system is not well established? Where there is no continuous water supply, or where the network has losses (leakage) and abusive intrusions? These distribution systems are characterized by unexpected events that interrupt the water flow or introduce contaminations. In such cases the authorities can ensure the quality of water only at some key points of the system, but it is impossible to guarantee the quality at the final consumer. Considering the random variations typical of discontinuous service cases, sampling and analyzing periodically does not help and the tragic numbers regarding the diseases and deaths caused by contaminated water reported before confirm the critical importance of ensuring a constant water quality. The optimal solution to these problem would be to monitor the water quality in real time and in a distributed way to inform the population in case of hazardous circumstances. However, this would require a lot of low cost devices, suitable for being installed as close to the final consumer as possible, ideally in each house.

Refractive Index - Universal Parameter

At first sight it looks quite impossible to analyze water quality in a distributed manner and in real time. Of course, it is not feasible if one aims to quantify the same amount of parameters of traditional analyses carried out in laboratories, but it becomes a realist goal if some simplifications are introduced. In this spirit, this dissertation discusses the first steps towards a real time water quality monitoring device suitable for wide deployment, which is based on the continuous monitoring of the water Refractive Index (RI). The RI is a dimensionless quantity that quantifies the reduction of the propagation speed of light in a dielectric and that defines the behavior of a light beam at the interface between two dielectrics (refraction). Given the dependence on the material composition and its physical properties, the RI is a parameter well suited to sense any chemical or physical modification in the material composition. For instance, 1 ppm of chlorine would increase the water RI by approximately 1×10^{-4} while an increase of 1 °C of the temperature would decrease it by about -1×10^{-4} [4, 5]. The refractive index can be measured using refractometers. The first refractometer has been designed by Ernst Abbe and produced by Carl Zeiss at the end of the 19th century and since then it has found numerous applications in different fields [6]. Most of the modern prism based refractometers still exploit the same principle (critical angle determination) as Abbe's refractometer.

In this work we will present an optical fiber based refractometer able to perform continuous real time monitoring. We believe that exceptional features of optical fibers perfectly go along with the water analysis application. It is clear that a single sensor, regardless of its performance, will not be able to compete with the results obtainable through the long procedure of water quality lab tests. Nevertheless, we believe that a real time, high efficient refractometer can be a companion (non a substitute) to the other existing test procedures in developed Countries, but it becomes a necessary low cost "rising alert" instrument where other regular tests are impossible to be done, such as in under developed Countries. Optical fibers have some really outstanding properties, which make them the best option when it comes to minimally invasive, real time and in harsh environment measurements: they are small size, immune to electromagnetic disturbances, resistant to extreme temperatures, and moreover have a relatively low per unit cost.

The proposed fiber-based refractometer exploits a well known physical phenomenon called the "Surface Plasmon Resonance" (SPR) because it allows higher sensitivity and resolution with respect to other configurations with similar applications. The largest part of this work is focused on the characterization of the SPR

phenomenon in metrological terms. Along the chapters we will try to answer some questions we thought are really relevant in order to know better the system and possibly bring it one step closer to a commercial level. - Is the phenomenon really that sensitive as the theory suggests? - What are the factors that determine its detection limits? - How does the sensor behave in long term tests? - Is it suitable to perform continuous real time measurements? - Which are the weak points that need to be overcome?

Temperature and Flow Rate

The plasmonic Optical Fiber (OF) refractometer needs to be temperature compensated. Therefore, in order to have a fully optical setup we have studied possible OF based thermometers. Apart from the compensation necessity of the plasmonic sensor, temperature is a very important parameter for the potable water. Long exposure to high temperatures favors micro-biological flora, creating optimal conditions for undesired bacteria; thus a real time temperature monitoring of the water is always welcomed. In this thesis we present an SMS (single mode - multi mode - single mode) OF sensor that exploits the interference between the first two propagating modes in a short multi-mode fiber section, obtaining a device with sensitivity five times higher than that of Fiber Bragg Gratings (FBGs), the most common OF based temperature sensors. Furthermore, with slight modifications on the configuration setup, the device can be used as a flow meter with a working principle similar to that of the hot wire anemometer. Again, knowing the real time flow rate or velocity of the flowing water in the distribution system would be very useful, especially in the cases where the distribution system has undergone interventions, might have losses, or has interruptions. However, the study of the flow sensor is limited to a proof of concept level, limiting the tests at constant air flow to prove the anemometer concept.

Thesis Outline

After this brief introduction focused on the motivation and the scope of this work, the dissertation will continue with **Ch. 2**, covering a short theoretical background of the SPR phenomenon and how it is implemented in optical fiber setups, with a discussion of the most common configurations. Then **Ch. 3** is focused on the mathematical model of the SPR phenomenon and on the simulation to optimize the different configurations. **Ch. 4** describes the main aspects of experimental work, which is aimed mainly at characterizing the OF SPR (OFSPR) sensors in different configurations, making a cost-performance analysis. **Ch. 5** is dedicated to the work regarding the SMS (single mode - multi mode - single mode) optical fiber sensor exploited as an hot wire anemometer to measure the flow rate of fluids.

The chapter covers the full topic, starting with a brief theoretical explanation of the phenomenon, continuing with the simulations done in Matlab and ends with the experimental work and results. The thesis concludes with **Ch. 6**, a short recap deducting the main aspects of this project and what the reader should keep in mind in case of interest to develop further the project.

In the appendices the reader can find valuable information about: i) the sensor fabrication process (**Appendix A**) and the key aspects that need to be taken in consideration in case the procedure needs to be replicated or improved in the future; ii) the fabricated sensors experimental characteristics and SPR curves (**Appendix B**); iii) the most important Matlab codes developed for the simulations of the OFSPR sensors (**Appendix C**).

Chapter 2

Theoretical Background

The physical principle of light confinement was proved in the XIX century by Jean-Daniel Colladon and John Tyndall, who experimentally demonstrated the total internal reflection of light within a water stream in air [7, 8]. The same principle was later exploited to confine light in glass rods, which then evolved into the Optical Fibers (OFs). Early fibers were used for illumination and decoration purposes only due to the very high propagation losses; then, when the attenuation decreased down to less than 20 dB/km, as predicted by Charles K. Kao and George A. Hockham (1965) [9] the great epic of telecommunications started. From that moment on, the optical fiber technology has progressed exponentially and nowadays the state of the art of the attenuation in optical fibers is 0.17 dB/km (almost in the theoretical limit), making optical fibers the leading technology in the telecommunications field [10].

Parallel with the communication capabilities, OFs have shown great capacity in sensing applications, as their peculiar characteristics make them the favorable option in many fields, where other sensing principles would be hard to be applied. One of the main features of the OFs, making them a perfect option for sensing, is their small dimension, which is particularly suitable for the minimal invasive impact and in-situ measurements. Another very important property of the Optical Fiber Sensors (OFSs) is the electromagnetic immunity, since this feature gives OFs an advantage with respect to metal or semiconductor based sensors. Moreover, fiber sensors are generally characterized by their high sensitivity, excellent resolution and robustness for harsh environments. However, until few years ago, OF based sensing has been considered mainly as a research topic, rather than a practical application, due to the high costs. Lately, the advancements in the field of telecommunications have turned that drawback into an advantage since high investments in the technology and mass production have decreased the cost of fibers and of their related components.

OF sensing principles are based on isolating and analyzing the key parameters of a propagating light, being that transmitted, reflected, refracted, absorbed or even scattered. The most common parameters analyzed are the intensity, the wavelength, the polarization, the modes, the angle of propagation and even the time of flight of the propagating light. By correlating any of these parameters of light with a parameter of interest of the surrounding environment, the OF have been used as thermometers [11], strain gauges [12], gyroscopes [13], refractometers [14], accelerometers [15], anemometer [16], molecular sensors [17], pH sensors [18] etc. OF sensors have found numerous applications both in the industrial and in the biomedical fields, with some of the setups already at commercial level and quite popular for certain applications.

As previously mentioned the work presented in this thesis is divided in two main parts, one regarding a plasmonic OF sensor and the other regarding an interferometric OF sensor. This chapter will focus only on the theoretical background of the plasmonic sensor, while the theory of the interferometric sensor will be found in the dedicated Ch. 5. The next section presents the explanation of the involved physical phenomenon; then it is discussed how this physical phenomenon can be implemented as a sensing principle and, finally, the possible and the most common configuration setups for these kinds of sensors are introduced.

2.1 Surface Plasmon Resonance - SPR

The SPR (Surface Plasmon Resonance) phenomenon relies on exciting the surface electrons of a conductive layer (metal, plasma) by a properly polarized light. The surface electrons of the conductive layer when oscillating synchronously create the idea of a surface plasma oscillation that propagates along the surface, which is called a Surface Plasma Wave (SPW). The wave has a range of oscillating frequencies, which if plotted along the frequency (or wavelength most commonly) axis has the shape of a notch filter (dipped curve). The frequency (wavelength) at which the curve exhibits its minimum value is the Surface Plasmon Resonance (SPR) condition. The same phenomenon can also be observed from a quantistic (particle) point of view: the photons of the incident light couple with the electrons of the conductive layer and generate another wave, which has its proper quantum particle called Surface Plasmon Polariton (SPP).

Although we can discuss about quantum particles and quantum phenomena, the full theoretical and analytical background of the topic can be covered by solving Maxwell's equation at the interface between a metal and dielectric, taking into account the proper boundary conditions. In order for the light wave to be able to transfer some energy to the surface plasma wave, conditions both in terms of energy

and momentum must be matched. Moreover, the plasma wave exists only if the dielectric constants of the materials at the interface match the following conditions [19]:

$$\varepsilon_1(\omega) \cdot \varepsilon_2(\omega) < 0 \tag{2.1}$$

$$\varepsilon_1(\omega) + \varepsilon_2(\omega) < 0 \tag{2.2}$$

where ε_i stands for the dielectric constant of the material. This means that one of the dielectrics must be negative but with an absolute value larger that that of the other. This conditions are clearly satisfied by metals, which are characterized by a large negative real part in contrast to the small imaginary part of dielectrics. The other material can be any dielectric. Nevertheless, considering the above dielectric constants, the wave vector (propagation constant) of the SPW at the interface between a metal and a dielectric, expressed as the left hand side of Eq. 2.3, $k_\mathrm{SP}(\omega) = \frac{\omega}{c}\sqrt{\frac{\varepsilon_\mathrm{m}\cdot\varepsilon_\mathrm{d}}{\varepsilon_\mathrm{m}+\varepsilon_\mathrm{d}}}$, is always larger than the wave vector (propagation constant) of a light beam (of the same wavelength) traveling in the same dielectric; expressed as in the right hand side of Eq. 2.3 $k_\mathrm{light}(\omega) = \frac{\omega}{c}\sqrt{\varepsilon_d}$ [20]:

$$k_\mathrm{SP}(\omega) = \frac{\omega}{c}\sqrt{\frac{\varepsilon_\mathrm{m}\cdot\varepsilon_\mathrm{d}}{\varepsilon_\mathrm{m}+\varepsilon_\mathrm{d}}} \;>\; k_\mathrm{light}(\omega) = \frac{\omega}{c}\sqrt{\varepsilon_\mathrm{d}} \tag{2.3}$$

In other words, this means that the light propagating in a dielectric is not energetic enough to excite a SPW at a metal interface. Fig. 2.1 is the graphic illustration of Eq. 2.3 considering gold (Au) as conductive material and water as the dielectric.

In order for a light beam to be able to excite an SPW, the two curves should have at least one intersection point and this is possible with two different solutions, either the k_SP curve is brought down, or the k_light is brought up. Thus, either the light beam is more energetic and it propagates beforehand in higher refractive index (dielectric constant) material or the SPW is generated at an interface between a metal and a lower Refractive Index (RI) dielectric. In principle we are discussing the same solution, where the light propagates beforehand in a material with higher RI compared to the material where the SPW will be generated, Eq. 2.4:

$$\varepsilon_{\mathrm{d1\ (light)}} > \varepsilon_{\mathrm{d2\ (SPW)}} \tag{2.4}$$

An example where glass is the high refractive index material (roughly 1.45), gold (Au) is the conductive material, and water is the low refractive index material (roughly 1.33) is illustrated in Fig. 2.2. The intersection point between the two curves is at 615 nm. This is precisely the wavelength of the light that in case of an SPW creation will couple energy with the polaritons.

How can this situation be experimentally implemented? The first researchers to observe the SPR phenomenon were Kretschmann and Otto in 1968 with prism

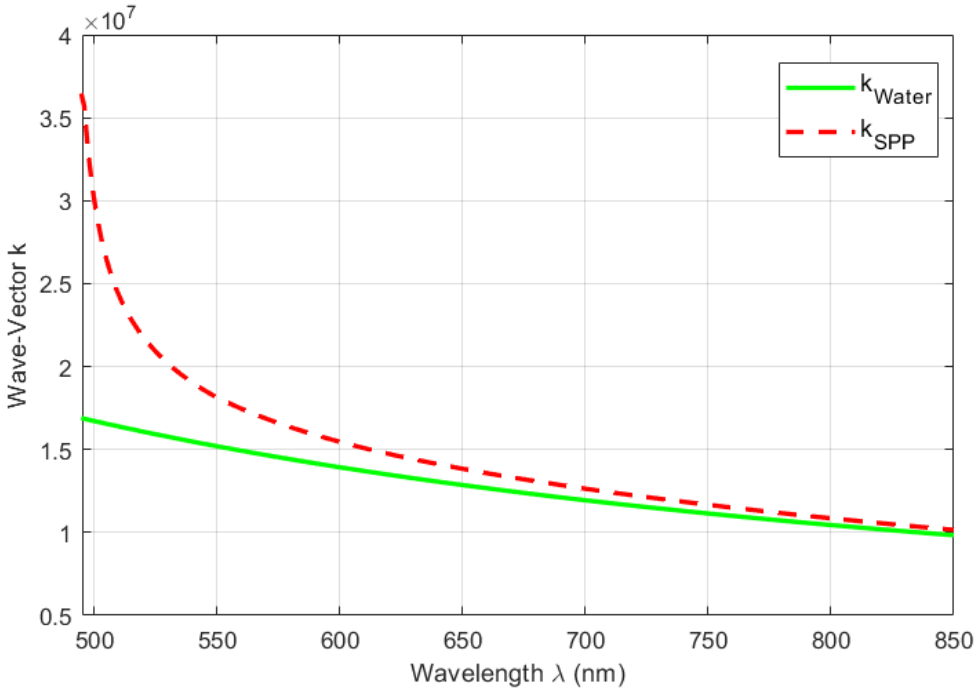

Figure 2.1: Wave vector of light propagating in water (green solid line) and wave vector of an SPW at the gold-water interface (red dashed line).

based setups [21, 22]. The setups are still the most popular even nowadays for sensing applications. Kretschmann configuration consists of a glass prism, with a facet coated by a very thin layer of metal (usually gold, silver or copper) on top of which is placed the other dielectric, such as water. The light beam is firstly coupled to the glass prism; it propagates within the prism and arrives at the glass-metal interface. The metal layer should be thin enough (several nanometers) to allow the electromagnetic field penetrate through the metal and interact with the dielectric on the other side. The incident light is totally reflected except for some wavelength or angular components that are absorbed by the electrons that generate the plasma wave. The main reason why the metal layer needs to be very thin in the Kretschmann configuration is because the thickness needs to be thinner than the penetration depth of the light in the metal, so the SPW can be generated at the metal-water interface. Kretschmann prism based configuration is illustrated in Fig. 2.3 (left).

In the same year, Otto, developed a very similar setup based again on a glass prism, as illustrated in Fig. 2.3 (right). While in the Kretschmann configuration the thickness of the metal layer is a crucial parameter of the setup, the Otto setup avoids such peculiarity. In this case the light propagating in the glass prism, reaches

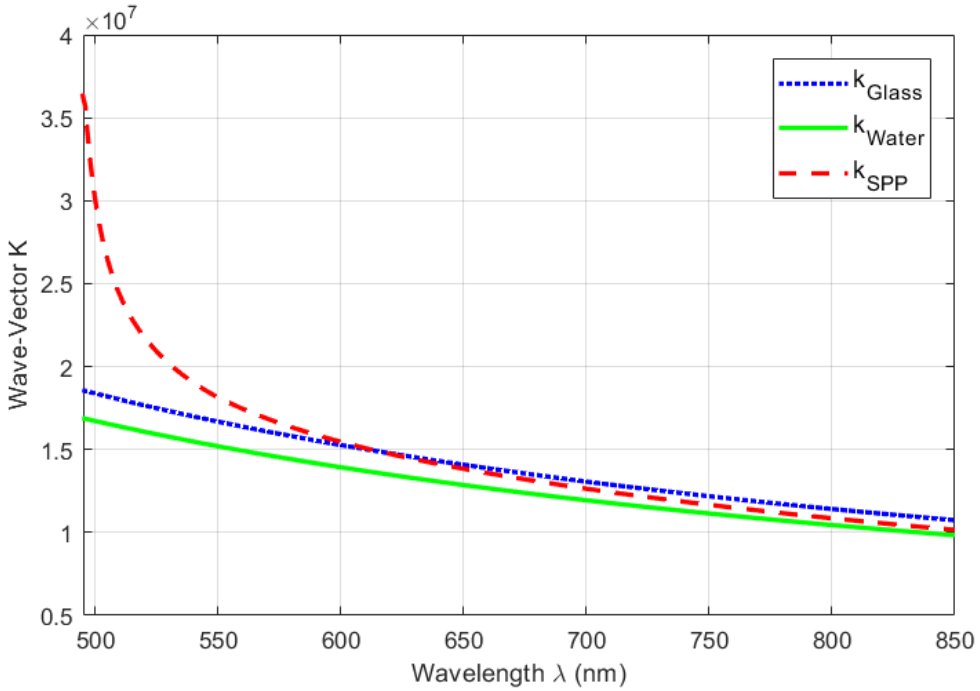

Figure 2.2: Wave vector of light propagating in water (green solid line); wave vector of light propagating in glass (blue dotted line); wave vector of an SPW at the gold-water interface (red dashed line).

the interface between glass and water, and undergoes total internal reflection and the evanescent wave reaches the dielectric (e.g., water)-metal interface where the SPW is generated. Though, the water layer should be thin enough (in the order of hundreds of microns), thinner than the field penetration depth for the evanescent wave to reach the other side of the layer where the metal is laying. This setup is rarely applied in practical applications, because it is quite difficult to guarantee the fixed small distance between the prism and the metal.

As the SPW propagates along the metal surface at the metal-dielectric interface, it naturally has a parallel polarization (p or TM polarization). Keeping in mind the fact that the waves have a vector nature, in order to create matching conditions between two waves, matching just their energy is not enough for the waves to couple. The directions (polarization) of their wave vectors need to be matched as well, thus only parallel polarized light wave can satisfy the conditions to generate a SPW.

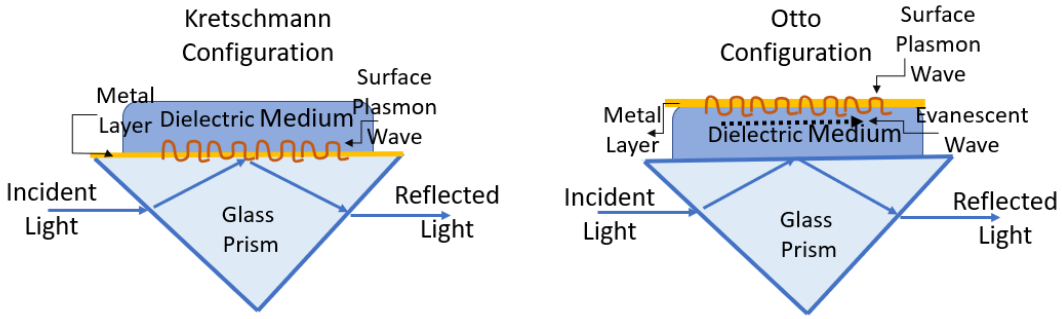

Figure 2.3: Illustration of Kretschmann configuration (left) and Otto configuration (right)

2.2 SPR as a Sensing Principle

In this section the Kretschmann configuration is further analyzed because it is the most commonly used and very similar to the fiber based setup later discussed. Glass is the preferred material for prisms for three main reasons: i) it is a solid, thus a metal layer can be easily deposited on top of it; ii) it is very transparent, thus there are almost no losses due to absorption or scattering; iii) it has a relatively high refractive index with respect to water-based fluids, around 1.5, and this means that the other dielectric can have a wide refractive index ranging from 1 to almost 1.5. As for the conductive layer, several metals have been tested, such as gold (Au), silver (Ag), and copper (Cu). Among the three, silver and gold exhibit the SP resonance wavelength in the visible range. While silver shows a deeper dip (easier to be distinguished), gold has better long term stability because it resists more to external corrosion and oxidation processes [23]. The third material is usually a liquid or a gas, with a refractive index up to that of the glass prism. In sensing applications this is usually the material under test, as the SPR response depends directly on the RI of the dielectric material. Thus SPR sensors can be easily used as refractometers for liquids.

Last but not least, another important parameter is the metal layer thickness, which directly impacts the shape of the SP curve. Studies both experimental and simulations have been done to analyze the impact of the metal layer on the SPR phenomenon [24]. In practice another layer of few nano meters of chromium (Cr) or titanium (Ti) is usually added between the glass substrate and the metal layer for adhesion purpose.

Once the above parameters are decided in accordance with the application and

the performance required, the other variables which impact the SPR phenomenon are accordingly related to the light and to the measurement technique. The two main interrogation techniques used in prism based setups are angular interrogation and wavelength interrogation.

- **Angular interrogation**; the source of light needs to be monochromatic. After getting coupled in the glass prism, the light reaches the metal layer, excites the plasmon polaritons, gets reflected and finally is collected in a photo-diode. The source is mounted on a rotary stage that sweeps all the possible angles, while the photo-diode collects the light. There is an angle for which the transmission reaches its minimum, known as the angle of the resonance for the specific wavelength. That angle shifts directly with respect to the external refractive index.

- **Wavelength interrogation**. In this case the source is a broadband (white) light and does not need a rotating stage to match the wavenumber. In this case the output signal needs to be collected by a spectrometer instead of a simple photo-diode: the wavelength where the curve presents the deepest dip is known as the SPR wavelength, which red-shifts in case of increasing refractive index. Fig. 2.4 illustrates how the SPR curves behave in terms of RI, in angular and wavelength interrogation. When the incident light is properly TM polarized with respect to the metal layer, the reflected light can even reach the 0 level at the resonance condition.

Prism based SPR setups have attracted a large interest for sensing applications since their first appearance and have found many applications particularly in the biomedical field. For example, Biacore AB Corporation was one of the earliest companies to commercialize an SPR based setup in 1990 to measure bio-molecular and protein-protein interactions.

2.3 Optical Fiber Based SPR

This section discusses how SPR sensing can be implemented with optical fibers, the so-called OFSPR sensors. In essence, the glass fiber plays the role of the glass prism in the Kretschmann configuration and thus in a short section of the fiber (few centimeters) the cladding is removed and a metal layer is deposited. The incident light is coupled from one end of the fiber and collected from the other end; the SPR phenomenon occurs at the section where the metal layer is deposited. However, when talking about OFSPR there are some other parameters that have to be considered with respect to prism based SPR, such as the fiber Numerical

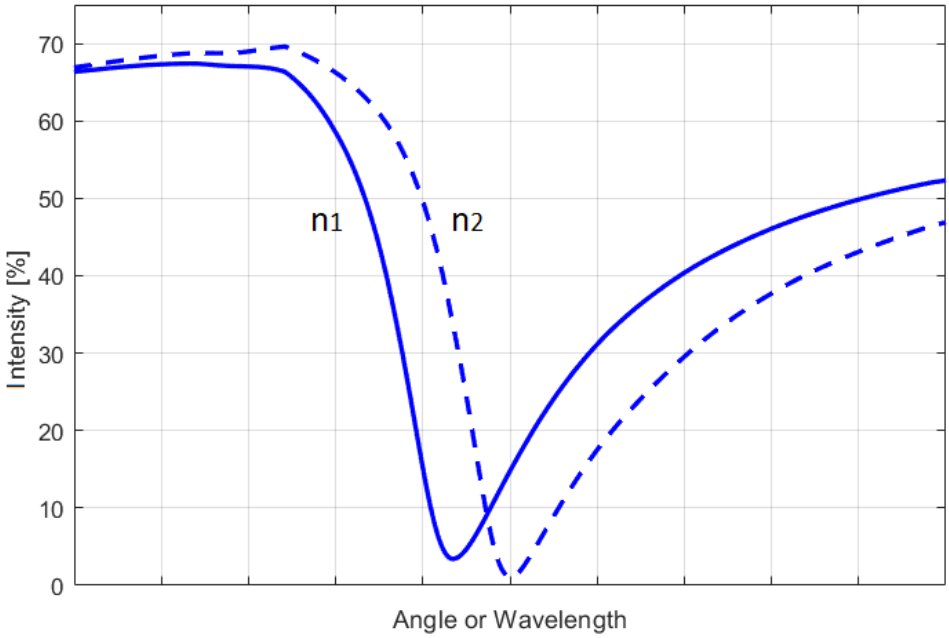

Figure 2.4: Illustration of SPR curves obtained from angular and spectral interrogation. ($n_1 < n_2$)

Aperture (NA). The NA is a dimensionless quantity – expressed as in Eq. 2.5a – that determines the acceptance cone of the fiber as in Eq. 2.5b (graphic illustration in Fig. 2.5), which in turn determines the angles of incidence of the light at the glass - metal interface.

$$\mathrm{NA} = \sqrt{n_{\mathrm{core}}^2 - n_{\mathrm{cladding}}^2} \tag{2.5a}$$

$$\theta_{\mathrm{max}} = \arcsin(\mathrm{NA}) \tag{2.5b}$$

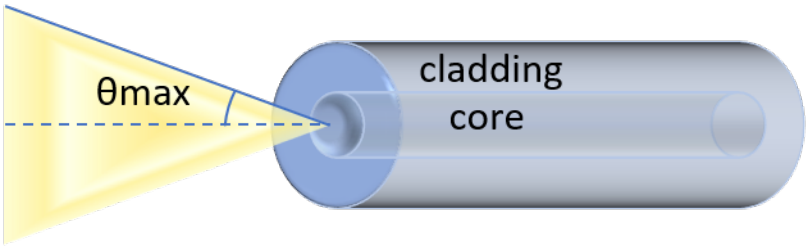

Figure 2.5: Schematic illustration of the numerical aperture and the acceptance cone of an optical fiber.

Typical NA values of commercial Multi-Mode Fibers (MMF) are 0.22, 0.39 and 0.5. An additional important parameter in OFSPRs is the length of the sensitive

area. This parameter was irrelevant in the prism based setup because in that case the light interacts only once with the sensitive area before it is analyzed, but in OFSPR the light can interact several times with the metal layer depending on the sensitive length because of the guiding mechanism of the fiber.

Another difference with the prism based setup is the control of the polarization. Indeed, while in the prism based setup the light could be launched with a well defined polarization, in OFSPRs it is not possible to control the polarization state of light, unless special polarization maintaining fibers are used; moreover, the metal layer has cylindrical shape, thus it does not lay on a single plane and therefore launching of the light with a specific polarization does not play any relevant role. More details about the design parameters of the OFSPR will be discussed in Ch. 3 where the mathematical model will be explained and the results of some simulations will be reported. Bearing in mind these final remarks we can now mention some specifics about the feasibility of the optical fibers for SPR sensing.

2.3.1 Fiber Modifications

A very important aspect to be considered in the case of OF based SPR sensors is the method exploited to allow the interaction between the guided field and the metal layer. Common fibers are designed in such a way that they confine the light within the core, and only a small portion of the field extends in the cladding, being totally negligible after few microns from the the core-cladding boundary. Therefore, just by depositing the metal layer over the cladding, the SPR phenomenon will not occur, because there will not be any significant power reaching the metal layer and capable to excite the polaritons.

This means that the fibers need to be physically modified before being used as substrates for OFSPR sensors. The most common and straightforward method is to unclad the fiber and expose the core for the length of interest. Nevertheless, this method is very difficult for standard Single-Mode Fibers (SMFs) because the core and the cladding are both made of silica and therefore removing the cladding requires etching the silica with hydrofluoric acid (quite a complex procedure that presents relevant safety issues) or precision milling. Besides, SMFs have very small core diameters (around 9 µm) and removing the cladding would pose mechanical stability issues. Even though uncladding the fiber is the most straightforward method, several other methods are exploited to have light interact with the metal layer and excite the SPW. The main reasons why one method is preferred over another, might be the per unit or operational cost, simplicity of operation, repeatability, or even robustness of the sensor. In the following, the main fiber modification techniques are summarized.

- **Fiber uncladding**: despite the difficulties outlined before, removing the cladding is feasible in some large core MMFs with polymeric cladding, such as fibers having a 400 µm or larger core. The uncladding process can be done either by chemical etching (usually acetone) or/and physically by mechanically stripping the fiber. Some authors have used all plastic fibers, the so-called Plastic Optical Fibers (POFs), which are characterized by a large core dimension too, and have chemically etched the cladding until the core is reached or until the evanescent field in the cladding has a relevant amount of energy [25].

- **Waist tapering**: this is an alternative method to etching and consists in reducing the diameter of the fiber for a certain length to extend the evanescent field tails in that section so that the interaction with the metal layer becomes possible [26]. This method is usually exploited for SMFs and is very repeatable, although the resulting sensors becomes more fragile. Fig. 2.6 (top) schematically illustrates a waist-tapered fiber based SPR sensor.

- **Side polishing**: another methodology is to polishing one side of the fiber, hence creating a D-shape [27] characterized by a plane that can be very close to the core of the fiber so that the evanescent field tails can penetrate in the metal layer. The biggest advantage of this technique is the simplification of the metal layer deposition process because it needs to be done only on a flat surface instead of on a cylindrical surface. This method has found application in SMFs, MMFs and POFs and is schematically illustrated in Fig. 2.6 (bottom).

- **Bragg grating assisted coupling**: this approach, which consists in inscribing a tilted Bragg grating in the core of an SMF, allows not modifying the outer structure of the fiber. The tilted Bragg grating reflects the incident light towards the cladding with an angle that is not larger than the critical one, thus it is not totally reflected and some light can escape in the cladding. In this case the metal deposition can be made directly on top of the cladding of the fiber. This method guarantees repeatability and robustness [28]. Moreover, the grating adds an interference pattern to the spectrum of light, which can be used to monitor other parameters, such as the temperature or the strain. A schematic illustration can be seen in Fig. 2.7 (top).

- **Fiber hetero-structure**: last but not least, a very interesting fiber "modification" is to create a sort of "hetero-structure" composed of an SMF sandwiched between two sections of MMFs [29]. The light is coupled to a large core MMF, whose other end is spliced to a small core SMF, obtaining a structure similar to that of the tapering technique. At the MMF-SMF junction a

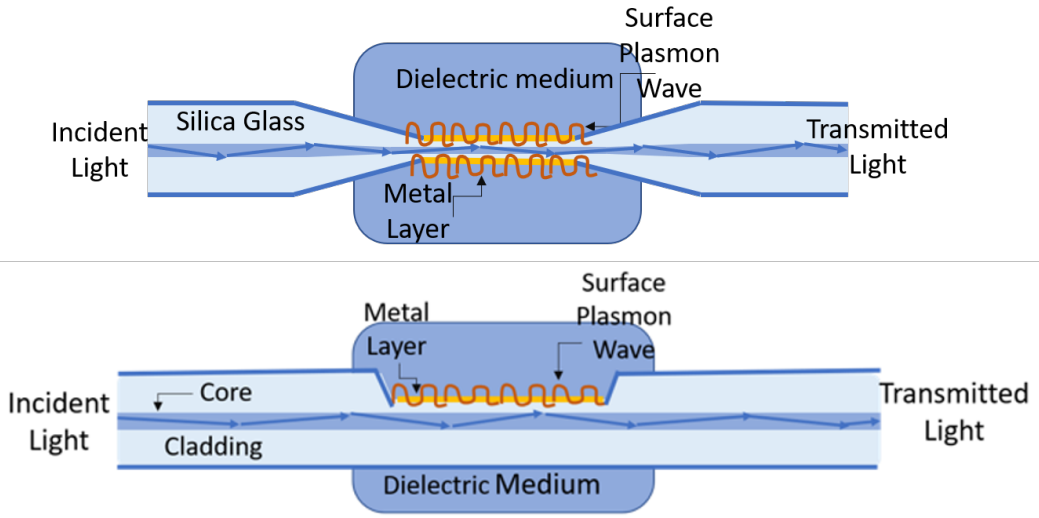

Figure 2.6: Schematic illustration of a tapered SM fiber (top) and a D-shaped fiber bottom

large part of the incident light is coupled into the cladding of the SMF, thus the metal layer can be deposited immediately on top of the cladding with no further needs for modifications. The light is then collected in another large core MM fiber to be further analyzed. In this case the central portion of the fiber does not necessarily need to be an SMF, as it can also be a core-less fiber or a photonic crystal fiber. The hetero-structure schematic is illustrated in Fig. 2.7 (bottom).

2.3.2 Transmission vs. Reflection

Whether the prism based setups can only work in reflection, the OFSPR sensors can be employed both in transmission and reflection, depending on the configuration. Transmission setups are the most straightforward since the are implemented by shining the light on one side of the fiber and collecting it after the SPR has occurred on the other side. Apart from simplicity, which is their major advantage, transmission based setups have some drawbacks. For instance, to use an interrogator that incorporates both the source and the receiver, the output fiber must be bent to be brought back to the input and this requires quite a large footprint because fibers are generally very bending sensitive and a minimal bending radius must be ensured. Another drawback is that the sample to be tested needs to be brought in contact with the sensor, thus the setup can not be comfortably used as a probe for in-situ measurements. However, transmission based setups are the best option for many applications: an example, is the term monitoring of water flowing in a pipe. A schematic illustration of a transmission based OFSPR sensor is shown

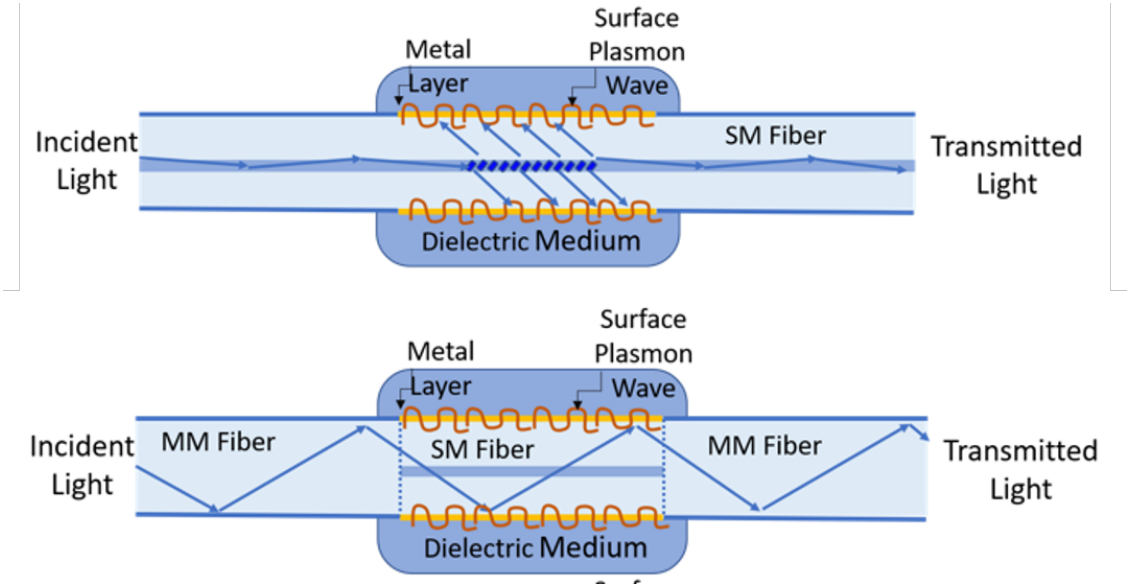

Figure 2.7: Schematic illustration of a TFBG (tilted fiber Bragg grating) SPR sensor (top) and a hetero-structure (MM-SM-MM) SPR sensor (bottom)

in Fig. 2.8

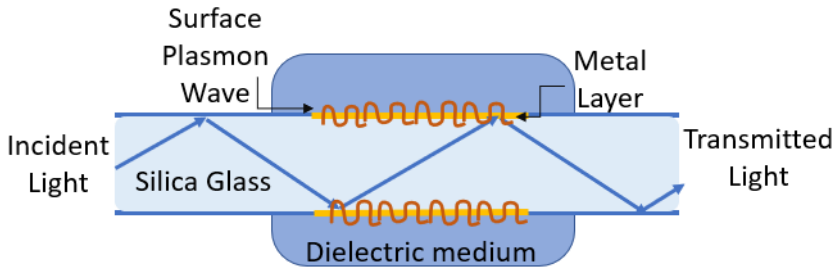

Figure 2.8: Schematic illustration of a transmission based OFSPR sensor

Reflection based sensors are more complex to be fabricated since a micro-mirror needs to be deposited (usually silver) at the end face of the fiber so that the signal comes back at the entrance point. Metal deposition on the end-face of a fiber is not something to be neglected when talking about complexity of a system. In this case, as the source and the collector are both in the same side of the fiber, a 2×1 coupler (or a circulator) is required to separate the signals as well. Although the reflection based setup presents some complications in the physical aspect, it is preferred by the scientist because it can be treated like a tiny probe, which exploits the best feature of the OF, small dimension. Being a probe, such setup is perfect

for in-situ measurements and where the sensor can be brought to the sample and not vice-versa. Fig. 2.9 illustrates a reflection based OFSPR sensor.

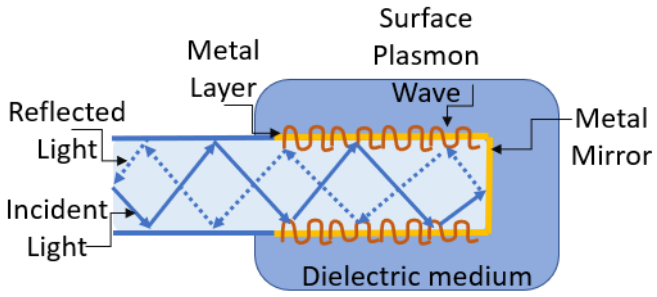

Figure 2.9: Schematic illustration of a reflection based OFSPR sensor

2.3.3 Wavelength, Intensity, Angle or Phase

Similarly to the prism based configuration, the OF based ones can also be categorized with respect to the interrogation method. Typically, OFSPR sensors are interrogated in terms of wavelength and intensity, but some researchers suggest also to interrogate them in terms of angle or phase. Let us start with the wavelength interrogation which is the most common and straightforward one. Likewise the prism based setup also in the fiber based one, the required instruments are a broadband (white) light and a spectrum analyzer or a spectrometer. The SPR dip shifts with respect to the external refractive index, with a red-shift in case of an increase in RI and a blue-shift when RI decreases.
The second most common technique to interrogate OFSPR sensors is the intensity interrogation. In this case, the light source is monochromatic, it can be a colored LED or a laser with the wavelength set in one of the shoulders of the typical SPR curve. On the receiving side it is enough to have a photodiode to monitor the changes in the intensity due to the relative shift between the source emission wavelength and the SPR spectral response. The principle is illustrated graphically in Fig. 2.10. The other two interrogation methods, angular and phase, are not very common in fiber application due to the complexity of the process. Angular interrogation is very common for the prism based application due to the structure of the prism with the metal layer deposited on a flat side. In fiber based setups, the fiber needs to be well fixed, and the result is monitored in intensity while the source is mounted on a rotating stage [30, 31]. Even though in principle this kind of configuration works, it loses all the intrinsic advantages offered by the optical fiber. The instrument becomes bulky, with the same features of the prism based setup.

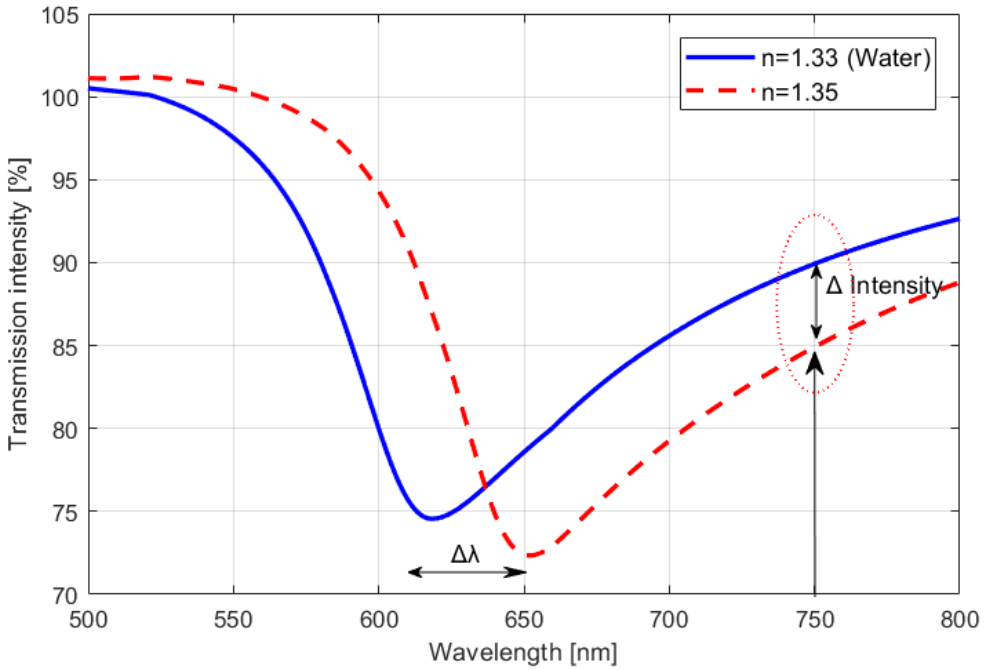

Figure 2.10: Graphic illustration of the intensity interrogation principle.

The same thing holds true also for the phase interrogation, which over-complicates the setup, in order to distinguish the phase difference between two polarizations [32].

Let us close this section with the last trend on OFSPR sensors based on smartphones. Lately, scientists have proposed using smartphones to make fully mobile, low cost SPR sensors [33, 34]. A short fiber, properly modified to exhibit the SPR phenomenon, can be connected between the flash light of the camera and the camera itself. The device exploits an intensity interrogation method, by either filtering the flash light before coupling it to the fiber, to have a specific wavelength, or by filtering the camera sensor. These kind of setups combine the full advantages offered by optical fiber based sensors and of consumer electronics, being low cost, compact, real-time and ready for in-situ measurements. However, they still present some sensitivity and reliability issues.

The sensors treated in this thesis, both in the simulation and in the experimental parts, operate in transmission, exploiting the first method of uncladding the fiber for plasmonic excitation. As previously mentioned, transmission based sensors are easier to be produced, and easier to operate, even though the lack the capability of being used as probes. However in laboratory environment the probe like design is not necessary. The experiments are based on large core MMFs with polymeric

cladding so that the cladding can be easily removed by means of a mechanical stripper or with some acetone. All in all, having the goal of analyzing the detection limits, the main reasons for this choice are the low cost and ease in operation.

Chapter 3

Mathematical Model and Simulations

This chapter will focus on the simulations of the OFSPR sensors in MATLAB, discussing the design parameters, the assumptions to simplify the process, the differences with respect to reality and future improvements. This part can be considered also as a continuation of Ch. 2, as it covers the mathematical model of the sensor, and the reader can understand in a more explicit way how the design parameters have direct impact on the final result. The chapter starts with the main aspects of the mathematical and physical model, discussing the assumptions taken in consideration to simplify the simulation process. It continues with discussion on the design parameters and their impact on the sensing performance according to some quality standard parameters, and ends with the simulation of a "novel' five layered structure. The refractive indices of the materials involved in the in simulations, considering the wavelength dependency (dispersion) are taken from https://refractiveindex.info/

3.1 Mathematical and Physical Approach

As seen earlier in Ch. 2, the SPR phenomenon consists of the excitation of a SPW at the interface between a metal (gold) and a low RI dielectric (water) from light coming from a higher RI dielectric (glass). Thus, to start creating the first physical model for an SPR structure, one should imagine a three layer structure, where a thin metal layer is sandwiched between a substrate of glass in one side and water one the other side. Fig, 3.1 schematically illustrates the three layer structure. For simulation purposes the glass and water layers can be considered semi-infinite, thus their thickness is irrelevant, while the thickness of the metal layer plays a very important role as it will be seen. The light beam is incident from the glass and at the glass-metal interface is partially reflected and partially absorbed to excite

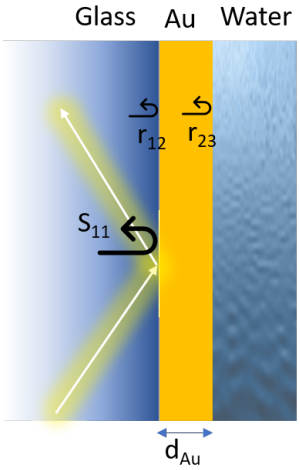

Figure 3.1: Schematic illustration of the simulated three layered structure.

the SPW. The equation that describes the light reflection on a three layered (slab) structure is written below in Eq. 3.1:

$$S_{11} = \frac{r_{12} + r_{23} \cdot \mathrm{e}^{-j \cdot k_{z2} \cdot d_{\mathrm{Au}}}}{1 + r_{12} \cdot r_{23} \cdot \mathrm{e}^{-j \cdot k_{z2} \cdot d_{\mathrm{Au}}}} \tag{3.1}$$

where r_{12} and r_{23} are the elementary Fresnel coefficients calculated as in Eq.s 3.2; k_{z2} is the wave vector in the direction of propagation z (horizontal axis in the figure) in medium metal, medium 2, and d_{Au} the corresponding thickness.

$$r^{\mathrm{s}}_{\mathrm{l,l+1}} = \frac{Z^{\mathrm{s}}_{\mathrm{l+1}} - Z^{\mathrm{s}}_{\mathrm{l}}}{Z^{\mathrm{s}}_{\mathrm{l+1}} + Z^{\mathrm{s}}_{\mathrm{l}}} \quad \text{for s} - \text{polarization} \tag{3.2a}$$

$$r^{\mathrm{p}}_{\mathrm{l,l+1}} = \frac{Z^{\mathrm{p}}_{\mathrm{l+1}} - Z^{\mathrm{p}}_{\mathrm{l}}}{Z^{\mathrm{p}}_{\mathrm{l+1}} + Z^{\mathrm{p}}_{\mathrm{l}}} \quad \text{for p} - \text{polarization} \tag{3.2b}$$

where l indicates the layer number and Z is the characteristic impedance of the respective materials, which depends on the wavelength, polarization and angle of the incidence and the refractive index of the material. For further details the reader can refer to Appendix C where the most important MATLAB functions for the SPR simulations are reported.

As mentioned also in the previous chapter (Ch. 2), usually between the glass substrate and the gold layer, a few nanometers of titanium (Ti) or chromium (Cr) are deposited to enhance the adherence. Therefore, in order to have the simulation as close as possible to the experimental reality, it is necessary to consider also this auxiliary layer in the calculations.

Moving from a three layered structured to a four layered one or even more, the calculations are just to be repeated iteratively once more. The calculations are started from the right to the left and the S_{11} calculated before, now it holds just for the three layers on the most right side of the structure and we call it S'_{11} expressed as in Eq. 3.3 below.

$$S'_{11} = \frac{r_{23} + r_{34} \cdot \mathrm{e}^{-j \cdot k_{z3} \cdot d_{\mathrm{Au}}}}{1 + r_{23} \cdot r_{34} \cdot \mathrm{e}^{-j \cdot k_{z3} \cdot d_{\mathrm{Au}}}} \tag{3.3}$$

The S'_{11} can now be considered as the second elementary reflection coefficient of a three layered structure and be put in the same equation leading to Eq. 3.4.

$$S_{11} = \frac{r_{12} + S'_{11} \cdot \mathrm{e}^{-j \cdot k_{z2} \cdot d_{\mathrm{Ti}}}}{1 + r_{12} \cdot S'_{11} \cdot \mathrm{e}^{-j \cdot k_{z2} \cdot d_{\mathrm{Ti}}}} \tag{3.4}$$

Fig. 3.2 schematically illustrates the four layered structure including the Ti layer.

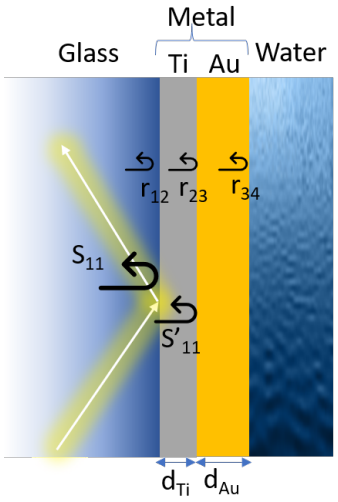

Figure 3.2: Schematic illustration of the simulated four layered structure.

This procedure is standard for any multilayered structure; what makes the situation "special" are the materials involved and the way they are ordered. The metal (Au) layer thickness should not exceed 100 nm, ideally 50 nm to 70 nm, and this is confirmed by our simulations but also in experimental works present in the literature [24]. Below 50 nm the metal layer is not reflective enough, and above 100 nm the thickness gets close to the maximum penetration depth of the metal, thus very few light reaches the second interface. However, as previously mentioned these numbers are valid for gold and certainly vary when other materials are involved.

The simulations are meant to get as close as possible to the experimental reality by considering as many details as possible, in order to be valid representatives of the experimental work. A very important detail of the fiber multi layered structure present in reality but not considered in the simulation is the cylindrical shape of the fiber. In practice, these simulations consider only the meridional rays (rays passing through the center of the fiber), neglecting the presence of the skew rays propagating in the fiber, implicitly assuming that their behavior is very similar to the others. Another assumption considered in the simulation is the flatness of the surfaces and the uniform thickness of the metal layers. However, in the actual sensors the thickness of the metal layer is not uniform, as we deposit the metal layer only on two symmetrical sides of the fiber, not continuously rotating it. This means that the thickness of the gold layer varies from 0 to 50 nm in an elliptic shape. More details on the sensor preparation and on the metal deposition process can be found in Appendix A.

After analyzing the physical and the mathematical approach of the SPR fiber structure, we can now move to the simulation of the light source and of the power distribution within the fiber. In practice, to observe the SPR curve in wavelength interrogation we use a white LED with an almost flat spectrum in the 470 nm to 850 nm range. However, the measurements are always taken with respect to a reference, thus the spectrum can be considered perfectly flat and normalized. Thus, in the simulation we can easily consider a light source with a flat spectrum. However, LEDs have a Lambertian shape power distribution with respect to the launching angles, which means different launching angles carry different power densities. Moreover, the optical power generated by the LED does not couple totally into the fiber as it is limited by the fiber numerical aperture, which determines the acceptance cone. The coupled portion propagates along the fiber with normal distribution, meaning that the central rays carry more power within the fiber compared to the peripheral ones. The coupled power portion in the fiber is described by the following Eq. 3.5 [35, 36, 37].

$$P_{\text{in}}(\theta_{\text{critical}})d\theta_{\text{critical}} \;\propto\; (\tan(\theta_{\text{critical}})/\cos^2(\theta_{\text{critical}}))d\theta_{\text{in}} \tag{3.5}$$

and the power distribution with respect to each angle due to the Lambertian power distribution of the source can be expressed as in Eq. 3.6:

$$P(\theta) \;\propto\; n_{\text{core}}^2 \sin(\theta)\cos(\theta) \tag{3.6}$$

Depending on the sensitive length and on the core diameter, another parameter that plays an important role is the number of reflections for each of the angles in which light is propagating. The number of reflection within the sensitive length can be expressed as in Eq. 3.7 [38]:

$$N_{\text{refl}} = \frac{L}{d\tan(\theta_{\text{cm}})} \tag{3.7}$$

where θ_{cm} is the angle in the core metal interface. It has to be considered that only the p-polarized light (TM polarization) contributes to the SP excitation, thus considering a non-polarized light with 50% of its power being s-polarized, only the 50% portion of the p-polarized light will be affected by the phenomenon. The final equation of the power transmitted can be written as expressed in Eq.3.8 [39]:

$$P = P_{\text{distrib}} \cdot (W_{\text{s}} \cdot R_{\text{s}}^{N_{\text{refl}}} + W_{\text{p}} \cdot R_{\text{p}}^{N_{\text{refl}}}) \tag{3.8}$$

where $W_{\text{s,p}}$ is the weight of each polarization, respectively (50% in case of non-polarized light); $R_{\text{s,p}}$ is the reflectivity calculated as mentioned in Eq. 3.4; P_{distrib} is the coupled power distribution calculated from Eq. 3.5 and in Eq. 3.6; N_{refl} is the number of reflections within the sensitive area calculated from Eq. 3.7.

Another remark worthy to be mentioned is the polarization of light. In general in our experiments we have worked with non polarized light, which can be easily considered 50% s-polarized and 50% p-polarized. However as the metal layer has a curved surface (not in the same plane), launching a specific polarized light does not make that much sense, as the polarization would hold only with respect to a single specific plane. In the simulations we have considered that the light holds the non polarized nature, also after a reflection has occurred on the metal interface, even though we know that a certain portion of the p-polarized light is absorbed by the SPW.

Last but not least, to be remarked is also the fact that both in practice but also replicated in the simulations, the SPR curve plotted in the graphs in this dissertation (but also in the literature) is not the raw spectrum. Actually a reference needs to be taken when the sensor is exposed in air. Thus what we call SPR curve is actually the effect of the SPR phenomenon in water divided by the effect of the SPR phenomenon in air. In practice, it is advised to subtract from both the curves the dark spectrum, in order to avoid the effect of the background noise. Finally what we generally see in an SPR plot is expressed in the Eq. 3.9.

$$\text{SPR} = \frac{SPR_{\text{water}} - (\text{Dark})}{SPR_{\text{air}} - (\text{Dark})} \cdot 100\% \tag{3.9}$$

3.2 Design and Quality Parameters

This section will focus on the design parameters of an OFSPR and their impact on the performance of the sensor. In most of the cases, the selection is limited due to the commercial available devices or to technical limitations. For instance, for adhesion purposes, we have selected a titanium layer of 20 nm. The selection of the material was due to the availability in the lab, while the thickness was recommended by the technical engineer of the clean room, claiming that a thinner layer would not

guarantee the deposition process. However, in the simulations we have considered a possible variation in the Ti layer thickness. The main parameters of a sensors are:

- Fiber core diameter.
- Numerical aperture (NA) of the fiber.
- Sensitive length.
- Titanium (Ti) layer thickness.
- Gold (Au) layer thickness.

Let us now consider each relevant design parameter one by one and their possible intervals of variations. The Ti layer thickness in the simulations is considered in the possible 10 nm to 30 nm range and the Au layer thickness in the 30 nm to 60 nm range, with a step of 5 nm. Instead, when talking about the core diameter of the fiber we have taken into consideration fibers of 200 µm, 400 µm and 600 µm. These are the diameters of the main commercial available MMFs. The main reason for choosing large core fibers has been the robustness of the fiber, but also the ability of large core fibers to collect light, guaranteeing a higher SNR. The numerical aperture of such large MMFs is typically 0.22, 0.39 or 0.5. In our case we focused on fibers with a polymeric (plastic) cladding, which can be easily removed manually by using a stripper or chemically with the help of some acetone. This specification reduces the possibilities to just two options 0.39 and 0.5 because the refractive index of silica, which is generally used for core, and the refractive index of the polymeric cladding (TECS, which stands for technology enhanced clad silica-removable clad fibers, as called by Thorlabs) in this case have a larger contrast, giving a larger NA (Eq. 2.5a). Last but not least, the sensitive length of the sensor. We have selected to simulate lengths in the 1 cm to 4 cm with 1 cm step. The maximum length has been limited to 4 cm, to keep the dimension of the sensor handy and guarantee robustness.

Table 3.1: Sensor design parameters taken into consideration during simulations.

Parameter	Interval	Step	Unit	Total
Core diameter	200 : 600	200	µm	3
NA	0.39; 0.5	-	-	2
Sensitive length	1 : 4	1	cm	4
Ti thickness	10 : 30	5	nm	5
Au thickness	30 : 60	5	nm	7
Combinations				**840**

Tab. 3.1 shows all the variables with their respective intervals and the number of total combinations that can be achieved which is 840. The MATLAB program is executed for each of the combinations generated and the important parameters are stored.

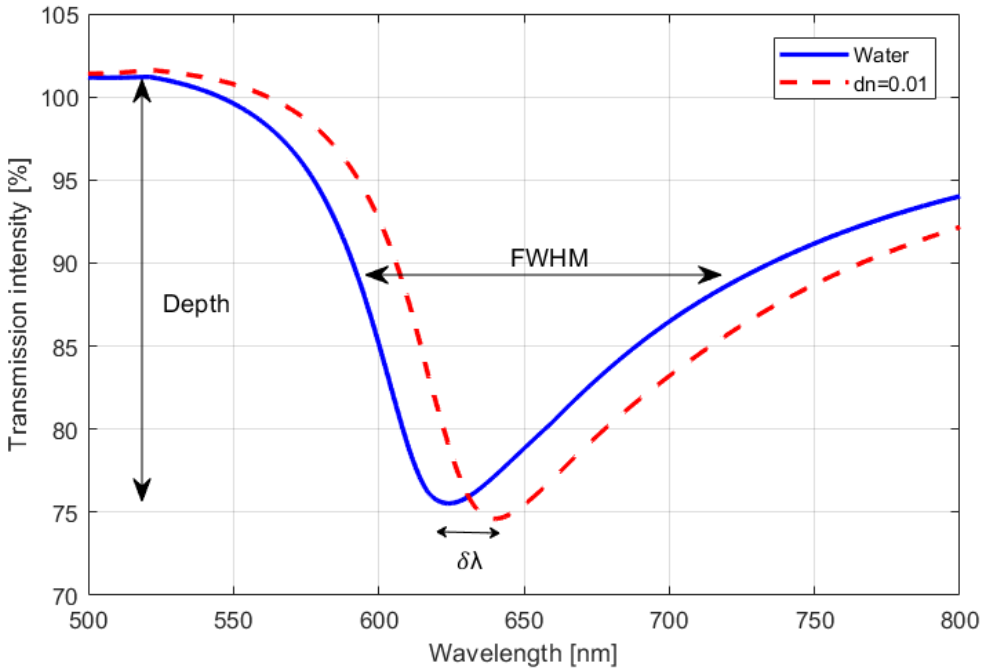

Figure 3.3: SPR curve parameters illustrated. Depth of the curve, shift in resonance wavelength and the FWHM.

Let us now see how we can evaluate the performance of an OFSPR sensor based on the obtained SPR curve in wavelength interrogation. The three main parameters that will be used also to compare the sensors in a qualitative way are: the depth of the curve, the Full Width at Half Maximum (FWHM), which actually, in the SPR curves it could be better described as the anti-FWHM or the full width at half depth, and the sensitivity, which can be calculated as

$$S = \frac{\lambda_{\mathrm{SPR2}} - \lambda_{\mathrm{SPR1}}}{\delta n}$$

. The parameters are illustrated graphically in a simulated example in Fig. 3.3.

In order to have a more complete evaluation of a sensor, these three key parameters can be related one another creating composite quality parameters, such as the Detection Accuracy (DA) and the Figure Of Merit (FOM), each of them defined

as expressed in Eq. 3.10 [40, 41]:

$$\mathrm{DA} = \frac{H}{\mathrm{FWHM}} \tag{3.10a}$$

$$\mathrm{FOM} = \frac{S}{\mathrm{FWHM}} \tag{3.10b}$$

where H is the depth of the SPR peak and S is the sensitivity. During the simulations, both H and the FWHM are calculated from a single SPR curve computed while the sensor is immersed in water; instead for S, which is measured in nm/RIU (where RIU is a dimensionless quantity that stands for Refractive Index Unit), at least two curves are needed to be calculated, one assuming water and another assuming a refractive index $n_{\mathrm{water}} + \delta n$, with $\delta n = 0.01$. Based on the above equations the FOM is measured in RIU^{-1}, while the DA is measured in %/nm.

3.3 Simulation Results and Discussions

Considering the detection accuracy (Eq. 3.10a) as a key factor in terms of quality, the best sensor design has these parameters: **NA = 0.39; core diameter =** 600 µm**; sensitive length =** 2 cm**; Ti thickness =** 10 nm **and Au thickness =** 45 nm. In this case $FWHM = 62.3\,\mathrm{nm}$ and $H = 18.9$ %, giving DA = $0.297\,\mathrm{nm}^{-1}$. This sensor has a sensitivity $S = 1820\,\mathrm{nm}/RIU$ and thus would be ranked $180^{\mathrm{th}}/840$ in terms of figure of merit with FOM = 19.084 RIU^{-1}. Fig. 3.4 (top) shows the plot of the simulated SPR curve of the sensor, which has the best performance in terms of DA while immersed in water.

Following the same logic the sensors can be ranked with respect to their figure of merit (Eq. 3.10b). The best sensor in this case has the following design parameters: **NA = 0.39; core diameter =** 200 µm**; sensitive length =** 3 cm**; Ti thickness =** 25 nm **and Au thickness =** 60 nm. This sensor has a FWHM = 35.7 nm and a sensitivity S = 1750 nm/RIU, thus resulting in a figure of merit FOM = 49.02 RIU^{-1}. This is ranked $760^{\mathrm{th}}/840$ in terms of detection accuracy with DA = $0.11\,\mathrm{nm}^{-1}$.

Fig. 3.4 (middle) illustrates the SPR curve of the best sensor in terms of figure of merit. The FOM is a parameter that depends on S and on FWHM and in this case it can be clearly observed that the parameter is dominated by the small FWHM, as the sensor has a very shallow and narrow peak, while instead the sensitivity is even lower than the previous case (best DA sensor). This means that the FOM might result in a misleading parameter, but in the meantime it carries a very important information, the sensitivity of the sensor, which is neglected in the detection accuracy. In order not to neglect any factor relevant to the quality of an OFSPR sensor, we introduced

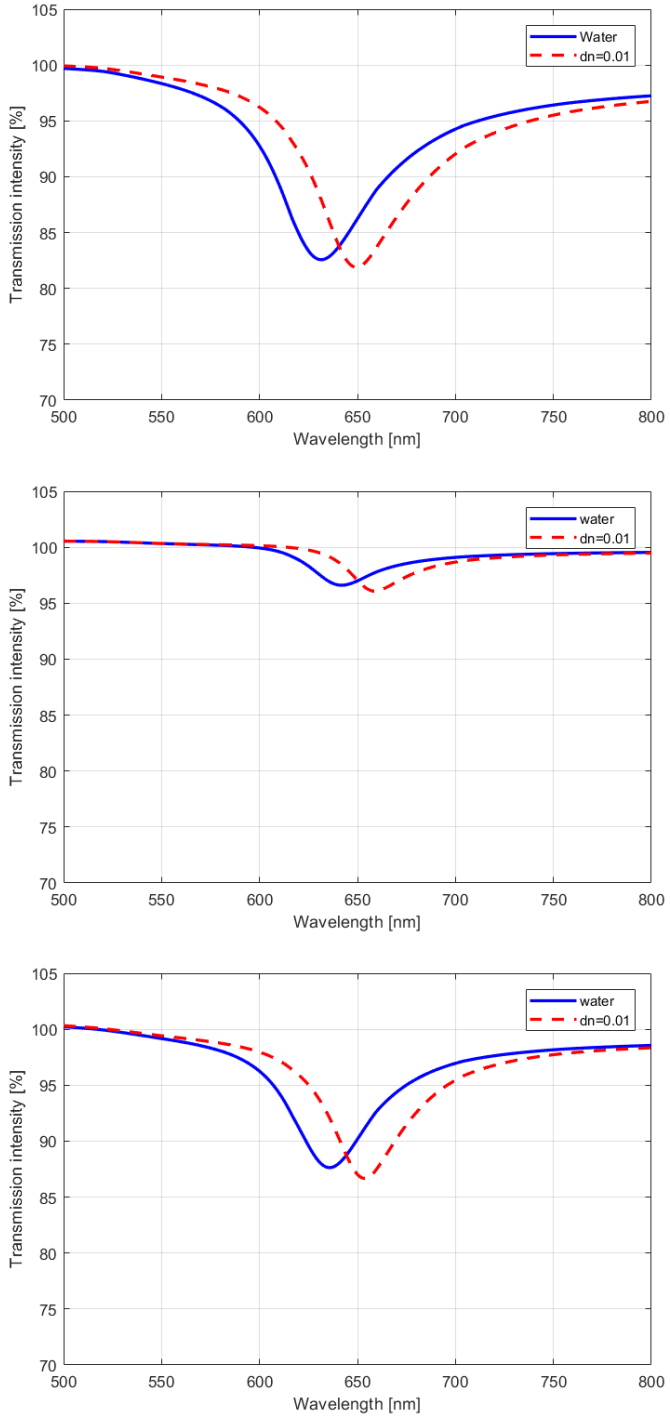

Figure 3.4: Simulated SPR plot of the sensor which performs the best in terms of DA (Top), FOM (middle) and QP (bottom); water (n=1.33) blue solid line, n=1.34 red dashed line

for the first time another qualitative parameter, called **Quality Parameter, QP**, which is obtained by the product of the DA and FOM:

$$\mathrm{QP} = \mathrm{DA} \times \mathrm{FOM} \tag{3.11}$$

or

$$\mathrm{QP} = \frac{H \times S}{\mathrm{FWHM}^2} \tag{3.12}$$

Where DA and FOM are calculated as specified in Eq. 3.10a and Eq. 3.10b ,respectively. The unit of QP is going to be [%/RIU × nm]. The DA of the simulated sensors varies in the [0.05 to 0.297] range, while the FOM varies in the [3.38 to 49] range. The QP varies in the [0.2 to 10.04] range, which makes it even more intuitive as a parameter to qualify our sensors. The sensor with the highest QP has the following specifications:**NA = 0.39; core diameter** = 600 µm**; sensitive length** = 4 cm**; Ti thickness** = 10 nm **and Au thickness** = 55 nm. This sensor is ranked 43$^{\mathrm{rd}}$/840 in terms of DA and 264$^{\mathrm{th}}$/840 in terms of FOM. The SPR curves of such sensor are illustrated in Fig. 3.4 (bottom).

Table 3.2: Design parameters of the sensors and characteristics of their respective SPR curves for the sensors with best performance according to each quality defining parameter.

Parameters	**Best DA**	**Best FOM**	**Best QP**	**Unit**
Core diameter	600	200	600	µm
NA	0.39	0.39	0.39	-
Sensitive length	2	3	4	cm
Ti thickness	10	25	10	nm
Au thickness	45	60	55	nm
Sensitivity	1820	1750	1820	nm/RIU
FWHM	62.3	35.7	49	nm
Depth	18.9	3.94	13.25	%

Fig. 3.5 shows the plot of the three simulated SPR curves for a sensor immersed in water. The red dashed curve is the one of the FOM, the blue solid line the one with the highest DA, while the green dotted line the curve with the highest QP. It can be observed that the green dotted curve lays somewhere between the two other curves, being the curve with the optimum situation between a deep peak, a narrow FWHM and a high sensitivity. Tab. 3.2 reports the summary of the best performance sensor according to the above mentioned parameters.

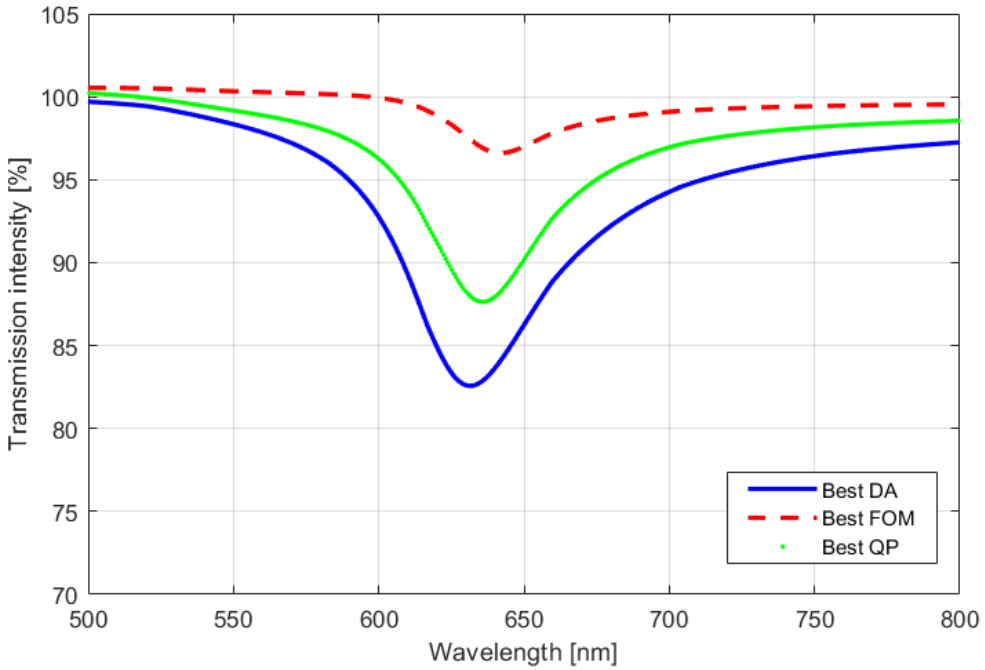

Figure 3.5: Comparison among the best FOM curve (red dashed line), the best DA curve (blue solid line) and the best QP curve (green line). All curves are simulated in a situation where the sensor is immersed in water (n=1.33).

3.4 Novel Five - Layer Design

The robustness of the sensor in view of long term applications can be improved by adding a silica nano-layer on top of the gold layer, in order to avoid the direct contact of the gold layer with the medium under test. This way the metal layer responsible for the SPR phenomenon would have a protective layer that guarantees a longer life. This is a novel architecture that is sketched in Fig. 3.6. There is one more iteration to be calculated in terms of elementary reflection coefficient in this case compared to the four-layer structure already abalyzed.

As we want to keep the sensor sensitive to a variable outer medium the extra silica layer has to be a nano-layer, in order to allow the wave propagate through all the layers. Even though the penetration depth differs from metals to dielectrics, in the simulations 4 different thicknesses of silica layer have been considered: [0, 5, 10, 15] nm. With the added layer the table of the total possibilities now is shown in Tab. 3.3 and the total number of combinations is multiplied by a factor of 4.

Fig. 3.8 shows the DA, the FOM, and the QP of each sensor in zoomed out scale in order to make visible the impact of the added silica layer. The first 840 points in each graph correspond to no silica layer added, the second interval to the designs

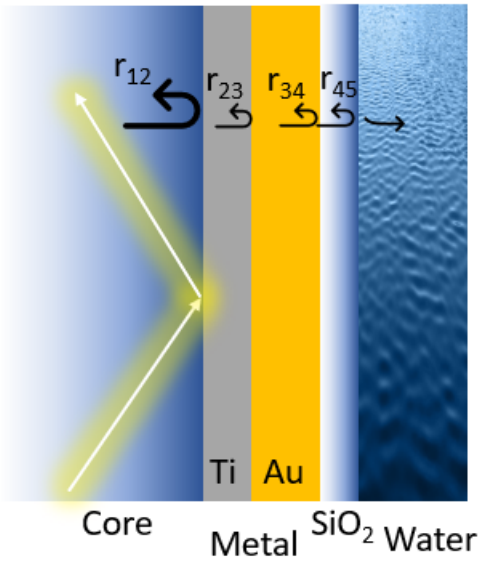

Figure 3.6: Schematic illustration of a 5-layered structure. A silica nano-layer is added on top of the metal layer.

Table 3.3: Sensor design parameters considered during the simulations for the five-layer structure.

Parameter	Interval	Step	Unit	Total
Core diameter	200 : 600	200	um	3
NA	0.39; 0.5	-	-	2
Sensitive length	1 : 4	1	cm	4
Ti thickness	10 : 30	5	nm	5
Au thickness	30 : 60	5	nm	7
SiO_2 thickness	0 : 15	5	nm	4
Combinations				**3360**

with 5 nm of silica, and so on. The graphs clearly show that the added silica layer has a positive impact in all the evaluation parameters. Meaning that the added silica layer adds other very important benefits in terms of measurement quality to the sensor, apart from being just a protective layer.

The sensor that best performed with the four-layer structure, still remains one of the best designs even in the five-layer case, by adding 15 nm of silica. The impact of the silica layer on the SPR curve of the sensor is shown in Fig. 3.7. Tab. 3.4 shows the impact of the silica layer on the evaluation parameters of the best QP sensor in case of the four-layered structure. The sensor had the following specifications:

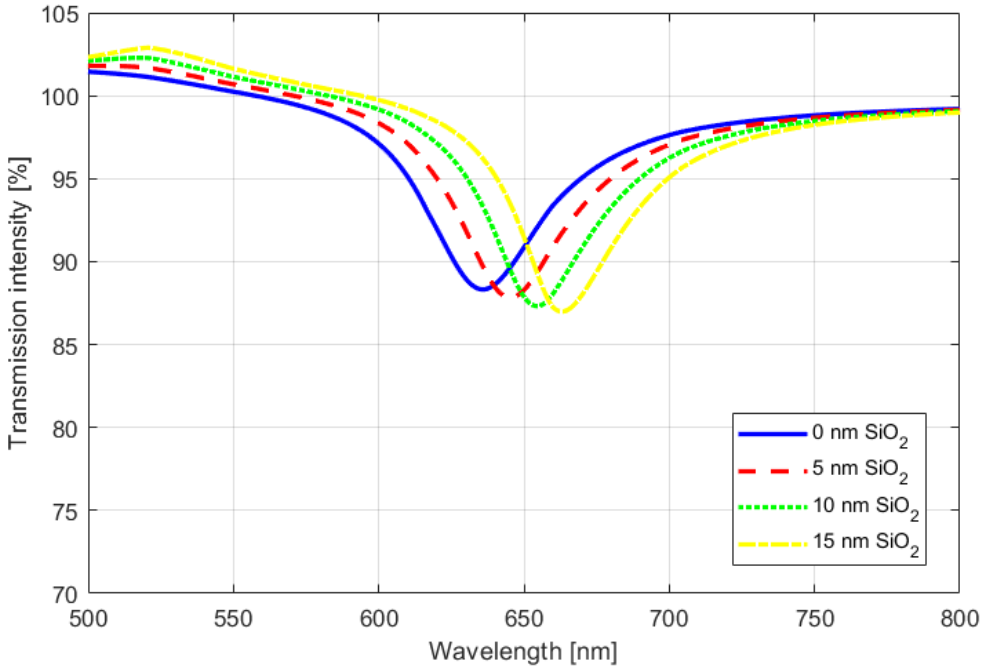

Figure 3.7: Impact of the silica layer on the SPR curve of the best QP sensor.

Table 3.4: Impact of silica thickness on the sensor with the best performance.

Silica thickness	DA	FOM	QP
0 nm	0.28	34.92	9.78
5 nm	0.31	36.67	11.36
10 nm	0.36	40.00	14.53
15 nm	0.43	42.00	18.14

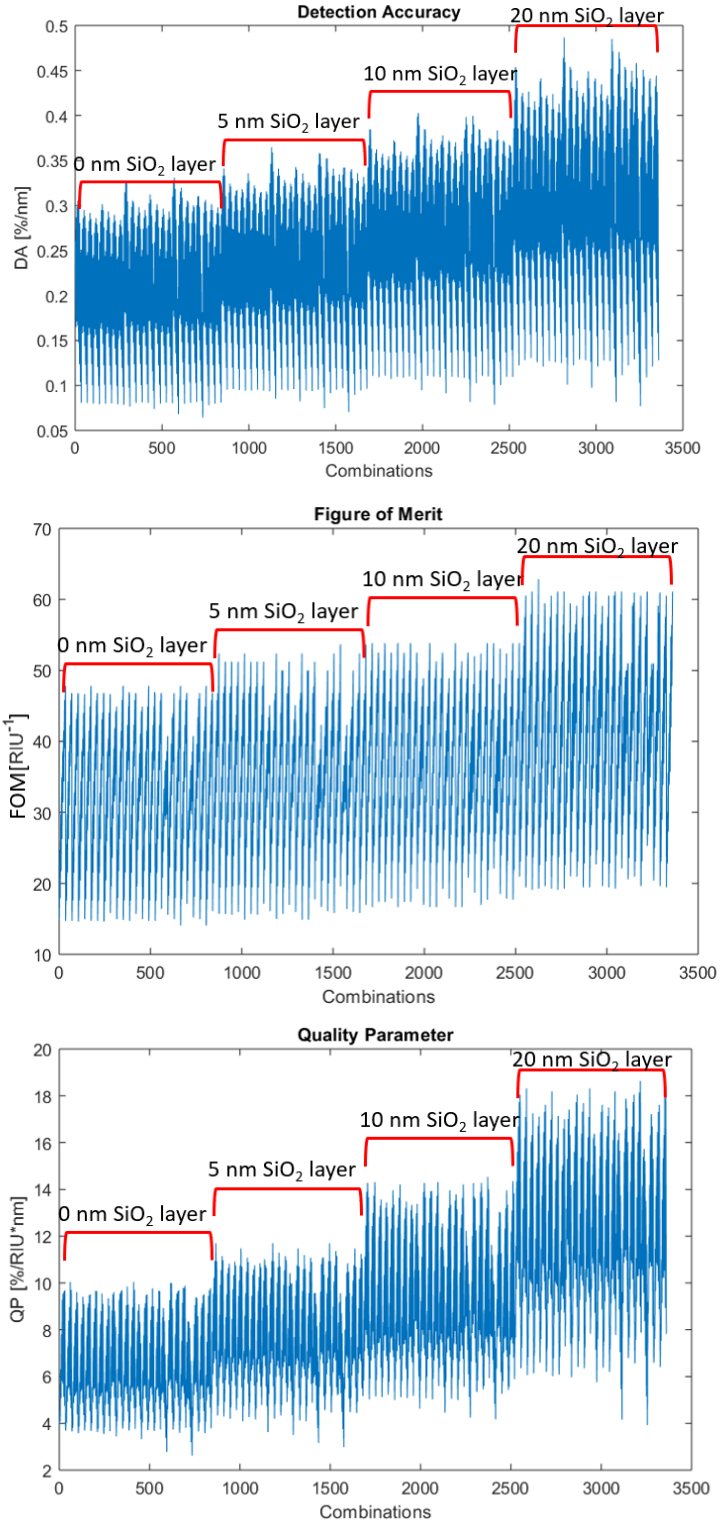

Figure 3.8: DA,FOM and QP of all the designed sensors.

Chapter 4

Experimental Work and Results

This chapter focuses on the experimental work performed regarding the OFSPR sensor. The experiments have been carried out part in the PhotonLab (Laboratory of Photonics) and part in the Automated Measurements Lab of the Polytechnic University of Turin. Focusing on the SPR, several sensors have been prepared, characterized and tested in different setup configuration.

The first sensor characterization setup has been the "classical" wavelength interrogation method that makes use of a white broadband light at the input and a spectrum analyzer at the output. This approach gives an SPR curve very similar to that expected from the simulations and therefore it simplifies the comparison between the simulation and experimental results. Then, the focus has moved towards more compact and lower cost setups in which the high quality spectrum analyzer is replaced with wavelength selective photodiodes or even with a simple photodiode combined with a narrow-band source (colored LED) at the input. The goal of the analysis of different setups is to make a cost / performance analysis.

Some parts of the experimental work are described in the Appendix A and in Appendix B to ease following the flow of the chapter. This does not mean that the material in the appendices is irrelevant: on the contrary, Appendix A is dedicated to the sensor preparation procedure, which is quite a critical process requiring specific attention, while Appendix B describes the characterization process and the characteristics of 12 different OFSPR sensors.

4.1 OFSPR Wavelength Interrogation

This section starts with the characterization of an OFSPR sensor by interrogating its spectrum. The sensor is based on a 400 µm core fiber with a sensitive length of 3 cm, NA of 0.39, and the metal layer composed of 20 nm of Ti and 40 nm of Au. It has to be recalled that, as also previously specified, the thickness of the metal

layer in our sensors is not uniformly distributed around the fiber circumference. Fig. 4.1 illustrates schematically the result of symmetrically double sided deposition. Obviously the image is not in scale, just for illustration purpose, otherwise the thickness of the metal layer is almost invisible compared to that of the core. However, in some cases this figure could be not totally correct since it is possible that a fiber undergoes slight torque when rotated in order to deposit the opposite side; in such cases, the resulting deposition is not symmetrical, and the thickness of the layers is practically impossible to be predicted. However neglecting this fact, one has to consider that the metal layer has its maximum and desired thickness of 20 nm of Ti followed by 40 nm of Au, while the effective thickness is definitely less, somewhere in the 0 nm to 60 nm range.

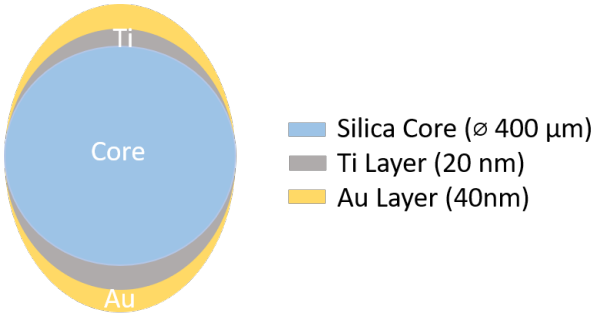

Figure 4.1: Schematic illustration of non uniformly deposited metal layers (out of scale).

The experimental characterization of the sensors is made using mixtures of water and isopropyl alcohol ($CH_3CHOHCH_3$, commonly called isopropanol) to produce a liquid with refractive index in the 1.333-1.376 range. Both water and isopropanol have refractive index that varies with respect to the wavelength (the chromatic dispersion, which has been considered also in the simulations). It is quite common to refer to RI at $\lambda = 589\,\text{nm}$. For the water and alcohol mixtures, there exists a relationship that considers their intrinsic refractive index values and densities [42]:

$$n_{\text{mix}} = 1 + \rho_{\text{mix}} \cdot (\omega_{\text{water}}(\frac{n_{\text{water}} - 1}{\rho_{\text{water}}}) + \omega_{\text{iso}}(\frac{n_{\text{iso}} - 1}{\rho_{\text{iso}}})) \tag{4.1}$$

where n is the RI, ρ is the density, and ω is the mass ratio in the mix for the respective liquids. Actually the formula is known as Gladstone-Dale relation and it holds for any mixture of two liquid solutions.

The wavelength interrogation has been implemented with a transmission setup in which in the input there is a white broadband LED (MBB1F1 - Thorlabs) emitting in the visible spectrum 470 nm to 850 nm, and a spectrometer in the 200 nm

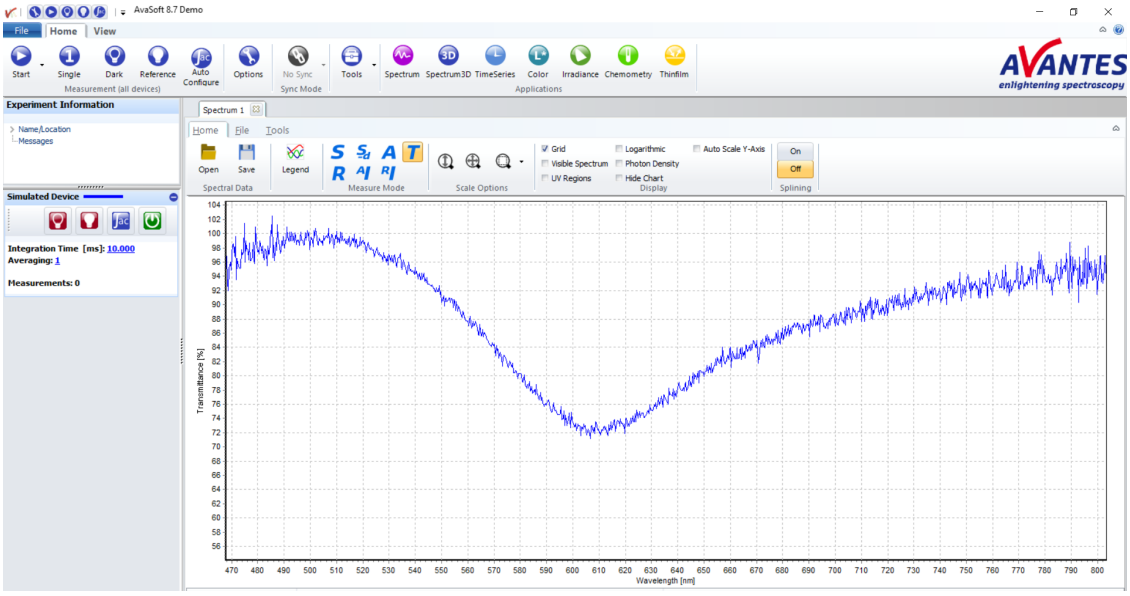

Figure 4.2: Screenshot of the Avasoft (the software of the Avantes spectrometer used to measure the spectral response) while plotting an SPR curve of a sensor immersed in water.

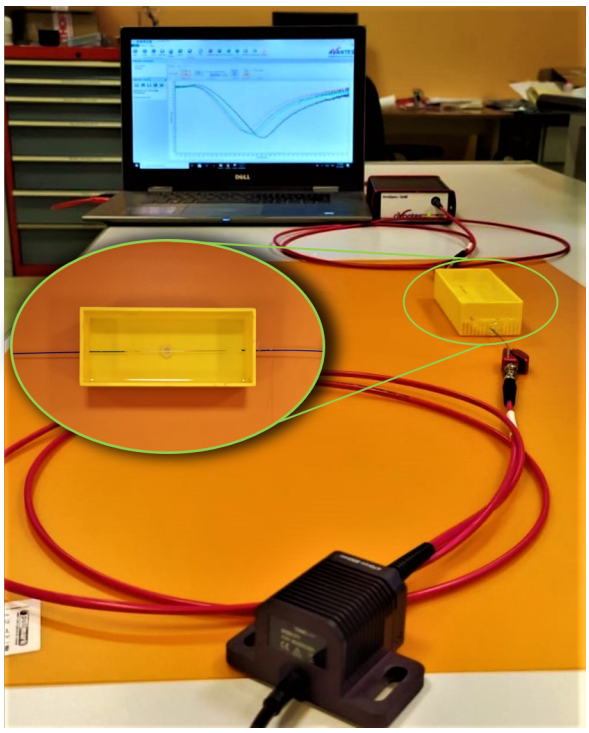

Figure 4.3: Setup of the wavelength interrogation system.

to 1100 nm range (Avantes - AvaSpec-ULS3648) at the output. Fig. 4.3 shows a photo of the experimental setup. The measurement procedure starts by taking a reference while the sensor is exposed in air, thus just the fiber connected in its two ends to the source and the spectrometer. A dark reference is also stored, with the sensor connected but with the source turned off. The final step is to configure the spectrometer in transmission mode, and the software (Avasoft-screen illustrated in Fig. 4.2) automatically considers the formula written in Eq. 3.9, and plots what we call the SPR curve.

The spectrometer has a resolution of 0.3 nm and the user can select the wavelength range of interest where the scanning occurs. Moreover, the user can select the integration time, the number of averages and the smoothing pixels. The integration time is usually set as high as possible, guaranteeing that the signal does not go in saturation. While the smoothing pixels and the number of averages are set to 0, because the signals are post-analyzed in MATLAB, and all the data processing is made in MATLAB. Initially, the spectra are saved either in EXCEL, or in a text file and then are imported into MATLAB for further analysis. The section of the curve around the SPR peak is fitted to a second order polynomial in order to reduce the noise contribution while detecting the peak. This process substitutes the smoothing pixel procedure offered by the spectrometer. While in the analysis of other parameters such as FWHM or depth, the raw spectra is considered.

4.1.1 Characterization of a Sensor in Wavelength Interrogation

In this section we will consider one of the many OFSPR sensors fabricated and analyze its performance. For the characteristics of the other sensors the reader can refer to Appendix B. The sensor taken in consideration in this section has the following characteristics:

- Core diameter: 400 µm
- NA: 0.39
- Sensitive length: 30 µm
- Ti layer thickness: 20 nm
- Au layer thickness: 40 nm

For the preparation of the sensor a piece of 0.5 m long MM TECS cladding fiber (Thorlabs-FT400EMT) is taken and uncladded in a section of 30 mm. The uncladding process is done partially chemically, by dipping the fiber in acetone for several minutes, and then mechanically with a calibrated hand stripper. For the

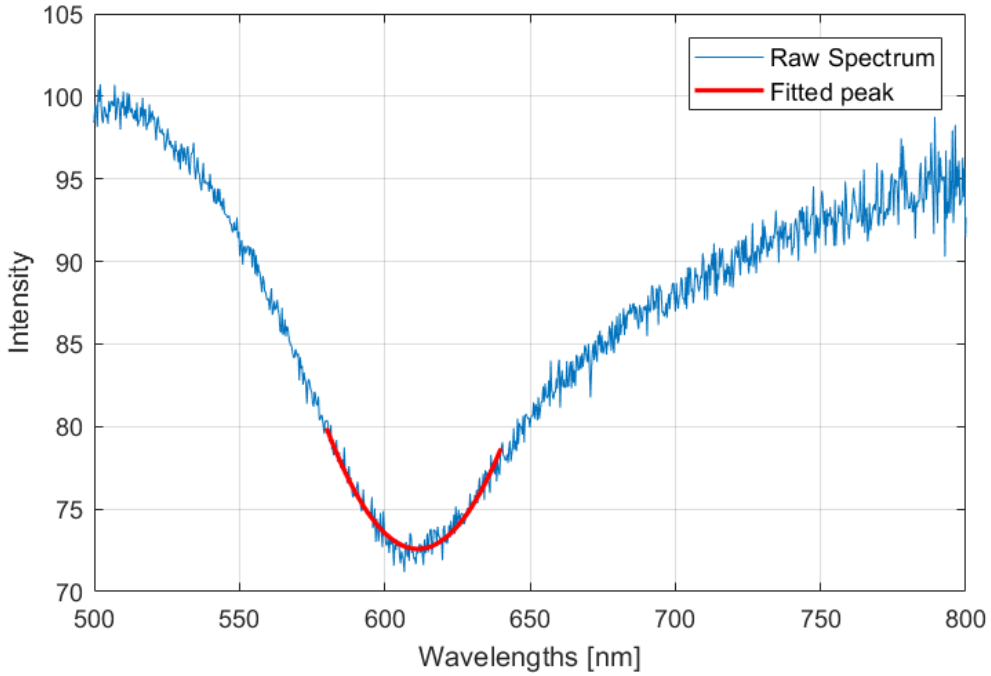

Figure 4.4: Example of a raw spectrum and the second degree polynomial fitted curve. Same spectrum show in Fig. 4.2.

full sensor preparation process the reader can refer to Appendix A.

The sensitive area of the sensor is encapsulated in a small plastic box, while the two end sides of the fiber are connected to the source and the spectrometer via two patch cords, exploiting mobile SMA connectors. Firstly the sensor is characterized with 6 different RI values obtained by mixing pure distilled water with isopropyl alcohol in 0%, 20%, 40%, 60%, 80% and 100% volume concentrations. Fig. 4.5 shows the experimentally obtained SPR peaks with their respective RI values and alcohol concentration in solid blue line and the linear fit in red dashed line. We can notice that the points do not have a fully linear linear fit; however, we can definitely say that the fitting is a nice approximation around the pure water approximation where is our area of interest. The fitting represents the average sensitivity of the sensor and has a slope of 2140 nm/RIU ($R^2 = 0.9844$).

After analyzing the sensor in terms of sensitivity, we have performed another type of experiment in order to understand the real time response of our sensor. In this case we have started by immersing the sensor in water while continuously storing the SPR spectra. In regular time interval isopropanol is added, thus the sensor is exposed to different RI values. The test has lasted 23 minutes saving 3000

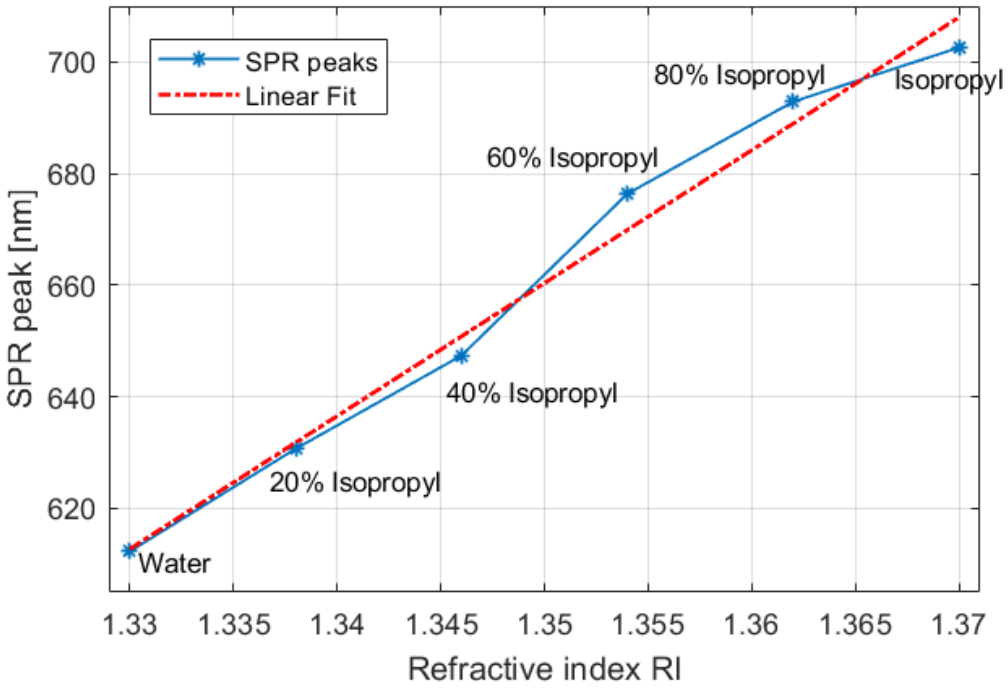

Figure 4.5: SPR peak for different refractive index values obtained from different water and isopropanol mixtures.

spectra in a continuous mode with the following chronology:

1. The data storage starts with the sensor exposed in air for 3 minutes (reference has been already taken);
2. Water is added in the container until the sensor is fully immersed in the liquid and rests for 5 minutes;
3. Isopropanol is added, such that the solution reaches 10% in concentration and rests for other 5 minutes;
4. More isopropanol is added, solution reaches 20% in concentration and rests for other 5 minutes;
5. Final step, more isopropanol is added, 40% concentrated solution, last 5 minutes.

Fig. 4.6 shows the SPR peak with respect to time during the test. The 5 markers highlight the key moments of the test described in the list above. In Fig. 4.7 the reader can find the four SPR spectra corresponding to the markers highlighted in

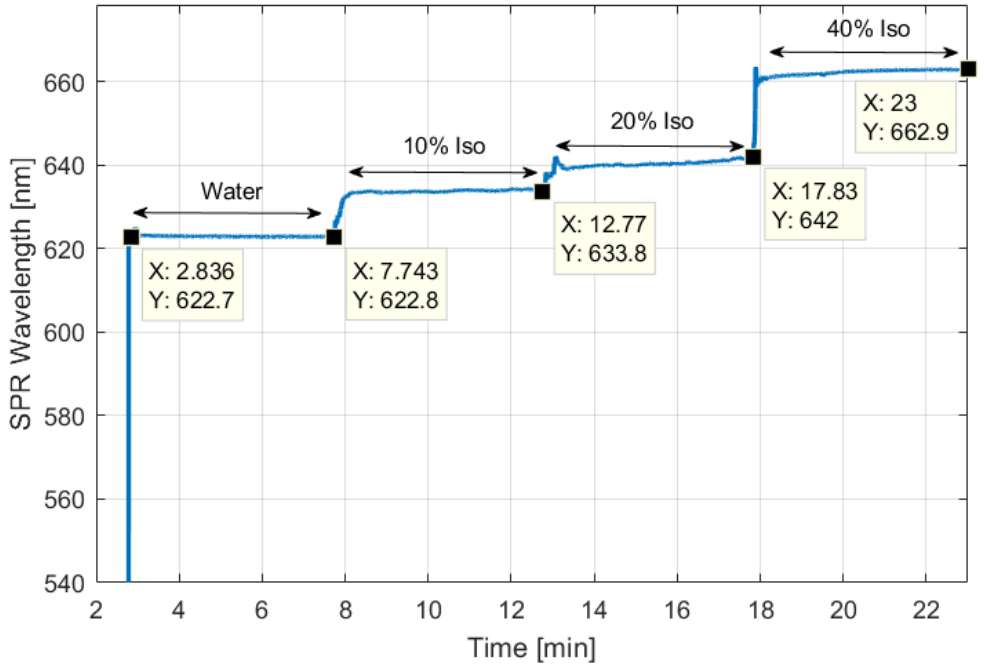

Figure 4.6: Relatively long term (23 minutes) sensor characterization tests for different RI values. Water (n=1.333); 10% Isopropanol (n = 1.3373); 20% Isopropanol (n= 1.3416); 40% Isopropanol (n= 1.3502); each interval lasted approximately 5 minutes.

Fig. 4.6 with the fitted 2nd degree polynomial around the peak wavelength.

The graph can confirm the real time response of the sensor. Nevertheless, it is important to outline that the sensor is sensitive only to few microns away from its sensitive area. This means that the water and isopropanol need to be fully mixed with one another before having a reliable readout. We can notice in Fig. 4.6 that when the sensor is immersed in pure water the curve is very flat, while when alcohol is added to the solution, 5 minutes were not enough to reach a stable condition.

Tab. 4.1 summarizes the characteristics of four SPR curves obtained in the last moment of each solution just before adding more alcohol to the mixture. Instead Tab. 4.2: shows the characteristics of the simulated sensor, which has the same design parameters as the simulated one while immersed in the same mixtures. We can now make a rapid comparison and see how well the simulations match our sensors. It can be seen that in reality our sensor is more sensitive compared to the simulations. Moreover the curve is deeper, but with a higher FWHM. However DA, the parameter that connects the depth and the FWHM of the curve in a single

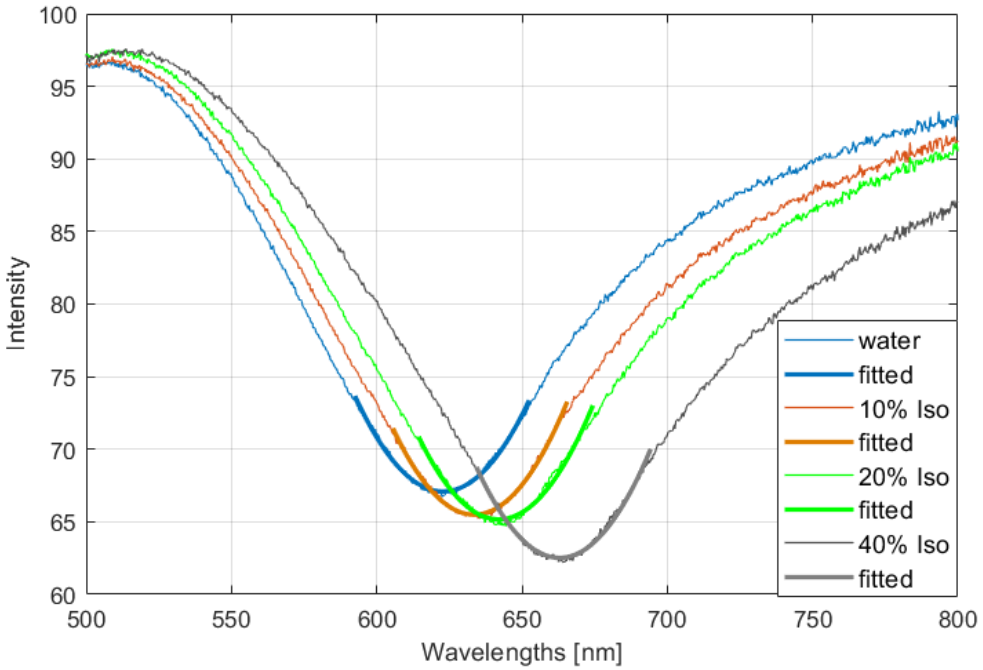

Figure 4.7: Experimental spectra and the respective 2nd order polynomial fit of 4 different refractive indices. RI = [1.333 1.3373 1.3416 1.3502] from left to right.

Table 4.1: Properties of the curves plotted in Fig. 4.7. Metrological characterization.

	Water	**10% Iso**	**20% Iso**	**40% Iso**	**Avg.**	**Unit**
RI	1.333	1.3373	1.3416	1.3502	-	-
λ_{SPR}	622.96	632.78	639.60	661.68	-	nm
Depth	34.93	35.84	35.72	37.03	35.88	%
FWHM	134.67	138.57	137.27	151.22	140.43	nm
Sensitivity	2283.49		1587.65	2567.42	2146.18	nm/RIU
DA	0.2593	0.2586	0.2602	0.2448	0.2557	%/nm
FOM	16.95	-	-	-	15.28	RIU^{-1}
QP	4.39	-	-	-	3.9	$\%/nm \cdot RIU$

number is a little higher in the experiments than in the simulations, though very similar. On the other hand, the FOM of the experimental sensor is lower than that of the simulated one, even though the sensitivity is higher. It means that in this case the FOM is dominated by the higher FWHM.
The differences between simulated and experimental values can be well justified

Table 4.2: Characteristics of the simulated sensor, with the same design parameters as the experimental one.

	Water	10% Iso	20% Iso	40% Iso	Avg.	Unit
RI	1.333	1.3373	1.3416	1.3502	-	-
λ_{SPR}	617.85	624.36	631.11	645.87	-	nm
Depth	11.87	12.25	12.65	13.53	12.58	%
FWHM	51.5	51	50.75	50.50	50.93	nm
Sensitivity	1512.38	1570.55	1715.97		1599.63	nm/RIU
DA	0.2018	0.20	0.24	0.24	0.2245	%/nm
FOM	29.36	-	-	-	31.4	RIU^{-1}
QP	5.92	-	-	-	7.05	$\%/nm \cdot RIU$

considering the assumptions made for the simulations. Moreover, it has been observed a certain variability in the sensor behavior, even though all the sensors are prepared following the same procedure detailed in the Appendix B. This might be due to several reasons such as the imperfections in the stripping process, the torque on the fiber while depositing, the shadowing on a fiber during the deposition process due to neighboring fibers, etc.

4.1.2 Stability Analysis

In order to fully characterize the developed sensors and the interrogation setup, we have performed some stability analysis tests immersing the sensors in a given liquid for up to three days. The sensors had been previously characterized with water and isopropanol mixture solutions and exhibited a sensitivity of around 2140 nm/RIU. The LED is driven in a constant current regime, while the SPR spectra are stored periodically (one spectrum every 6 seconds, so 10 spectra per minute) to be fully post processed in MATLAB. Fig. 4.8 shows how the SPR wavelength peak has evolved during the three day test of one of the sensors. The saved spectra are fitted to a second degree polynomial and the wavelength of the minimum is extracted. The peak wavelength of the sensor tested for three days exhibited a minimum value at 661.1 nm and a maximum value at 662.1 nm, with a difference of 0.1 nm, which corresponds to a RIU difference of 5×10^{-4} in case of liquid contamination or to a difference of 5 °C in the liquid temperature. Since the liquid did not change during the test and the temperature changed by 2 °C, the variations can be ascribed to drifts in the interrogation setup. Moreover, the presences of contamination would only increase the RI of the liquid and not decrease it as can be seen in the graph.

Analyzing the information provided by the graph of Fig. 4.8, the worst drift

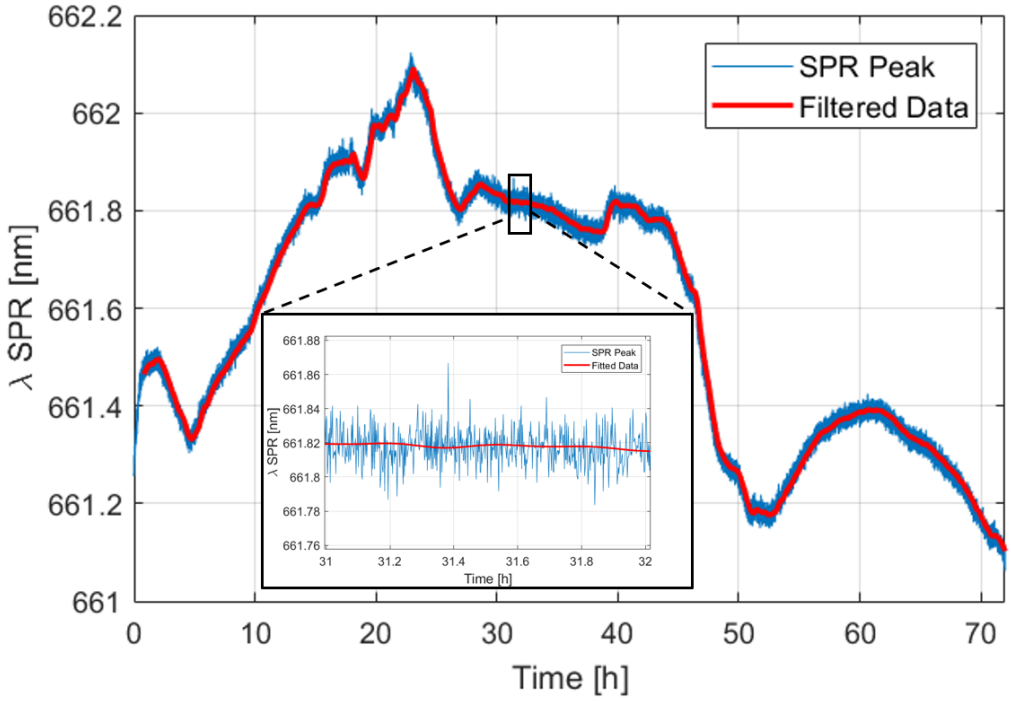

Figure 4.8: Three day stability test using the wavelength interrogation technique: blue solid line is for raw data, while the red solid line is for the filtered data.

has happened at time t = 46.6 h at a rate of −5.1 pm/min. Assuming this value as the worst case scenario of the time drift, we can expect a drift of 306 pm/h and 7344 pm/day. This values, if converted to RIU considering the sensitivity of the sensor, would represent the limit of detection of our system: 2.55×10^{-6} for a test with duration of 1 minute, 1.5×10^{-4} for a 1 hour test, and 3.67×10^{-3} for a 1 day test. It is important to remember that this is a temporal drift arising from external parasitic factors. In this case, however, it is assumed that the worst drift would continue in the same direction during a full day, and this is a scenario that most probably is never going to happen in reality. In practice, the worst drift observed during the longest tests has been of 191 pm over 1 hour and of 750 pm over 24 hours corresponding, respectively, to 8.4×10^{-5} and 3.2×10^{-4} in terms of RIU.

While the temporal drift limits the accuracy of the measurement by shifting the result away from the "expected value", we have to consider also the precision of our system. Precision is a parameter that makes sense to be calculated only in intervals where no drift is observed, thus in relatively short intervals. We have calculated the precision by looking at the standard deviation of the measurements in intervals of 1 min, 10 minutes and 1 hour. Looking at all the 1 minute intervals (10 consecutive data points) during all the three day test, the average standard

deviation is equal to 9.9 pm, while the worst one is equal to 19.8 pm. Analyzing the intervals of 10 minutes (100 consecutive data points), the average standard deviation is equal to 10.6 pm and in the worst interval equal to 21.6 pm. The same analysis is performed for all the 1 hour long intervals (600 consecutive data points) and the average standard deviation is 15.7 pm and the worst interval has a standard deviation of 59 pm. Definitely this is due to the contribution of the drift in the measurement more than to the noise floor. It can be observed that the noise contribution dominates in the uncertainty of the measurement only for very short intervals (1 minute) while for longer term measurements the drift dominates the uncertainty.

Temperature Dependence

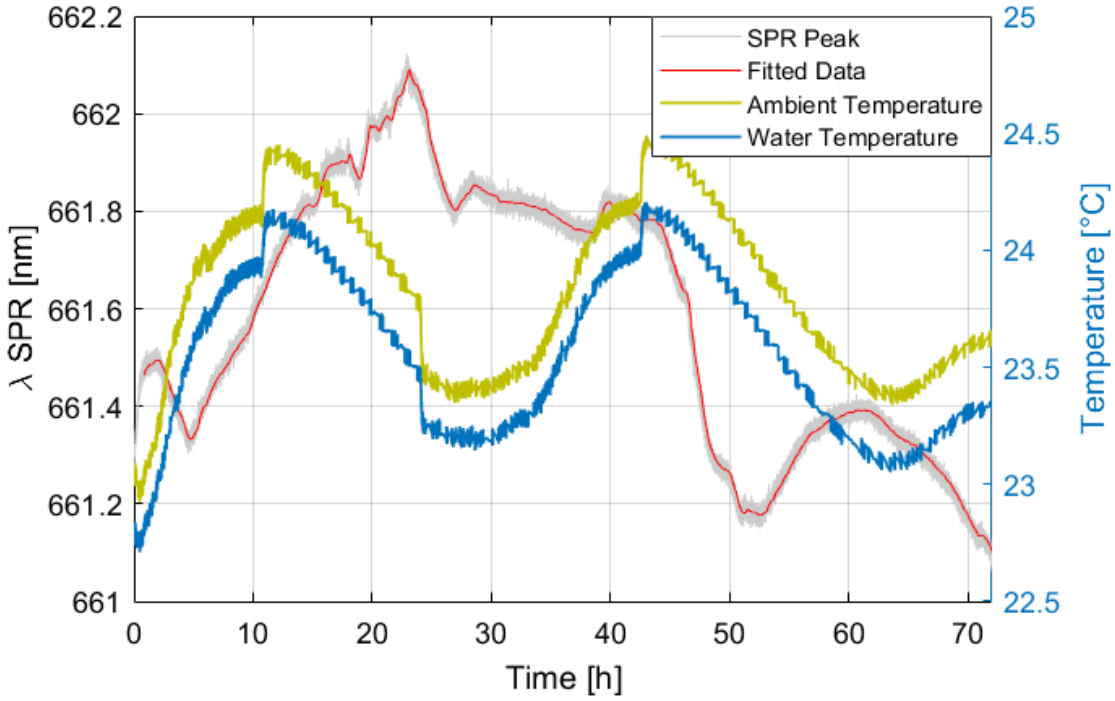

Figure 4.9: Temperature and SPR progress with respect to time during the three day stability test.

Fig. 4.9 illustrates how the temperature has been evolving during the three day test. We believe that the temperature is the main contributor to the drift observed during the test although it is hard to highlight a direct correlation between the curves of the temperature and of the SPR peak trend. We have taken each component of our setup and analyzed the effect of the temperature change in their performance. We have started by isolating the spectrometer and exposing it to

higher temperatures compared to the room temperature. During this test no relevant spectrum distortion has been noticed, thus no relevant drifts can be ascribed to the impact of temperature on the spectrometer. On the contrary, we noticed a non negligible spectral distortion when the same test was performed on the LED source. The LED was placed in an environmental chamber and exposed to temperatures of 25 °C, 30 °C, and 35 °C while the rest of the setup was maintained in room conditions. Fig. 4.10 graphically illustrates how the normalized spectrum of

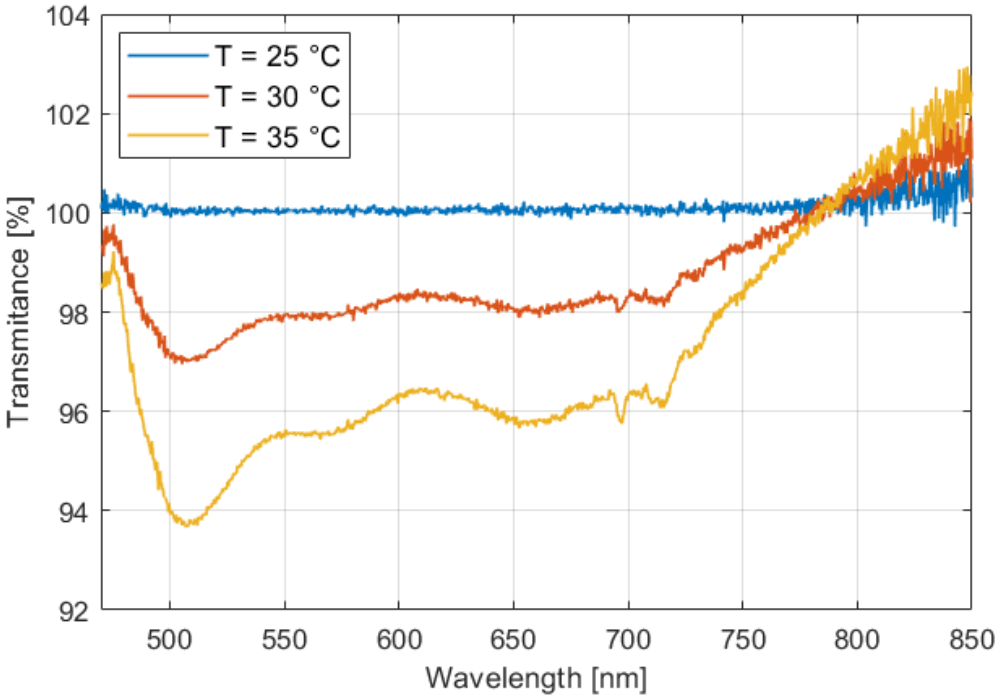

Figure 4.10: Normalized spectrum of the broadband LED for three different temperatures, respectively 25 °C, 30 °C, and 35 °C.

the broadband white LED is impacted by the temperature change. This distortion is clearly responsible of shifts of the SPR peak. Specifically, extracting a random curve from the three day test, the results of this temperature test show that the impact on the LED introduces a blue-shift of about 0.15 nm in the first increment of 5 °C, and then another blue-shift of 0.16 nm in the second increment, thus we can linearize to 0.03 nm/RIU. It has to be pointed out that we have introduced quite a large temperature change to see a fast modification of the reference spectrum, even though this is not what has happened in reality (max 2 °C). It has to be considered that the LED has an appropriate heat sink, thus it is understandable not observing a fast (large) disturbance in the spectrum. The LED spectrum changes with respect to the junction temperature that is effected by the ambient temperature,

but not directly by the ambient temperature. However a relevant shift of the SPR peak could be observed.

After analyzing the thermal effect on the source and the receiver of our setup, we have also analyzed the impact that the change in temperature has on our sensor itself. We have performed an ad-hoc experiment to isolate the liquid and the sensitive part of the sensor, while the rest of the setup remains at room conditions. The liquid container has been placed on top of a controllable hot plate while the temperature of the liquid is measured by means of a thermocouple very close to the sensitive area of the sensor. The temperature is increased from 20 °C to 60 °C and the spectra are shown in the Fig. 4.11. The SPR curve has undergone an

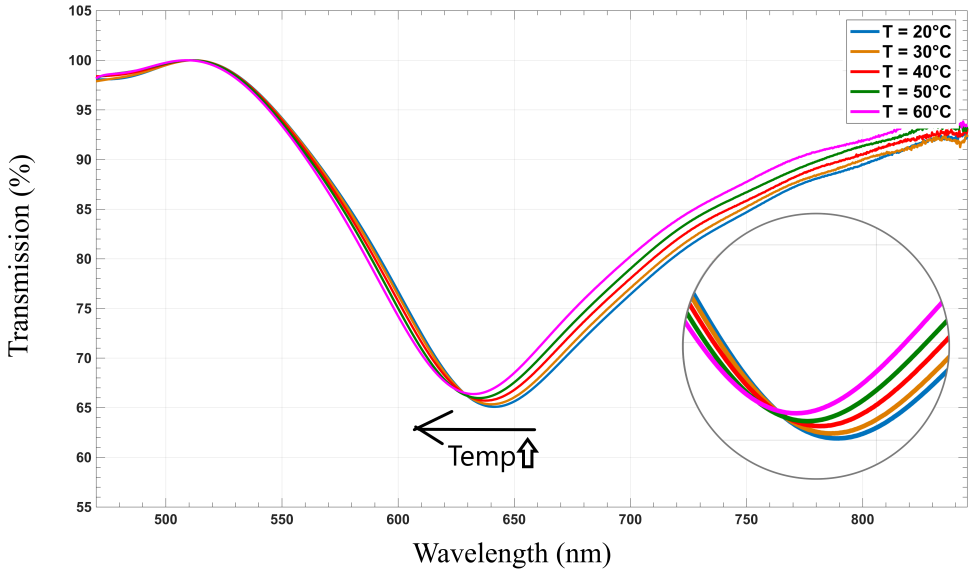

Figure 4.11: SPR curves while the sensor is immersed in water changing temperature in the range of 20 °C to 60 °C.

average blue shift of 0.2 nm/°C and this corresponds exactly to the thermo-optic effect of water, which is the responsible for the change of the refractive index of water with respect to the temperature, is in the order of $10^{-4} RIU°C$ [5]. This parameter introduces the most relevant impact on the long term drifts observed during the three day test. Indeed, a change of 2 °C would introduce an SPR shift of 0.4 nm because of the thermo-optic effect of the water plus a shift of 0.06 nm due to the spectral distortion of the LED. Still to be investigated are the effects that the temperature has on the mode distribution of the optical fiber and on the mobile connectors exploited during the measurements.

4.2 OFSPR Intensity Interrogation

After analyzing and characterizing the OFSPR sensors using the most performant yet expensive setup, we considered a simplified and lower cost version based on an intensity interrogation scheme. Indeed, with such approach, the most expensive part (the spectrometer) will be replaced with a simple photodiode. The setup consists of a red LED at 700 nm (LED700-04U - Roithner Lasertechnik) and a simple photodiode (SPD64-04 - Roithner Lasertechnik). The photodiode output is connected to a trans-impedance amplifier exploiting an op-amp with a trans-impedance of 1 MΩ and a capacitor of 1.5 nF. The cutoff correspondent cutoff frequency (-3dB) is about 106 Hz. In the mean time the LED is driven at controlled current regime, by a current driver schematically illustrated in Fig. 4.12. The signal of the LED

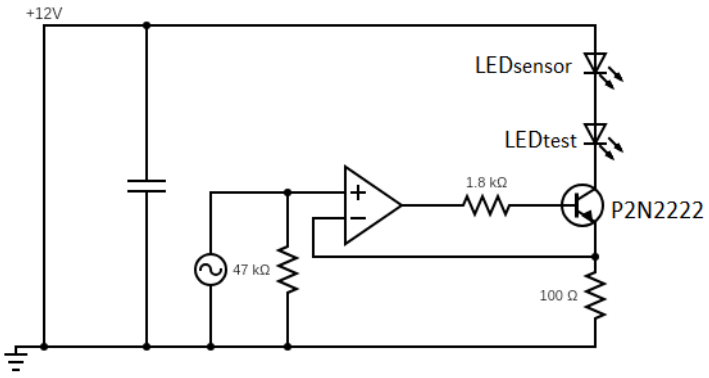

Figure 4.12: Electronic circuit schematics of the LED current driver

is set at offset of 600 mV, amplitude of 1 Vpp and frequency of 22 Hz. The output of the trans-impedance amplifier is received by a data acquisition board (DAQ NI6036) with an incorporated 16 bit ADC. The LED is controlled with a 22 Hz sinusoidal signal in order to discard the background noise, which might come due to slower movements in the environment. Eventually, we perform a Fourier transformation to the received signal and read only the peak signal at the 22 Hz. The stored signals have a value in the range of few mV and the full range of the ADC is set at ±50 mV corresponding to a quantization voltage $V_q = 1.5 \times 10^{-6}\ V = 1.5\,\mu V$.

Moreover, the setup is created by cutting the fiber sensor really short, around 7 cm with both the LED and the PD glued to the extremes of the sensitive area. The setup is really compact with dimensions of $10 \times 3 \times 3$ cm including the sensor, the red LED, the PD, a thermistor and the circuitry. Fig. 4.13 shows a photo of the device. The LED and the PD are incapsulated in a silicone protection so that they can be immersed together with the sensor in the liquid under test. This creates

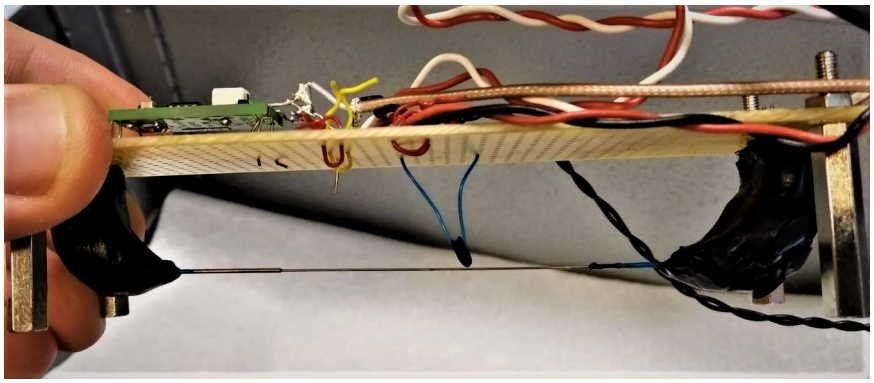

Figure 4.13: Photo of the intensiometric OFSPR device including the LED, PD, thermistor and the circuitry in a compact design.

a more stable environment, with all the setup at the same temperature, and no mechanical disturbances coming from the outer environment to the optical fiber. The main idea behind this "stable" setup is to compare it with the wavelength interrogation one in terms of long terms stability and temperature dependence.

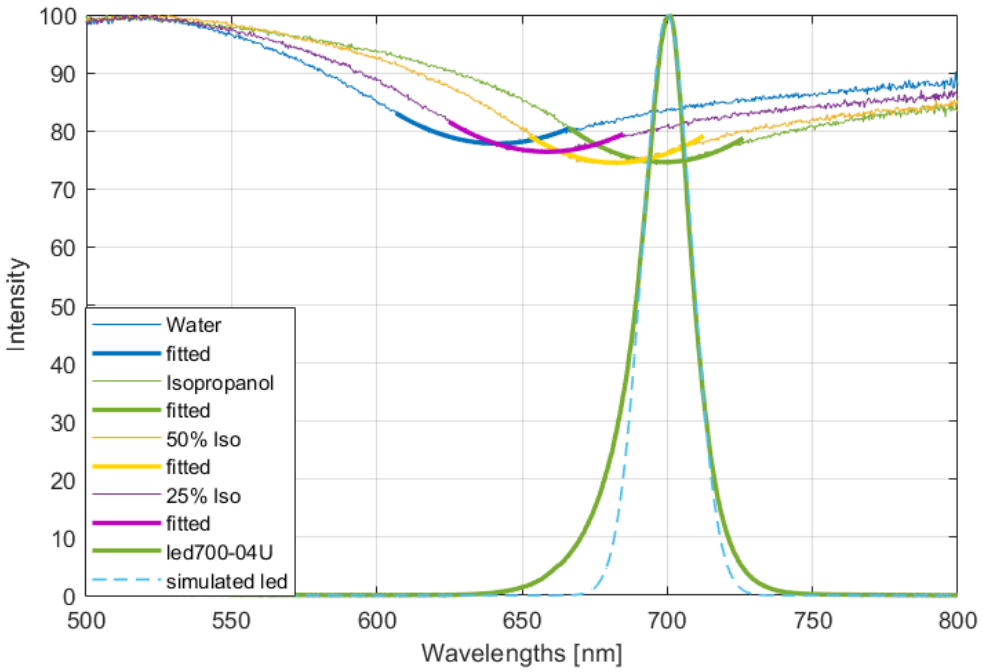

Figure 4.14: Four SPR spectra with the respective 2nd polynomial fitting; LED at 700 nm simulated and experimental spectrum.

Prior to its actual use in the intensiometric setup, the sensor has been characterized using the wavelength interrogation setupin order to "predict" its potential behavior. Fig. 4.14 shows the SPR curves of the sensor immersed in 4 different solutions (100% Water, 25% Isopropanol, 50% Isopropanol, and 100% Isopropanol) with the respective refractive index values (1.333, 1.3438, 1.3545, and 1.376). In this case we have chosen an LED at 700 nm in order to guarantee that all the curves have the peak at the left side, thus the measurements will show a decreasing trend with the increment of the RI values.

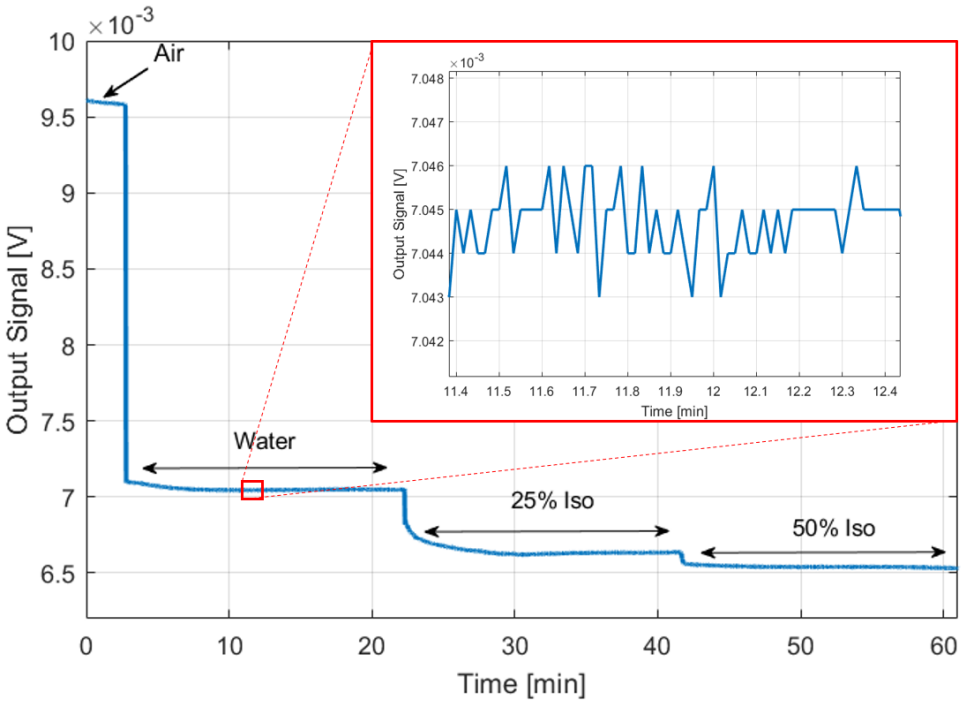

Figure 4.15: Characterization of the OFSPR in intensity interrogation for 3 different RI values (1.333, 1.3438, and 1.3545); test duration 1 hour; the red box shows a 1 minute zoom in.

Fig. 4.15 shows the graph of an experiment that has lasted around 1 hour storing a sample every second. This time we have kept the same liquid (same RI) for relatively longer time compared to the previous one, in order for the water and alcohol to fully mix and the system to stabilize. In the red highlighted box is zoomed in what occurs in a selected minute of the measurements, and it can be seen that the variation is in the order of the quantization voltage ($\pm 1.5\,\mu V$). Strangely, the sensor shows a lower sensitivity ($-10\,mV/RIU$) in the transition from 25 to 50% of isopropanol concentration compared to the transition from water to 25% isopropanol concentration ($-39\,mV/RIU$). However, in this case it is hard to

compare the results with the those obtained from wavelength interrogation, because the fiber is cut short, which means the NA loses its "filtering power" and not only the guided modes interact with the metal layer.

4.2.1 Stability Analysis

In order to test the sensor stability both in long and short terms, the sensor was left immersed in the water alcohol mixture with 50% alcohol concentration for two more days. The test result is shown in Fig. 4.16. The graph shows the output signal (blue solid line) measured at the pins of the trans-impedance amplifier and also the temperature of the liquid where the test is performed (red dashed line). It can be clearly seen that there is a direct relation between the two signals. From the figure

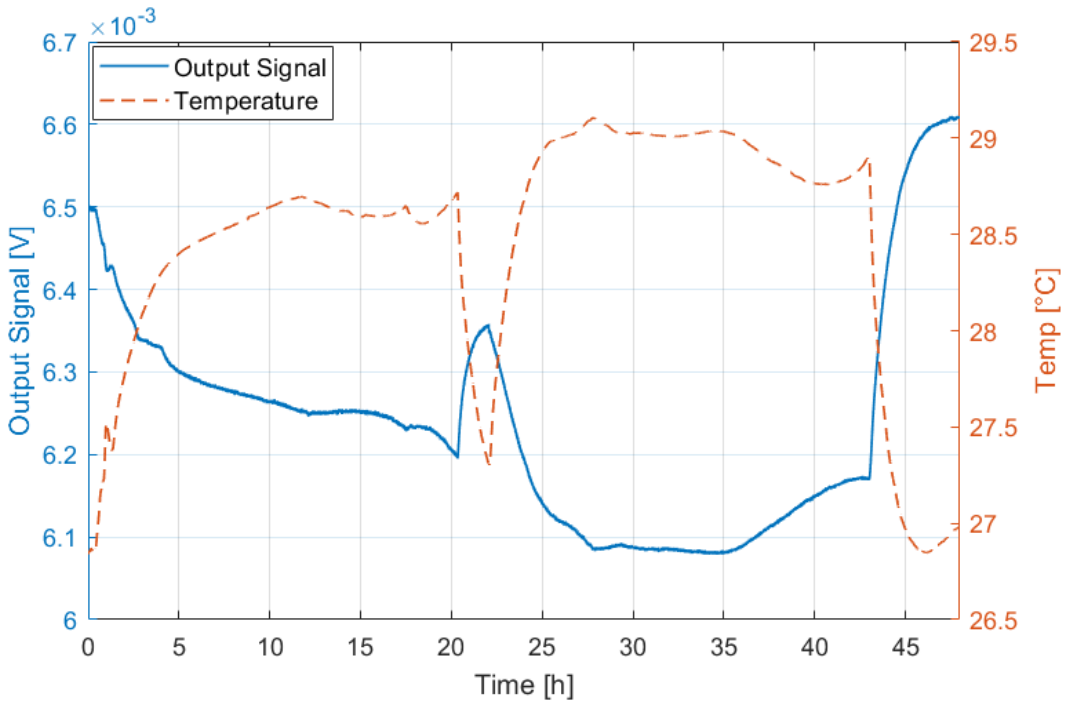

Figure 4.16: Two day stability test of an intensiometric sensor immersed in a 50% concentrated Isopropanol/water mixture; the blue solid line is for the signal output, while the red dashed line is for the liquid temperature.

we can understand that the in long term the signal is dominated by a drift driven by the effect of the temperature. Still the signal is characterized also by its short term instabilities, referred to as signal noise. We have analyzed the signal in intervals of 1, 10 and 60 minutes, by taking the standard deviation of all the intervals occurred during the two day test. The worst (highest) standard deviation found among the 1 minute intervals is 3.6 µV,corresponding to $9.2 \times 10^{-5} RIU$, among the

10 minute intervals is 20 µV, corresponding to $5.2 \times 10^{-4} RIU$, and among the 60 minute intervals is 79 µV, corresponding to $2 \times 10^{-3} RIU$. It is clear that already in the 10 minute interval, the uncertainty is dominated by the drift rather than the noise floor, as the standard deviation is almost an order of magnitude higher.

Temperature Dependence

As previously mentioned, the long term uncertainties of the signal is dominated by a drift that we visually correlated to the temperature change in the liquid. Fig. 4.17 shows the signal output with respect to the measured temperature, and confirms what is visually noticed in the previous graph of Fig. 4.16. The fitted

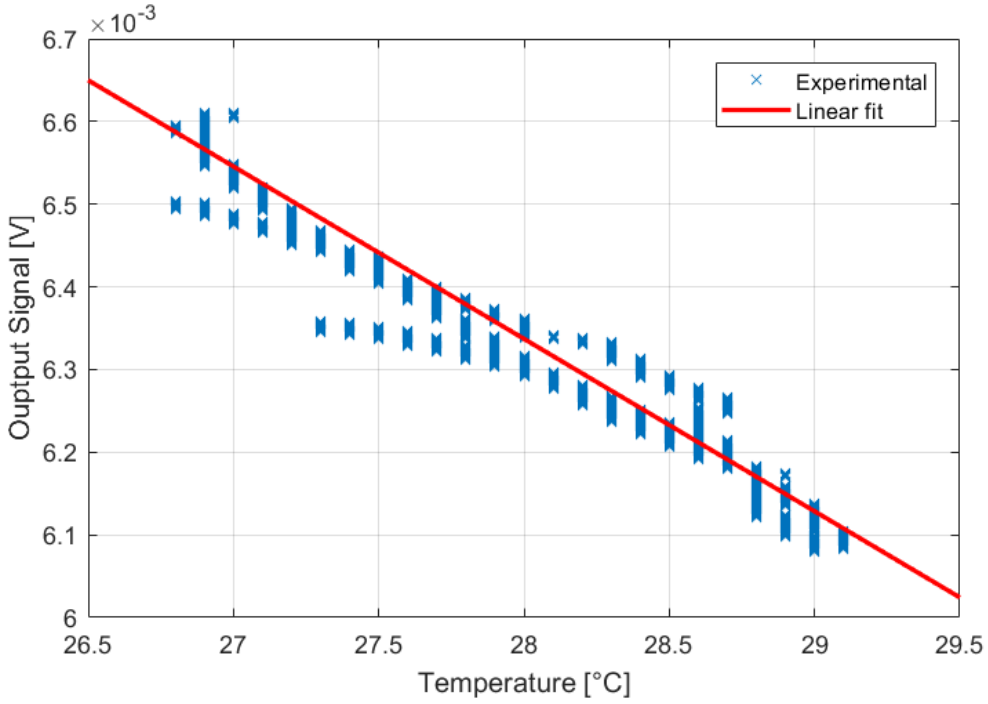

Figure 4.17: Output signal with respect to liquid temperature, during a 2 day test.

curve has a slope of $-2.08 \times 10^{-4} V/°C$ ($R^2 = 0.9146$), which, if converted in RIU (as of sensitivity), would correspond to a value of $\delta n = -5.3 \times 10^{-3} RIU/°C$. Based on existing literature and proved also by our experiments described above, this is not a reasonable RI modification due to the change in the temperature (thermo-optic effect of the liquid) as liquids have a characteristic thermo-optic effect of $-10^{-4} RIU/°C$ [5]. Therefore, from this short analysis we can deduce that this temperature dependence of the signal does not arise from the SPR phenomenon. Excluding the option of the thermo-optic effect of the liquid under test, we can

have a look at the LED and PD characteristics with respect to temperature. In the literature it can be found that the responsiveness of the PDs increases with the increment of operating temperature and this factor is of the order of $0.05\%/°C$ [43]. Obviously we can neglect this parameter as well, as the trend shown in Fig. 4.17 is negative and in the order of around $2\%/°C$. There is only one device still to be analyzed in the setup which could possibly bring the measured temperature dependence. The LEDs decrease their output power with the increment of the temperature in their junction, and the junction temperature is definitely dependent on the ambient temperature [44]. However, it is hard to guess what is the impact of a change of ambient temperature with 1 °C in the junction temperature, because this relationship is also dependent on the current flowing, on the isolation of the LED etc.

Temperature confirms to be a really important parameter in the OFSPR sensors. For the wavelength interrogation technique, there is a solution that can be implemented exploiting the same fiber by adding another fictitious sensitive area in series with the previous one covered by a fixed RI material that acts as a reference. In this case the transmitted spectrum will show two peaks at different wavelengths, one that follows the RI of the liquid and the other shifting only in case of temperature change [45]. Of course, in the case of intensity interrogation this solution is not feasible, but it can be adapted by adding a reference sensor in another fiber, placed in parallel, connected to the same LED source, as presented in one of our papers [46]. However, this over complicates the setup, losing its compactness introducing a fiber coupler or bundle. Another simpler option is by just characterizing the final setup with respect to temperature, thus having a calibration curve for each respective temperature of interest.

4.3 Middle Range Setup

Until now we have analyzed two different setups exploiting OFSPR. Obviously the wavelength interrogation, which is also the tradition method for OFSPRs has shown a higher performance both in terms of short and long term measurements. However such high performance is accompanied by a high cost. This was the main motivation to move towards a lower cost setup, which was proved to be valid, nevertheless considering the trade off in performance. The biggest problem in the intensity interrogation setup was the temperature dependence of the red LED's on the temperature. For this reason in this section we will study another type of setup that is somewhat in between the first two, both in terms of configuration and of cost.

This new setup replaces the high quality spectrometer with a lower quality one.

The second spectrometer considered (NIR AS7263) has a slightly different working principle compared to the traditional one, which justifies the lower cost of the device. The device instead of a grating has six selective photodiodes in the range from 600 nm to 870 nm, spatially separated and mounted in the same chip of area 0.47 mm^2, thus it is basically an array of PDs spaced in different wavelengths of the spectrum. It is very compact, has the options to be connected to a PC via SPI (Serial Peripheral Interface) or I^2C (Inter-Integrated Circuit) communication protocols, and has a thermometer incorporated. Meanwhile on the source side we will exploit the super luminescent LED (MBB1F1 - Thorlabs) used for the wavelength interrogation. The difference in the cost of the two setups is purely introduced by the two spectrometers the first with a cost of approximately 5k€ whether the PD array around 20€.

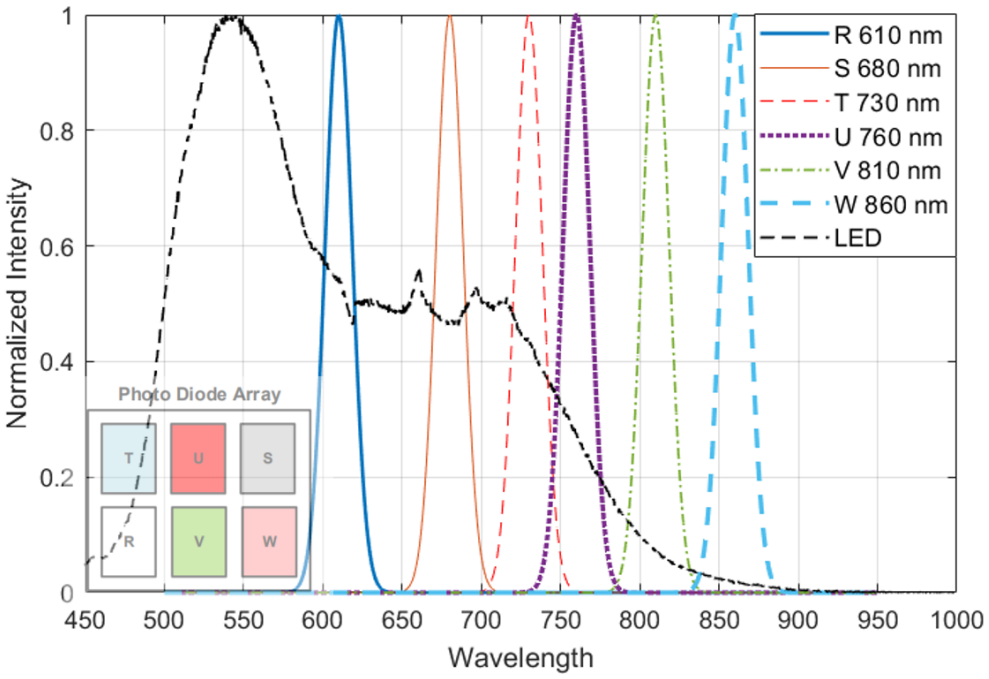

Figure 4.18: Spectral positioning of photodiodes, and LED spectrum (Graph); and spatial positioning in the photodiode array (bottom-left corner)[taken from the data sheet of manufacturer].

The graph presented in Fig. 4.18 illustrates how the photodiodes are spectrally positioned, and on the bottom-left angle of the image is shown how the respective photodiodes are positioned spatially in the array. The PDs have a FWHM of 20 nm and have the respective wavelengths: R = 610 nm; S = 680 nm; T = 730 nm; U = 760 nm; V = 810 nm; and W = 860 nm. While on the other side we have kept

the same LED source (470 nm to 850 nm) that emits very few power for the last 2 photodiodes (V and W) but significant power at the wavelengths of interest.

However we have noticed that the spectrum measured does not match the profile emitted by the LED. This might due to misalignments of the fiber with respect to the photodiode array, because, being physically divided in 6 photodiodes, the spectral shape depends on how much light reaches the various PDs. However, as we are interested in the relative changes, the absolute value can be discarded. We can naturally say that in this case the sensor will be intensity interrogated, rather than wavelength even though the PD array is considered as a spectrometer.

As we are going to consider our measurements only relatively, we can take the photodiode spectra all normalized to 1, not introducing the effect of the LED spectrum. Fig. 4.19 illustrates how the photodiodes stand with respect to the normalized SPR spectra. In order to calculate the relative intensity that the respective

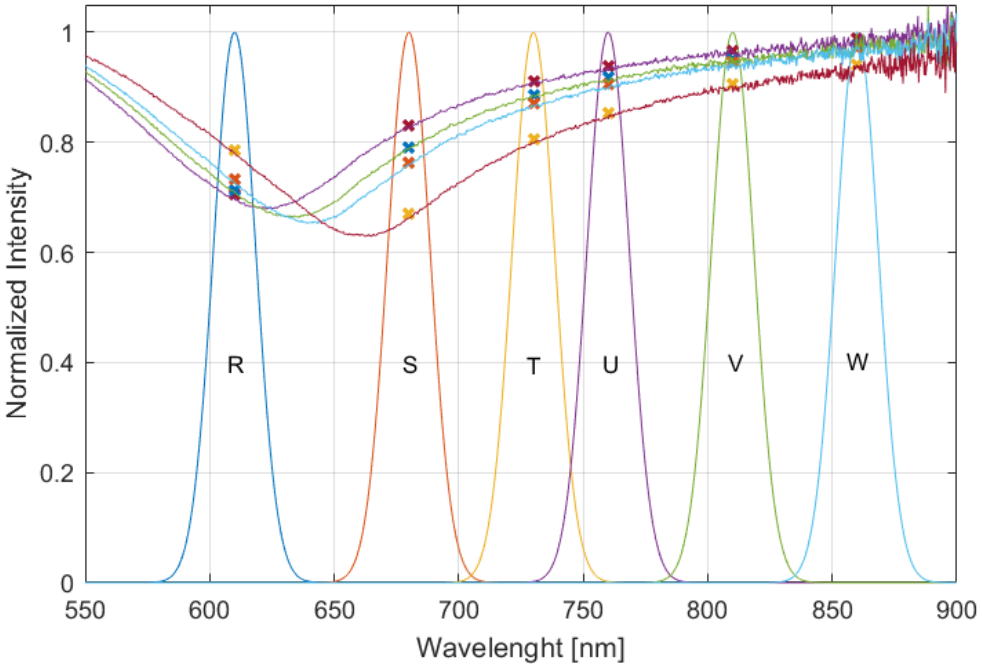

Figure 4.19: Spectral positioning of photodiodes with respect to SPR curves obtained experimentally.

photodiodes will receive, we have to make the product of each two signals of interest and integrate over the wavelength. Let us consider the photodiode R specifically at 610 nm for the first two immersion in water and in 10% concentrated Isopropanol concentrated mixture. The following Eq. 4.2 shows how we proceed to predict the

expected relative values from the respective PDs.

$$Int_{\text{water}} = \int_{\lambda_{\min}}^{\lambda_{\max}} R(\lambda) \cdot SPR_{\text{water}}(\lambda)\ d\lambda \tag{4.2a}$$

$$Int_{\text{Iso10}} = \int_{\lambda_{\min}}^{\lambda_{\max}} R(\lambda) \cdot SPR_{\text{Iso10}}(\lambda)\ d\lambda \tag{4.2b}$$

$$Int_{\text{rel}} = \frac{Int_{\text{water}}}{Int_{\text{Iso10}}} \cdot 100\% \tag{4.2c}$$

where Int stands for intensity, $R(\lambda)$ stands for the profile of the photodiode at 610 nm with respect to wavelength, and $SPR(\lambda)$ the SPR curve immersed in the respective medium. The same approach is valid for any medium and photodiode involved in the experiment. Tab. 4.3 shows the results obtained from the simulations, calculating the convolution between the SPR curves and the selective photodiodes, and the results obtained experimentally. The trends are converging, even though the results do not perfectly match. It can be seen that only the R (610 nm) PD has a positive trend with the increasing RI, and this is conform the expectations because this PD is the only one on the left side of SPR wavelength peaks. Another very interesting fact that can be remarked both in the wavelength and in the intensity interrogation of the sensor is the very small variation during the second step of the measurements. When the transition from 10% Isopropanol to 20% Isopropanol occurs, the sensor seems to be relatively less sensitive to the difference compared to the other steps. This has occurred both when Avantes spectrometer and PD array are used. This is also quite a justifiable result from the simulations. One can see in Tab. 4.2 that even in pure simulations the sensitivity is higher at the step 20% to 40%. However in experiments, the difference is a lot bigger.

Table 4.3: Experimental and simulated results of the PD array for 4 water-isopropanol solutions, RI = [1.333 1.3373 1.3416 1.3502]

	Experimental					
	R	**S**	**T**	**U**	**V**	**W**
Water	1	1	1	1	1	1
Iso10	1.03	0.95	0.98	0.97	0.99	0.99
Iso20	1.09	0.88	0.94	0.94	0.98	0.98
Iso40	1.24	0.70	0.84	0.82	0.97	0.92

Simulated PDs					
R	**S**	**T**	**U**	**V**	**W**
1	1	1	1	1	1
1.02	0.95	0.97	0.98	0.99	0.99
1.04	0.92	0.95	0.97	0.98	0.98
1.12	0.81	0.89	0.92	0.94	0.96

Let us now consider separately the case of photodiode R (610 nm) and S (660 nm), positioned at the most advantageous point with respect to the SPR curve (refer to Fig. 4.19) and with respect to the source spectrum (refer to Fig. 4.18). Fig. 4.20 shows the graphs of the two photodiodes during the test of 20 minutes while the sensor is immersed in 4 different water-Isopropanol solutions. From the graph it can be seen that the two photodiodes do not have a linearly correlated response

with respect to each other. This because they are positioned in different points of the SPR curve. Closer the PD is to the SPR peak, less linear becomes its response, while further it gets to the right of the spectrum it becomes more linear but less sensitive.

The experiments exploiting this setup are left to a proof of concept level, without

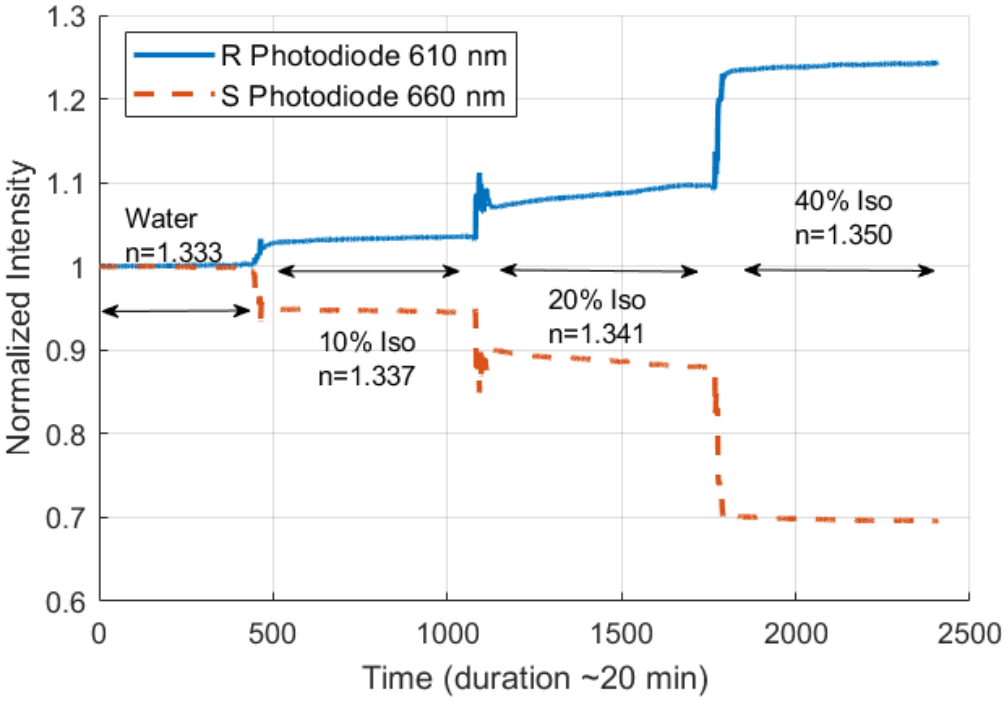

Figure 4.20: Normalized intensity of R (610 nm) and S (660 nm) over a 20 min characterization test with the sensor immersed in 4 different solutions.

entering in many details regarding the stability and uncertainties. Nevertheless, the setup has shown promising results, performing with high sensitivity. This setup has an important advantage compared to the pure intensiometric one which consists of measuring intensities in both sides of the SPR curve simultaneously. This feature can be exploited to compensate the intensity fluctuations of the source and to discriminate them from the changes in RI of the liquid under test. For example, if we consider adding some isopropanol to our water under measurement, the R-PD will have a positive response while the S-PD will have a negative response (as shown in Fig. 4.20). Instead if an intensity fluctuation is occurring due to let's say increase of room temperature, both the PDs will have a negative response. For this reason we have considered this setup to be in the middle range, both in terms of performance and of cost (white LED + PD array cost more than red LED + single PD). However a full characterization needs to be performed before giving a

final verdict to this solution. This setup might have significant problems introduced by mechanical disturbances, as the PDs are spaced physically in the chip, and the modal distribution of the fiber might change the received light intensity in each of them.

Chapter 5

SMS Optical Fiber Sensors

This chapter will be dedicated to another OF sensor studied and developed during my Ph.D. work. It will have a very similar mini-organization as the thesis itself, starting with a short theoretical background, continuing with some simulations and concluded with some experimental work to prove the concept. The chapter is included in this thesis, not only because it describes a sort of "minor" carried out simultaneously with the "major" (the OFSPR sensor), but mainly because it presents a sensing technique that can complement the SPR sensors in a first step towards a multi-parameter sensor.

The sensor analyzed in this chapter is an interferometric one, implemented exploiting the beating of the modes at the interface between multi-mode and single-mode fibers, in a configuration known as SMS (single mode - multi mode - single mode) to highlight that it is fabricated by sandwiching a short piece of a multi-mode fiber between two single-mode fibers. Such a sensor can be exploited to measure different parameters (for example, temperature and with a sensitivity that can be much larger than that of the market standard represented by fiber Bragg gratings), but we have thought to use it as an hot wire anemometer to evaluate the velocity of the flowing liquid for which the SPR sensor monitors the changes in the composition.

5.1 Theoretical Background

As the name suggests the sensors, consists of a section (few cm) of MM fiber spliced between two SM fibers. At the first SM-MM junction the various modes of the multi-mode fiber are excited and propagate; then at the second junction the power that is transferred to the collecting single-mode fiber depends on the field distribution, which in turn depends on the phase difference accumulated by the various modes while propagating in the multi-mode section. Particularly interesting for the excellent combination between simplicity of operation and sensing

performance is the case of using for the MM section a two-mode fiber or a single-mode fiber operated close to the cut-off wavelength. Essentially this case can be seen as a Mach-Zehnder interferometer (MZI), where the two modes in the MM section represent the two arms, with the same propagation length, but propagation constant, hence different phase velocity. It has to be pointed out, however, that the similarity holds for the physical principle only and not in the setup because in the traditional MZI, the two branches are physically separated by beams splitters or couplers. Fig. 5.1 schematically illustrates a traditional MZI on the left and a SMS structure on the right.

A two-mode fiber (so with only the first higher order mode LP_{11} above the cut-off

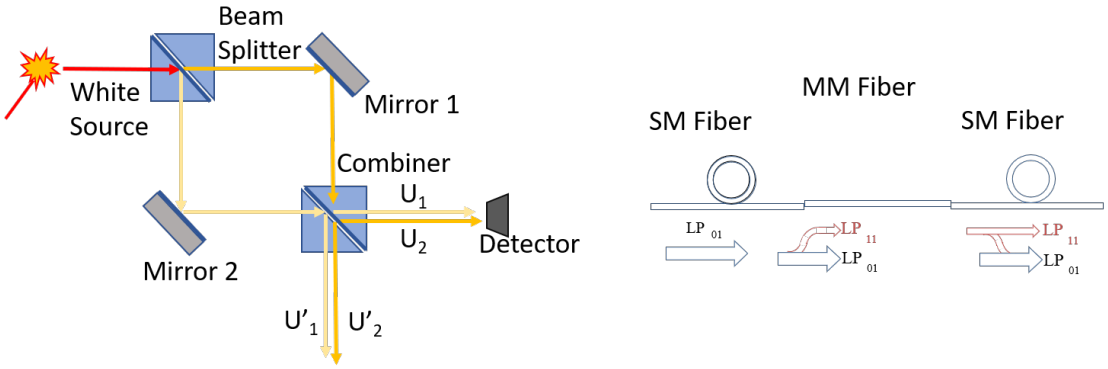

Figure 5.1: Schematic illustration of a Mach-Zehnder Interferometer (left) and a SMS fiber interferometer (right).

besides for the fundamental LP_{01} mode) can be obtained operating in the second or third optical communication window a fiber designed to be single-mode at a longer wavelength, such as the SM2000 fiber by Thorlabs, which is single-mode around 2000 nm and supports two guided modes in the 1300 nm to 1600 nm range. Alternatively, Bend Insensitive Fibers (BIFs) can be used for the intermediate section. BIFs are single-mode fibers in the third optical communication window (so around 1550 nm) in which the field confinement is increased to lower the sensitivity to bending; in turn this increase leads to working close to the cut-off wavelength, so that for the shorter wavelength edge of the single-mode bandwidth the higher order mode is only poorly attenuated and for short spans the fiber practically behaves as a two-mode fiber. This condition can be easily obtained using a BIF in the second optical communication, around 1310 nm. The excitation of the first higher order mode at the first SM-MM junction requires a splice with a lateral offset, as shown in Fig. 5.1 (right).

5.1.1 Interference

[1]Considering two monochromatic waves as described in the following two equations Eq. 5.1):

$$U_1 = \sqrt{I_1}\ exp\ (j\phi_1) \tag{5.1a}$$

$$U_2 = \sqrt{I_2}\ exp\ (j\phi_2) \tag{5.1b}$$

their superposition would have the same frequency and the complex amplitude expressed as $U(r) = U_1(r) + U_2(r)$. The intensity of the superimposed wave can be expressed as in Eq. 5.2:

$$I = |U|^2 = |U_1 + U_2|^2 = |U_1|^2 + |U_2|^2 + U_1^* U_2 + U_1 U_2^* \tag{5.2a}$$

$$I = I_1 + I_2 + 2\sqrt{I_1 I_2}\ cos(\phi) \tag{5.2b}$$

where ϕ_1 and ϕ_2 are the phases of each wave and $\phi = \phi_1 - \phi_2$. This relation, known as the interference equation, demonstrates that the intensity of the superimposed wave is sensitive not only to the amplitudes of the elementary waves but also to their phase difference. The phase shift $\phi = kd = 2\pi d/\lambda = 2\pi nd/\lambda_0$ of a wave depends on its propagation constant k, hence on the wavelength λ and on the RI of the propagating medium, and on the propagation distance d.

5.1.2 Optical Fiber - Modes - V Number

In the two-mode SMS fiber interferometer, the propagation distance d is the same for both the LP_{01} and LP_{11} modes, but they propagate with different phase velocity and therefore with different effective refractive index n_{eff}. In optics it is quite common to express the number of modes in terms of the normalized frequency V expressed as follows (Eq. 5.3):

$$V = \frac{2\pi}{\lambda}\, a\, \sqrt{n_{\text{core}}^2 - n_{\text{clad}}^2} \tag{5.3}$$

where a is the core radius and $n_{\text{core}}, n_{\text{clad}}$ are the core and cladding RI, respectively. V is a dimensionless parameter useful in determining the cutoff wavelength of each mode, the mode volume, number of modes in a multi mode fiber, etc. For instance, $V < 2.405$ is the condition that guarantees a single-mode regime, while for $2.405 < V < 3.83$ the fiber supports only two guided modes. The graph Fig. 5.4 shows the dispersion curves of the first LP modes with respect to the V number. The graph clearly illustrates that for the same V number, thus the same wave-

[1]The equations in this section are obtained from [47] Chapter 2.

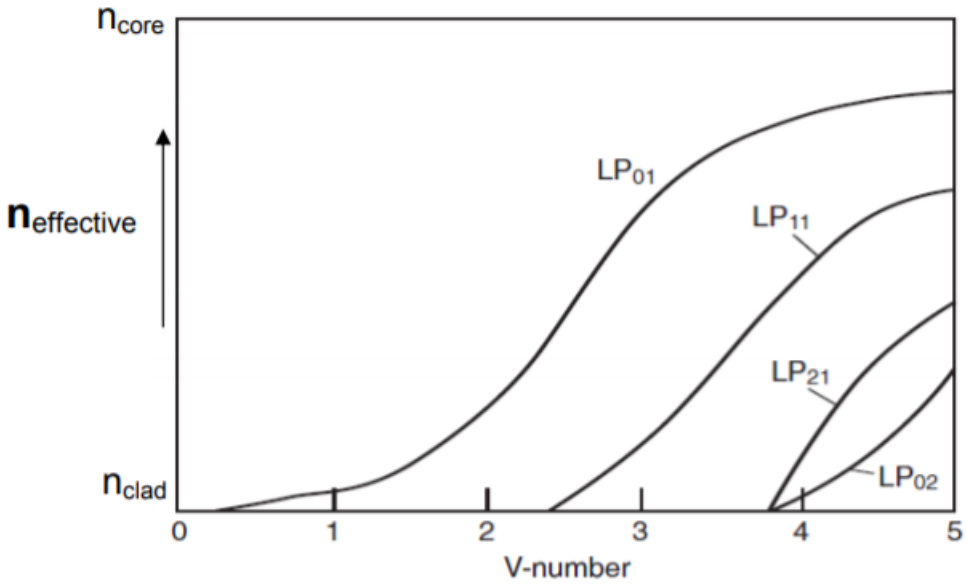

Figure 5.2: Propagation constant β with respect to V number for the first 4 modes [48].

length, the fundamental mode LP_{01} has a higherhigher propagation constant, thus it sees a higher effective index that the first higher order mode. It is exactly this difference that based on Eq. 5.2b, guarantees a phase shift between the propagating modes.

The dispersion equation for the $LP_{l,m}$ mode satisfies the following Eq. 5.4:

$$\frac{J_l(U)}{U\ J_{l-1}(U)} = -\frac{K_l(W)}{W\ K_{l-1}(W)} \tag{5.4}$$

where J and K are respectively the Bessel functions and modified Bessel functions of order l, and U and W are the propagation constants in core and cladding respectively.

The physical principle of the SMS sensor is the interference pattern created from the superposition of the fundamental mode and the first higher order mode. As previously mentioned, this interference pattern depends totally on the phase shift ϕ accumulated by the two propagating modes, which is function of the travelled distance and of the modal effective refractive index. Temperature is a parameter that affects both parameters: the distance by thermally expanding or shrinking the MM fiber and the RI due to the thermo-optic effect of silica. In particular, increasing the temperature with by a δT, the RI of glass decreases, while the propagation length increases. Nevertheless the thermo-optic effect dominates and the spectrum red-shifts when temperature increases.

5.2 Simulations

In this section we discuss the mathematical model of an SMS sensor simulated in MATLAB. As previously mentioned, the $LP_{\mathrm{l,m}}$ can be mathematically described by the Bessel functions as described in Eq. 5.4. The field of the single-mode fiber

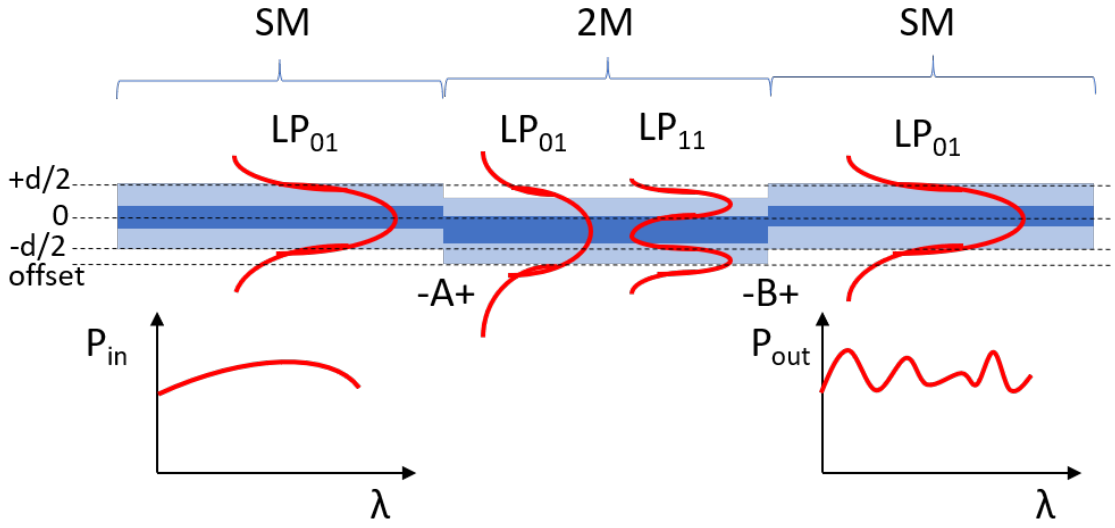

Figure 5.3: Schematic illustration of an SMS sensor.

at the first junction must be written in terms of the modes of the two-mode fiber: calling with C_1 the coupling coefficient $LP_{01}|_{\mathrm{SM}} \Rightarrow LP_{01}||_{\mathrm{MM}}$ and C_2 the coupling coefficient $LP_{01}|_{\mathrm{SM}} \Rightarrow LP_{11}||_{\mathrm{MM}}$, we have the following Eq. 5.5

$$C_1 = \int_0^{d/2} |E_{\mathrm{sm}}^{01} \cdot E_{\mathrm{mm}}^{01}|^2 \,\mathrm{d}\,x \tag{5.5a}$$

$$C_2 = \int_0^{d/2} |E_{\mathrm{sm}}^{01} \cdot E_{\mathrm{mm}}^{11}|^2 \,\mathrm{d}\,x \tag{5.5b}$$

where E_{sm}^{01} is the field profile of the LP_{01} mode of SMF, and E_{mm}^{01} and E_{mm}^{11} are the field profile of the LP_{01} and LP_{11} modes of the MMF, respectively. The field profile at the right end side of the MMF can be described as in the following Eq. 5.6:

$$E_{\mathrm{B}}^{-} = C_1 \cdot E_{\mathrm{mm}}^{01} \exp\left(-j2\pi\frac{L}{\lambda}n_0\right) + C_2 \cdot E_{\mathrm{mm}}^{11} \exp\left(-j2\pi\frac{L}{\lambda}n_1\right) \tag{5.6}$$

where E_{B}^{-} is the field profile at the left side of the B intersection (Fig. 5.3), L is the length of the MM fiber, and n_0 and n_1 are the effective indices of LP_{01} and LP_{11} in the MM section, respectively. Finally, in order to evaluate the power collected by the second SMF (i.e., in section B+), the field profile expressed in terms of the

modes in B- must be projected onto the fundamental mode distribution of the SMF.

We have simulated different setups analyzing the impact of the offset and of the MM section length to choose the best design parameters. Fig. 5.4 shows the V

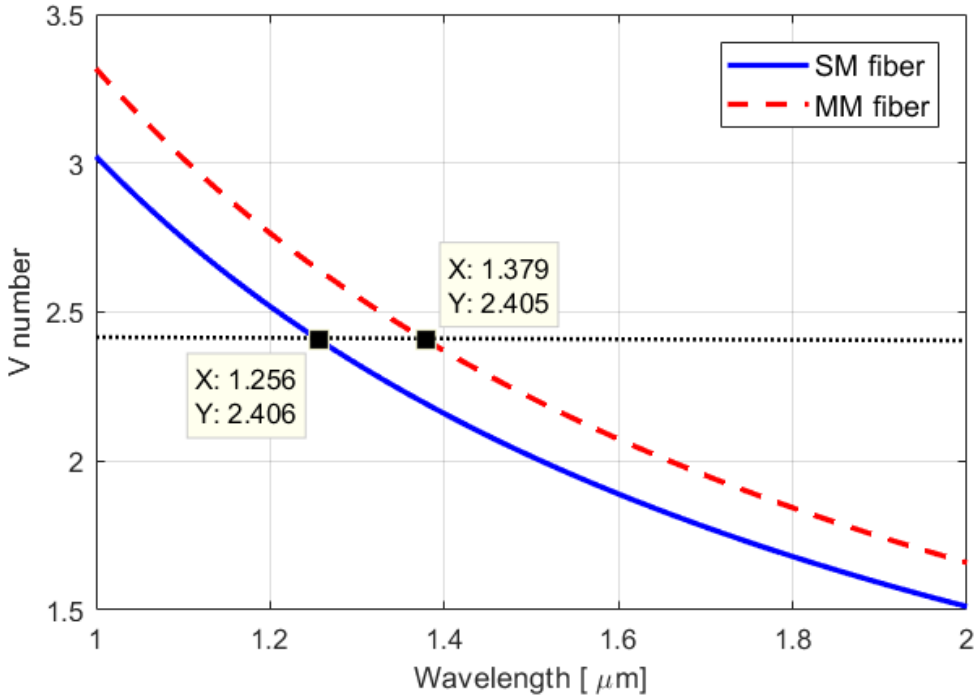

Figure 5.4: V number of the considered fibers with respect to wavelength.

number of the considered fibers with respect to wavelength. The blue solid line is for the V number of the SM section,evidencing the cut-off wavelength at 1256 nm, while the red dashed line is for the MMF, which has the cut-off at 1379 nm. This means the range 1256 nm $< \lambda <$ 1379 nm covers the wavelengths of our interest. Below 1256 nm both the fibers allow 2 modes or more, and above 1379 nm both the fibers are sing-mode, thus no interference is expected.

Fig. 5.5 shows the interference pattern for five different splicing shifts from 0 to 4 micron. From the graph it is clear that the larger the offset, the less power is transmitted. Actually, this result perfectly matches the experimental tests, because the mismatch between the cores in the splicing process results in transmittance power loss. However, in an interference spectrum rather than the total transmitted intensity, the most important parameter is the fringe visibility. Fringe visibility of an interference pattern can be quantified mathematically by the following Eq. 5.7:

$$V = \frac{I_{\max} - I_{\min}}{I_{\max} + I_{\min}} \cdot 100\% \tag{5.7}$$

The visibility is a parameter which provides information in relative terms (ratio) rather than absolute, thus it is better visualized in logarithmic scale. Fig. 5.5 illustrates the plots of the interference patterns for different offset splicing in the logarithmic scale. The graph clearly shows that the splicing offset has an impact

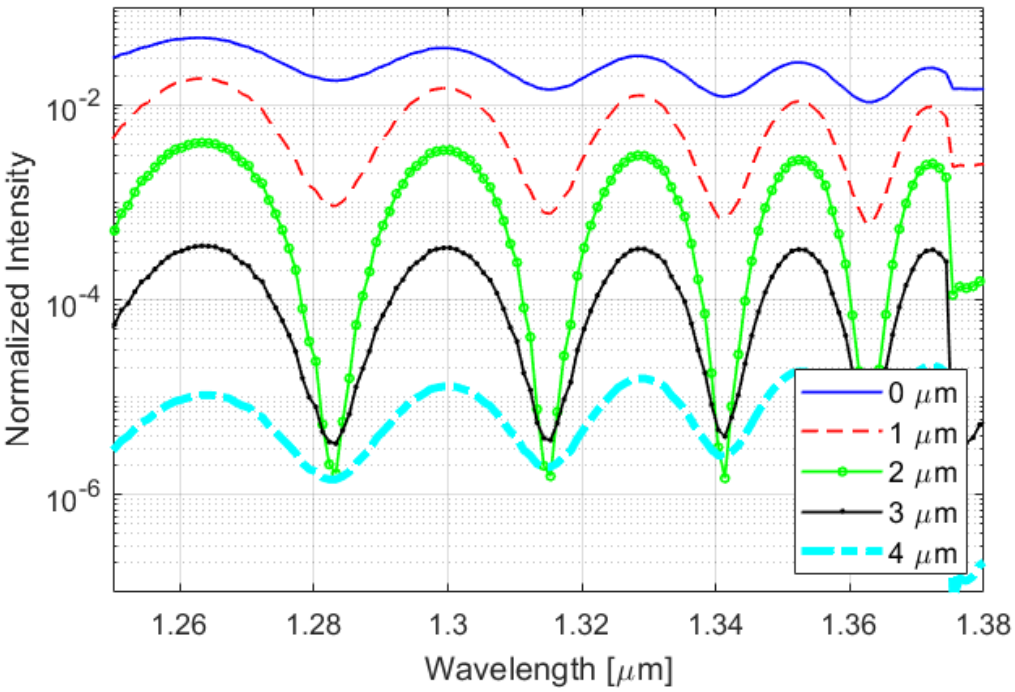

Figure 5.5: Interference pattern with respect to splicing offset, logarithmic scale.

on the fringe visibility. The optimum offset in these terms seems to be 2 µm with a visibility $V = 99.9$ % and the worst case when no offset is introduced with a visibility $V = 64.1$ %.

The other very important parameter of the SMS interferometer is the length of the MM section, where the interference happens. The length of the interferometer in inversely proportional to the free spectral range (FSR) of the interference pattern. FSR is defined as the space (in wavelength) between two consecutive fringes and is expressed as in Eq. 5.8:

$$\Delta\lambda_{\mathrm{FSR}} = \frac{2\pi}{L}\left|\left(\frac{\delta\beta}{\delta\lambda}\right)^{-1}\right| \tag{5.8}$$

We already found that the optimum splicing offset is 2 µm, so for the next part of the simulations we will keep splicing offset at the optimal value while varying the MM fiber length. Fig. 5.6 shows the interference pattern curves for 4 different MM fiber lengths. It is clearly visible that the FSR gets halved when L doubles.

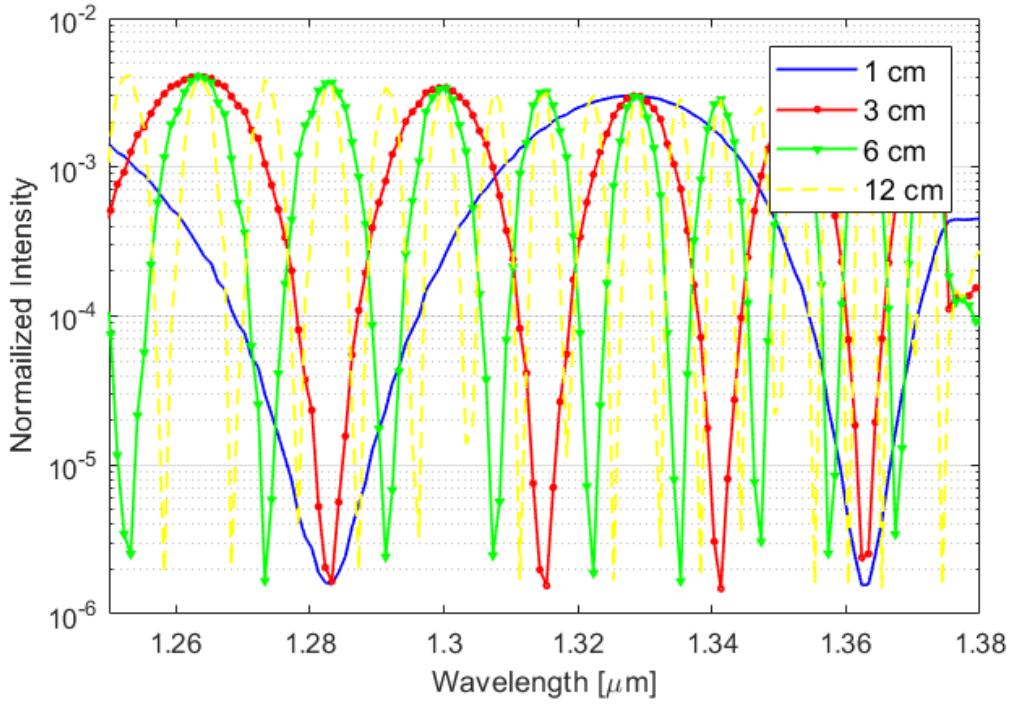

Figure 5.6: Interference pattern for different MM fiber lengths, 1, 3, 6 and 12 cm.

5.3 Experiments

The scope of the experiments is mainly to reach a proof of concept level. The sensor is aimed to be exploited as an OF based hot wire anemometer, by monitoring the interference pattern of the SMS hetero-structure fiber. The first set of the experiments aim to characterize the SMS sensors in terms of temperature and guarantee a real time and non hysteric response to temperature changes. On one side the fiber is connected to a super continuum generator (SuperK - NKT Photonics.) and on the other side the light is collected by an optical spectrum analyzer (OSA).

5.3.1 Simulations Vs Experiments

Firstly let us see how the experimental curves compare to the simulated ones. Fig. 5.7 shows how the FSR changes with respect to $1/L$ (MM section length) in theory blue curve (squares) and experimentally red curve (crosses). The table placed at the bottom right angle of the graph shows the exact data points plotted in the graph. The simulations match quite well the experiments. The Δn_{eff} of the LP_{01} and LP_{11} in the MM section is around 2.5×10^{-3}. The small difference

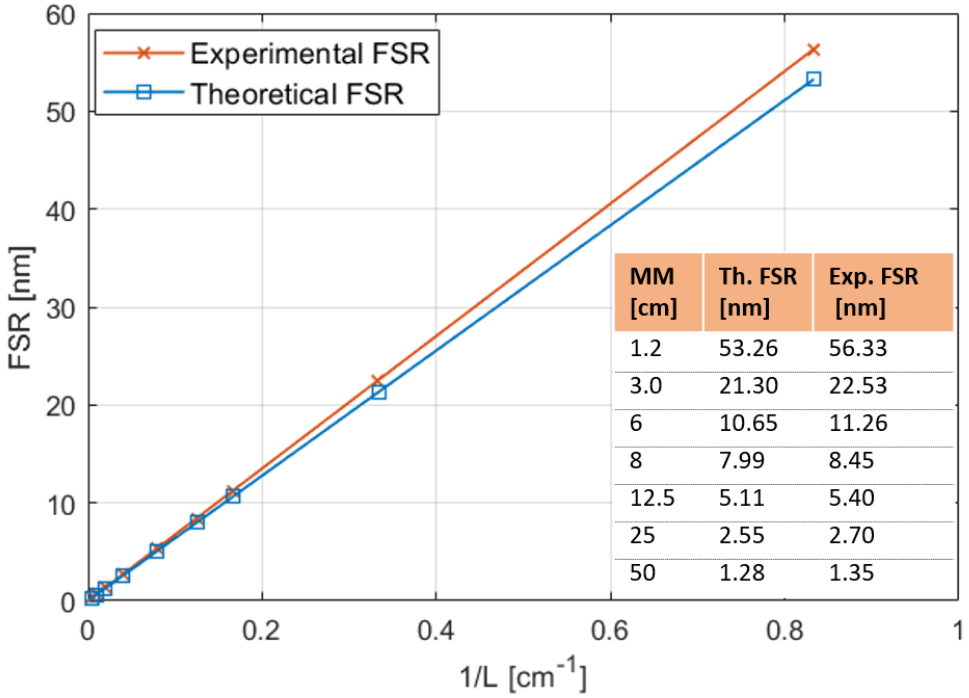

MM [cm]	Th. FSR [nm]	Exp. FSR [nm]
1.2	53.26	56.33
3.0	21.30	22.53
6	10.65	11.26
8	7.99	8.45
12.5	5.11	5.40
25	2.55	2.70
50	1.28	1.35

Figure 5.7: FSR with respect to $1/L$ MM section length, theoretical - blue squares, experimental red crosses

between the theoretical and the experimental results in this case can be justified by the way fiber length is measured, cut and spliced. The three processes introduce uncertainty to the length of the MM fiber length that was used.

5.3.2 Temperature Characterization

Instead for the temperature characterization the fiber is positioned on top of a temperature controlled hot plate, and the temperature is increased slowly while saving the spectrum of the transmitted light. Actually only the sensitive part of the fiber, thus the MM section is set up on top of the hot plate Fig. 5.8 shows the experimentally obtained interference pattern of an SMS sensor while the plate is heated at 22, 80 and 150 °C and then cooled down back to 22 °C. The sensor is composed of two standard SMF28 fiber sandwiching a 6 cm of SM2000 fiber, with an offset splicing of 3 µm. Increasing the temperature, the fringes red-shift and the sensor has a sensitivity of 50 pm/°C. This value is quite higher compared to similar OF based temperature sensor. For instance typical FBGs exhibit a sensitivity of 10 pm/°C [49]. Nevertheless, sensitivity is only of the important parameters that characterize an OF sensor, thus in different situations, different setups are preferred.

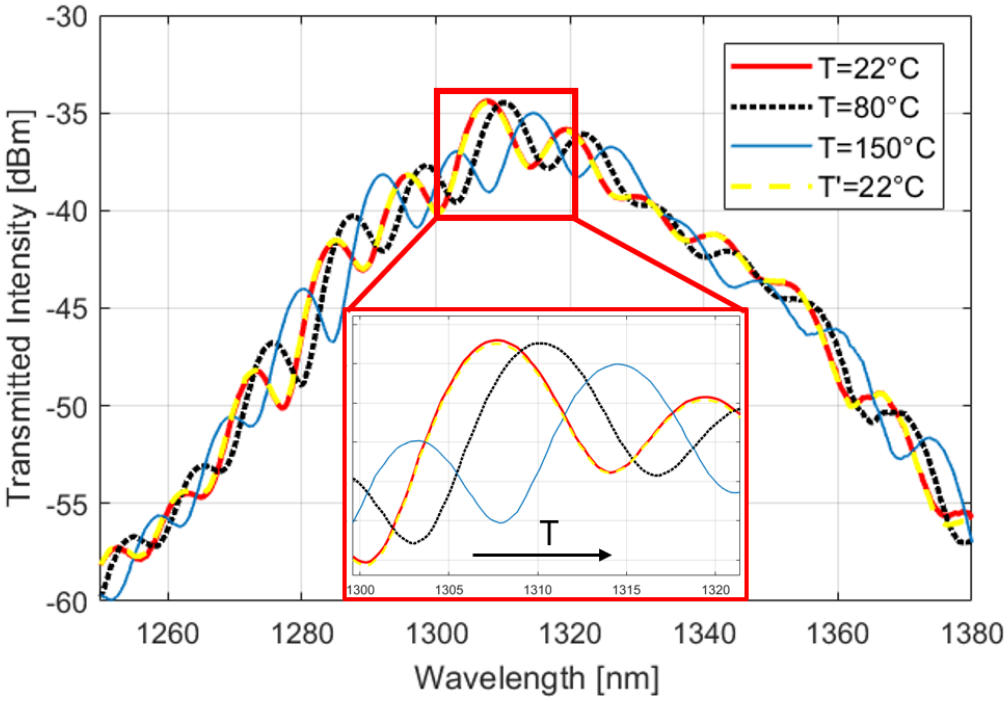

Figure 5.8: Interference pattern and temperature dependence of a SMS sensor with 6 cm of MM section.

5.3.3 OF SMS Anemometer

Until now we have proved that SMS fiber hetero-structures can be exploited as highly sensitive thermometers and they can be perfectly designed based on the mathematical model of the superposition of the first two fundamental modes. Nonetheless similar results have been already published in literature [50, 51]. The scope of our research was to push this topic further and to find another application for the SMS OF sensors, which could be also applicable to the main topic of this Ph.D. work. The hetero-structure design of the SMS sensor can be perfectly exploited as an hot wire anemometer.

In order to be able to exploit the SMS sensor as an hot wire anemometer, the sensitive part of the fiber (the MM section) needs to be maintained at a fixed high temperature. We have thought of heating up this part of the fiber by coupling a high power at the input in parallel with the broadband light. The offset at the splicing guarantees a high portion of the power to be coupled and scattered in the cladding of the MM fiber. We have also deposited a graphite layer at the outer

surface of the cladding, in order to increase the absorption of the laser light in the surface of the MM fiber. Fig. 5.9 shows the configuration setup of the fiber based anemometer.

Through this configuration we have been able to increase the temperature of the

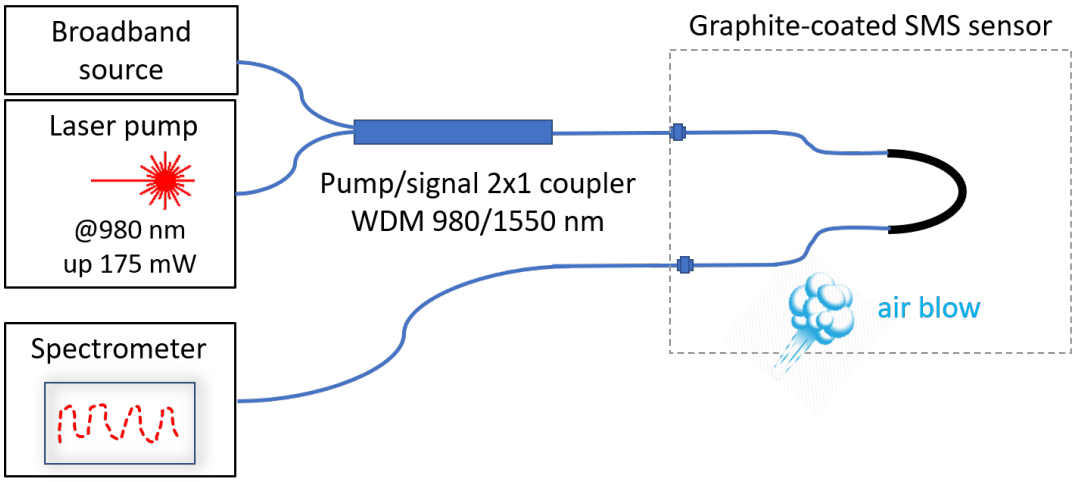

Figure 5.9: Schematic illustration of the OF SMS based hot wire anemometer.

fiber from 25.1 °C to 25.9 °C by applying up to 175 mW of laser power at 980 nm. Tab. 5.1 shows the temperature of the graphite coated MM fiber section with respect to the laser pump power. The power absorption of the graphite layer is definitely a process to be optimized, however 1 °C is enough to prove the concept of the anemometer.

Table 5.1: Pump laser power and the respective temperatures of the MM fiber section.

Laser Power [mW]	0	53.2	121	175
Temperature [°C]	25.1	25.4	25.7	25.9

After the SMS sensor is brought to a stable situation with a higher temperature than the room one, we have tried our conceptual anemometer by blowing air towards the sensitive part of the fiber. We have blown at a flow rate of around 6 L/min and the results are plotted in the graph of Fig. 5.10. From the figure, it can be clearly seen that the spectrum red-shifts 1 nm when the laser pump is turned on at the maximum power. Even though the external temperature increment introduced by the laser pump was only 1 °C, the spectrum shifts quite more than just 50 pm. This can be explained that the fiber itself has absorbed quite a lot of energy, not only due to the graphite layer, but also due to the misalignment in the splicing. Nevertheless when air is blown to the sensitive area the spectrum blue

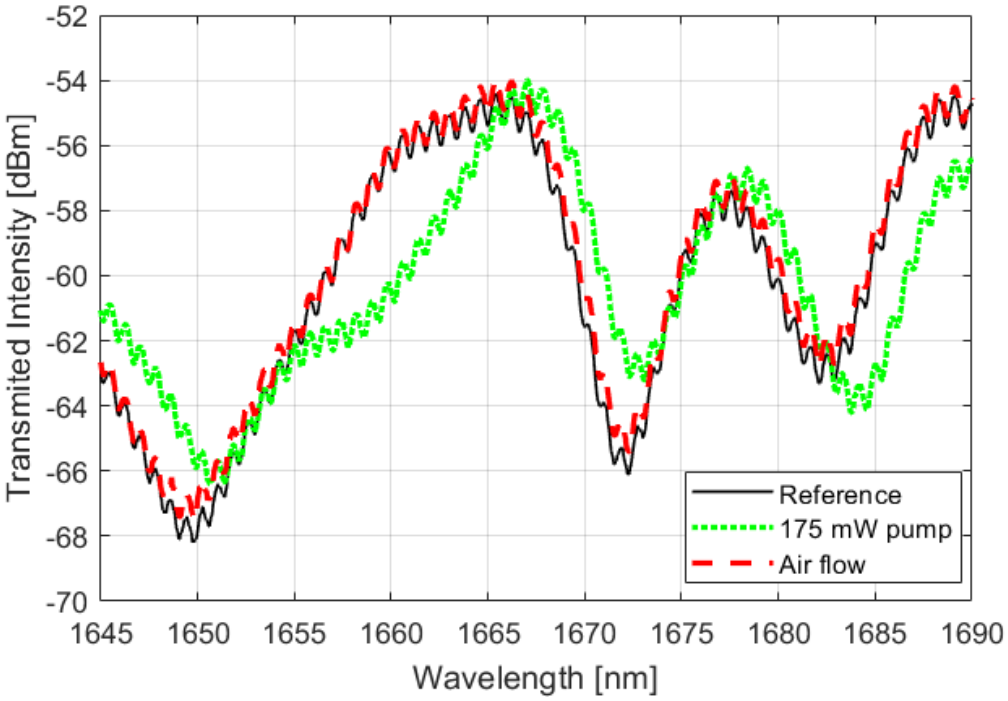

Figure 5.10: Graphic illustration of the interference pattern shift when exposed to air flow.

shifts tending to return to its reference level.

As previously mentioned, these experiments where designed and carried out with the only scope, to prove the concept of a fully optical hot wire anemometer. The results are quite promising, and applicable also to water flow rate measurements. More research is required in metrological terms for the full calibration of the sensor. Moreover, in case we would want to exploit this sensors together with our OFSPR based refractometer, a lot of work has to be done towards a lower cost setup.

Chapter 6

Conclusions

Exploiting their well known advantages, OF sensors have found applications in several domains covering different biomedical and industrial fields. Our sensors are targeted for the potable water quality monitoring, an emergent problem involved also among the UN sustainable development goals (SDG6) to be resolved worldwide within 2030. Some shocking facts about the water situation are mentioned in the Introduction, and I believe the problem is so clear that there is no need to be repeatable. As a matter of fact, in Albania, my country, located in Europe not that far from Italy, with plenty of water reserves, as for 2020 people do not have potable water flowing at their homes continuously. Nevertheless, this desperate situation has served to us as a motivation to give our contribution with our expertise and possibly to get a step closer to probable solution.

The main aim of this project has been to shed some light on optical fiber sensors in metrological terms. Optical fibers have been in the telecommunications market since a long time now, and simultaneously have been exploited for their sensing capabilities. They have some outstanding characteristics that bring them to the front compared to other sensing techniques, and for this reasons they have got a lot of attention from the scientific community. Generally optical fiber sensors are characterized by small dimension, immunity to electromagnetic disturbances, robustness towards harsh environments able to provide real time response, configurable to perform remote and distributed sensing. Moreover with the fast progress on the telecommunication field, nowadays optical fiber based systems can come up with relatively low cost. These three sentences in one way or another can be found in the introduction of any document related to optical fiber sensors, being them scientific articles, conference proceedings, books, reviews, or even dissertations like this one. Definitely those sentences are so true that nobody can disagree about them, nonetheless there are some questions that come to everyone's mind once presented a long list of benefits and features. **"Why are optical fiber sensors not so popular in the sensors market?"** or better **"Is there also a list of**

drawbacks which is not being shown, that holds this technology far from the hall of fame?"

With no doubt the answer to the above mentioned questions is not straightforward as the discussion moves out of the scientific coverage, more towards market, business and finance. Still the two topics cannot be totally separated form one another. The biggest part of my work during this period has been focused on a plasmonic optical fiber based sensor, trying to understand the behavior of the sensors as close as possible to real applications, making a cost performance analysis. Referring to the technology readiness level (TRL) scale, we tried to move from TRL-3 proof of concept level towards TRL-4 and TRL-5, thus a technology validated in lab and in relevant environment.

The sensor has proved its high performance when exploited as a real time refractomter for liquids. Several setup configurations have been designed, prototyped and tested, analyzing the cost performance tradeoff both in short term and long term measurements. We have shown that temperature is the biggest parasitic effect introduced, and special care needs to be taken especially in low cost setups, based on narrow-band LEDs. Tab. 6.1 summarizes the performance of the considered three configurations for the OFSPR sensor. The last row of the table gives an

Table 6.1: Summary of OFSPR setup configurations; cost - performance analysis

	White LED Spectrometer	**White LED Selective PDs**	**Red LED Single PD**
std (1 min)	$8.7 \times 10^{-6} RIU$	$1.0 \times 10^{-5} RIU$	$9.2 \times 10^{-5} RIU$
1 hour stability	$8.4 \times 10^{-5} RIU$	-	$6.8 \times 10^{-3} RIU$
24 hour stability	$3.2 \times 10^{-4} RIU$	-	$1.3 \times 10^{-2} RIU$
temp. effect (δ_n/δ_T)	$1.0 \times 10^{-4} RIU/°C$	$1.0 \times 10^{-4} RIU/°C$	$4.0 \times 10^{-3} RIU/°C$
Est. Cost	6000 €	600 €	6 €

approximate idea about the cost of the interrogation setups exploited in each case, where we include the source and the detector. The cost of the sensor is not included as it is prone to change in an economy of scale, nevertheless it would be the same for all of them. Neither the cost of the computational analysis is not considered, as during the experiments we have exploited personal computers which can easily be replaced by means of micro-controllers with relatively lower costs in the future.

The configurations I have presented in this thesis are pretty plain and straightforward and this has been done on purpose. There is a lack of information in literature about the metrological aspects of OFSPR sensors and there is no point

in over complicating the setup or the computational analysis prior to understanding and knowing in details the existing method. Definitely there is a lot of space for improvements in our setups and in our designed sensors as well. One of the possible improvements has been introduced in Section 3.4 of Ch. 3. Adding a silica nano-layer on top of the metal layer of our sensor has been proven to improve the robustness, resilience, and moreover the performance in metrological terms of our sensor. Whether for long term measurements we have noticed the necessity for a temperature compensation technique. Temperature change gives rise to the thermo-optic effect of the liquid under test, which is in the order of $-1\times10^{-4}RIU/°C$ which in case of contamination analysis, a decrease of the temperature by $1°C$ has the similar effect of 1 ppm of extra chlorine in water [4]. Moreover in the intensiometric approach, temperature compensation is required also for the source, whose intensity is directly related to the environmental temperature. For this reason we have proposed a "middle range solution" analyzing the intensity in several points of the spectrum both on the left and on the right side of the SPR notch. Other fiber based techniques can be used for temperature measurement and compensation, and this has been our motivation to carry out some work also on the SMS sensors.

In parallel with the plasmonic sensors, we started to work on an interferometric based optical fiber sensor which we brought up to a proof of concept level (TRL-3). I have included all the essential information regarding the SMS sensor on a single separate chapter Ch. 5. This choice is done on purpose to let the reader deep dive into each topic without loosing the focus and getting confused between two sensors that work based on different principles. The SMS sensor has been proven to be very sensitive to ambient temperature variations, specifically 5 times more sensitive than FBGs, which hold the state of the art for OF temperature sensing. The SMS sensors can be exploited as stand alone temperature sensors, or exploited together with the OFSPR for temperature compensation purpose. By modifying a little bit the configuration setup, the same sensor can be exploited as an hot wire anemometer to measure the flow rate of a flowing fluid. We have performed proof of concept level experiments, and have proved the feasibility of such setup by demonstrating the sensitivity of the sensor towards the flow rate of blown air. The same principle can exploited to sense a flowing liquid, and like this combined with our plasmonic sensor we can have a sensing probe which gives information about the RI, and the temperature or flow rate of the water within a water distribution system.

This dissertation comes as the final testimony of my last three and a half years of working as a Ph.D. candidate at the Polytechnic University of Turin. The document's aim was to cover in a summarized way the most relevant activities carried out during this period, but in the same time following a logic flow which we have

tried to go along with during our work progress. Nevertheless the thesis is organized in traditional chapters separating the theory from the simulations and the experiments, the activities of which in reality have not necessarily followed the same chronology of actions as described in this thesis. Definitely there are activities which might have been carried out simultaneously, however in this thesis are described in different sections, as there are some other activities which are totally excluded from this thesis because their aim has been just to prove us right or wrong. In general I have tried to be as inclusive as possible when it comes to the topics that have been discussed along the performed work, sometimes even opening questions which need further investigations, or even cases that due to technical reasons have provided limited results.

Definitely, this work leaves space to further development, both vertically in terms of deepening the technical analysis, improving the performance of the sensors, decreasing the cost of the setups but also horizontally, trying to explore the possibilities of implementing the same sensing techniques in various different fields, which can be either biomedical or industrial. Science is more attractive when interdisciplinary field merge together for a unique purpose. A lot of work has to be done also towards commercialization of such research projects. Plasmonics (including SPR and LSPR) is by know a well known phenomenon among the scientific communities, and hundreds of papers get published every year with advancements in the field, nevertheless the commercial applications are still very few.

All in all I must say that as in most of the research projects there is never enough time to conclude, as while we get close to an end, the end gets further away, and this strange but beautiful phenomenon is confirmed also by this project.

Appendix A

OFSPR Sensor Preparation

This dissertation is mainly focused on the OFSPR sensors working principle, the simulation of the mathematical model and on the experimental work performed for the characterization of sensors. Nonetheless, between the simulation process and the experimental characterization there is another very important experimental worked performed in order to prepare the sensors. The activity for the sensor preparation is mainly carried out in the clean room laboratory environments of Convergent Photonics - Prima Electro S.p.A, an industrial company in the market of high power lasers.

This appendix will focus exactly on the sensor preparation process, which is somehow delicate and requires quite some attention. The completed process can be divided in two macro-tasks:

1. Fiber Preparation: Exposure of the core of the optical fiber in small section (few cm) in the middle of the fiber.

2. Metal layer deposition: Process performed in the clean room environments, in order to enable the sensitive area of the fiber.

Optical fibers of core diameter 200 µm, 400 µm and 600 µm with TECS cladding were purchased from Thorlabs. The fibers have a length of 50-100 cm, with the sensitive in the middle, such that both the ends are long enough to make further connections. Both the coating and the cladding of the fibers need to be removed for the core to be exposed. Firstly the section of interest of the fiber is immersed in acetone for some minutes. This process softens a bit the hard plastic coating. Then each fiber is stripped with a calibrated mechanical stripper trying to stay within a limit of few cm. Finally another round of cleaning with acetone has been performed to fully remove the cladding in the area of interest.

Fig. A.1 shows the final result of a 400 micron fiber photographed under a microscope, in the transition section where the cladding is still there and where the

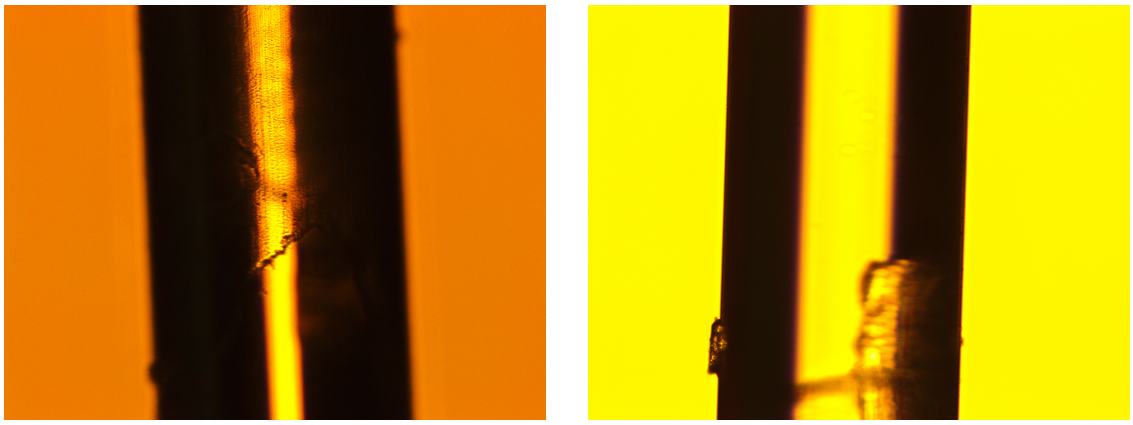

Figure A.1: Coating and Cladding removal of a 400 micron core fiber

cladding is totally removed. After all the fibers have passed through the above described process they are brought in the clean room environment ready for the deposition process. The instrument exploited for the deposition process is called "Temescal BJD-2000 Bell Jar Deposition System". The fibers are placed in a metallic holders with a ring shape adaptive to the deposition system. The process overall process can be divided in few micro-steps:

1. Stick the fibers to the metallic ring holders.
2. Load the rings containing the fibers in the deposition system
3. Start the process by setting the instrument to reach "medium vacuum" condition
4. Deposition of 20 nm of Titanium.
5. Deposition of 40 nm of Gold
6. Relaxation of the vacuum chamber.
7. Rotate the metallic ring holder to start deposition on the other side.
8. Repeat the sequence from point 3 to point 6.
9. Remove the fibers from the holders, sensors are ready.

Photos in Fig. A.2 are taken before the deposition process has started. The image on the right shows the fibers placed (duct taped) in the metallic holder, and the image on the left shows the instrument before the capsule gets closed to start step 3 explained above.

The chamber requires around 2 hours to reach the ideal vacuum level. The

Figure A.2: Photos taken before the deposition process

deposition process starts firstly with a 20 nm thick layer of titanium (Ti) with deposition rate 1 Å/s, thus a total time of 200 seconds. Immediately after the 40 nm thick Gold (Au) layer is deposited with a deposition rate of 3 Å/s for around 150 seconds. The resulted deposition thickness measured by an internal quartz crystal micro-balance (QCM) was 20.9 nm of Ti and 40.4 nm of Au. The deposition process itself is relatively short, nevertheless overall the process requires around 6 hours counting twice the time to reach vacuum condition, twice the time for the chamber relaxation (20-30 minutes) and the time required to load the chamber.
The thicknesses of the metal layers is selected by observing at the simulation results presented in Chapter 3 and experimental works already presented in the literature [24]. An important fact to be kept in mind in our process is that the deposition process is not uniformly done around the core of the fiber. Rather than that, the deposition results more as an elliptical shape around the fiber depositing on two opposite sides 60 nm of metal layer, and perpendicular to them almost 0. Fig.A.3 illustrates schematically and out of scale how the fiber's cross section looks like. Instead Fig. A.4 shows a photo of an OFSPR sensor produced on a 400 micron core fiber. The effective sensitive length is around 3.2 cm. Velazquez et al. discuss the feasibility of the idea of non uniformly deposited fibers. In their article [52] they experimentally compare the two sides symmetrically deposited sensor, with a one side deposited one and a uniformly deposited one. By that time we had also reached in the same conclusion that two sided symmetrical deposition works perfectly fine in practical situation and reduces the complexity of the sensor preparation process.

It is recommended to place fibers of the same dimension in the same metallic holder in order for the stress of the holder on the fibers is uniformly distributed and the fibers not to torque when the fiber is bent to fit within the chamber. However even though special care is taken in every step of the process the produced sensors do not provide repeatable SPR spectra when characterize. The only non fully

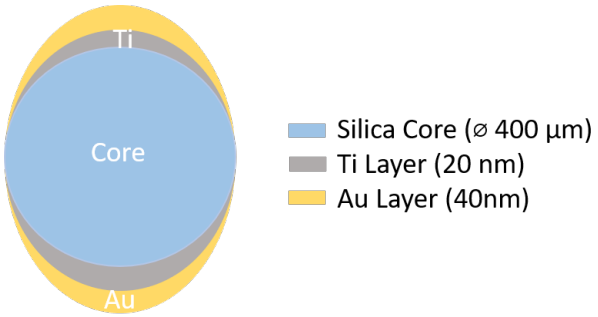

Figure A.3: Schematic illustration of the non uniform deposited metal layers (out of scale).

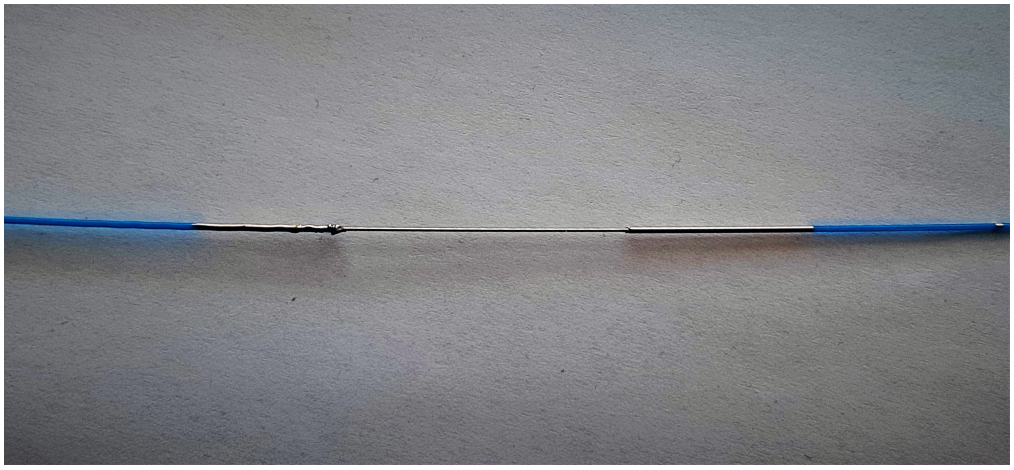

Figure A.4: Photo of the sensitive are of a OFSPR sensor produced on a 400 micron core fiber.

repeatable action along the process is the mechanical stripping of the coating and cladding of the fiber. As it is performed manually, the exposed length generally happens to be longer than the targeted one. Appendix B will throw some light on the characterization process of the sensors in wavelength interrogation technique.

Appendix B

Sensors' Characteristics

This appendix will be focused on the characteristics of the sensors produced in a unique deposition process. Generally the sensors are characterized in wavelength interrogation in different RIs realized by mixing water and isopropanol at different concentrations. Nonetheless in the figures B.1, B.2 and B.3 in this appendix are shown only 2 curves for each sensor, one obtained while the sensor is immersed in water and the other while the sensor is immersed in isopropanol. The sensors have all the same core diameter of 400 micron but have sensitive lengths varying in the range of 3 to 6 cm. Even though the sensors are produced in the same process the plots show that the curves are not identical, thus either the stripping process or the characterization process is not repetitive in terms of quality assurance.

The experiments are carried out in room temperature condition, exploiting a white LED (MBB1F1 - Thorlabs) at the output and a spectrometer (Avantes, Avaspec - ULS3648) at the output. The final data are saved in an Excel worksheet, imported to MATLAB and analyzed in order to extract the useful information. The sensor is connected to source and spectrometer via mobile SMA connectors with two patch-chords. The mobile connectors are not the ideal solution as they do not guarantee a repetitive process, however once the sensor is connected the situation is stable. Moreover we are interested at the information hidden in the spectrum of the light rather than the intensity.

Table B.1: Characteristics of 12 sensors prepared on 400 micron core fiber.

	S. 1	S. 2	S. 3	S. 4	S. 5	S. 6	S. 7	S. 8	S. 9	S. 10	S. 11	S. 12	Unit
Sensitive Length	32	28	32	48	30	30	30	40	40	60	50	60	mm
Sensitivity	23501	1765	2188	2375	2139	2115	1814	1537	2163	2180	2318	2131	nm/RIU
FWHM	128.5	119.7	128.8	158.4	66.7	92.1	150.6	112.9	67.6	132.7	99.2	146.4	nm
Depth	31.2	32.7	33.4	31.2	13.9	21.6	30.9	21.1	16.6	31.0	22.2	29.7	$\%$
DA	0.24	0.27	0.26	0.19	0.21	0.23	0.20	0.19	0.25	0.23	0.22	0.20	$\%/nm$
FOM	18.29	14.74	16.98	14.98	32.07	22.96	12.04	13.61	31.97	16.42	23.36	14.55	RIU^{-1}
QP	4.45	4.03	4.41	2.95	6.7	5.39	2.47	2.55	7.87	3.84	5.24	2.95	$\%/(nm \times RIU)$

The only difference among the sensors considered in this characterization process

is the sensitive length of each sensor. Nonetheless all the qualitative parameters of the sensors vary quite a lot and the variation has no direct relation to the sensitive length of the sensor.

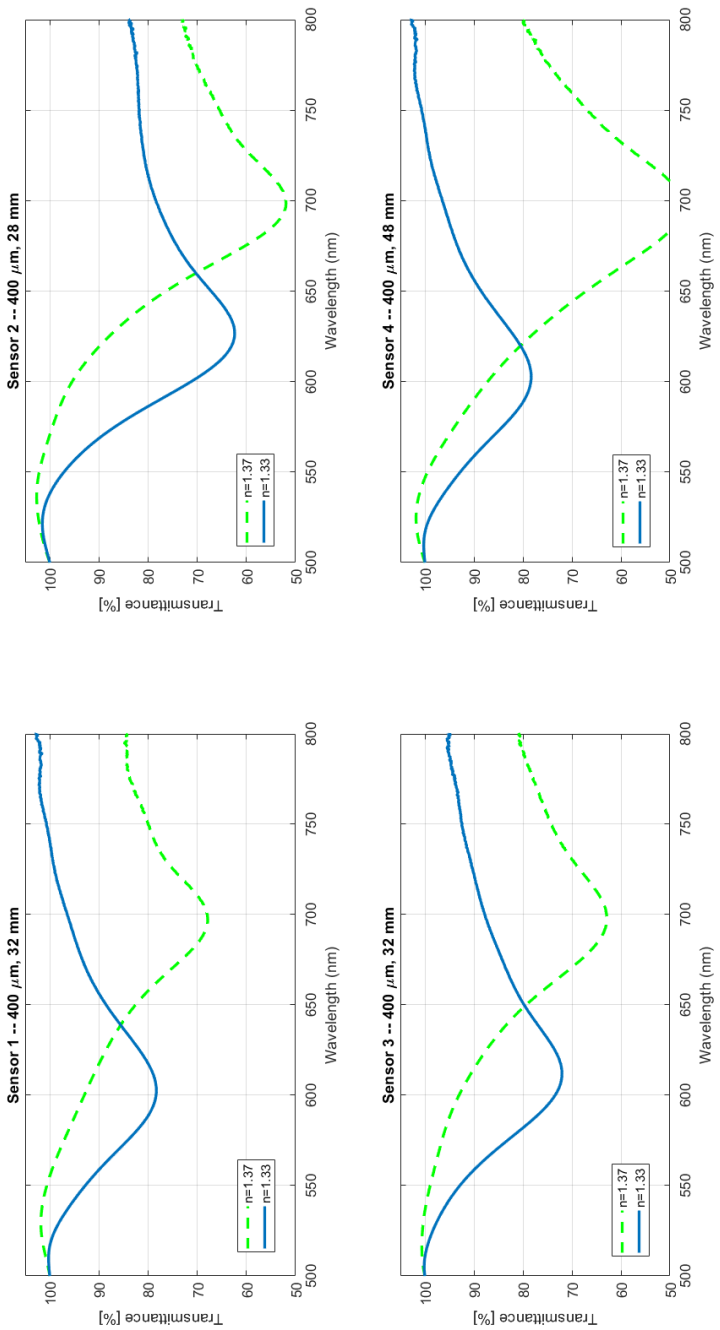

Figure B.1: Experimentally obtained SPR curves of 4 different sensors while immersed in water and isopropanol.

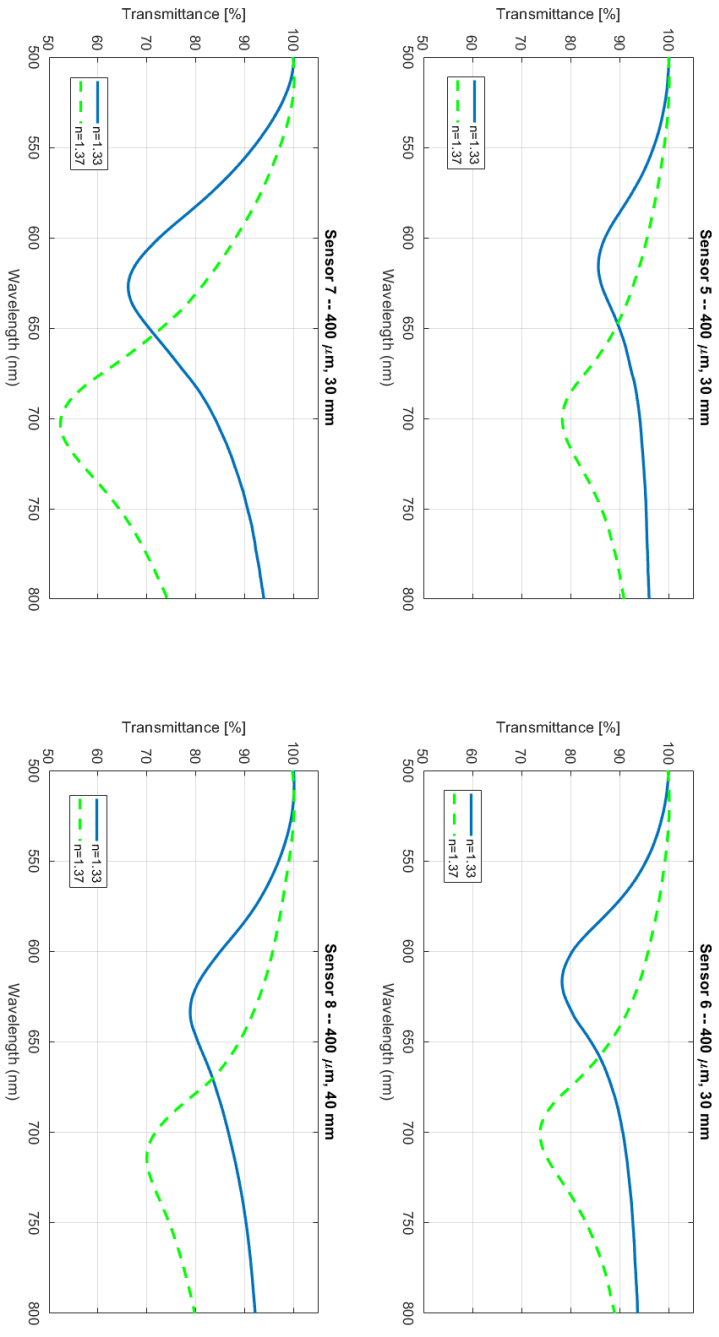

Figure B.2: Experimentally obtained SPR curves of 4 different sensors while immersed in water and isopropanol.

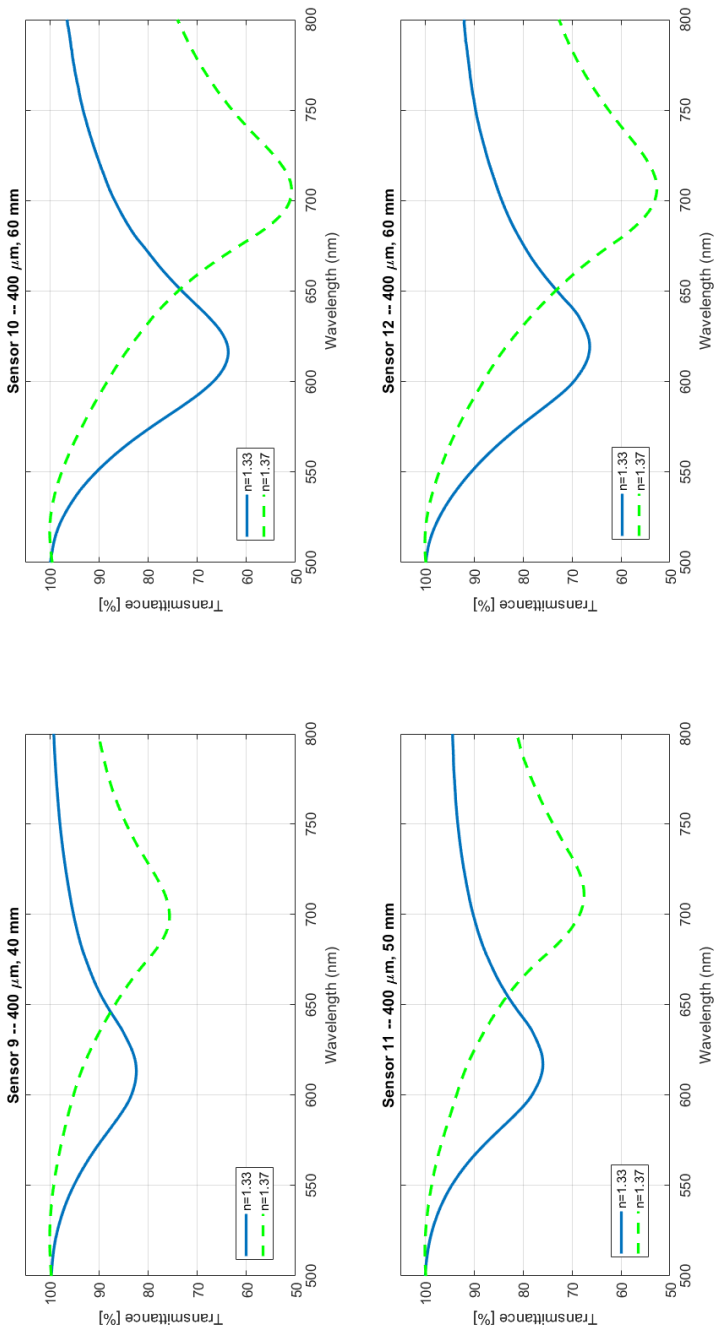

Figure B.3: Experimentally obtained SPR curves of 4 different sensors while immersed in water and isopropanol.

Appendix C

MATLAB Functions

This Appendix covers the MATLAB functions and scripts accompanied with detailed comments exploited for the simulations of the fiber based plasmonic sensors. The first code corresponds to the script where the user is allowed to change the input parameters,

1. The main Script which plots the SPR curves for the respective RI, calculating the main characteristics of each curve.

```
lambda_nm          = linspace (400, 900, 2000);
lambda             = 1e-9.* lambda_nm;
n_lambda           = length(lambda);
res                = (lambda_nm(end) - lambda_nm(1))/ n_lambda
    ; % resolution
c                  = 299792458; % Light speed

%% Input variables
fiber_type         = 's';        % s=silica , p=pmma
NA                 = 0.39;
l_sens             = 0.03;       % sensitive length m
d_core             = 400*10^-6; % core diameter m
W_TM               = 0.5;        % Polarization of input light
    (50% => non-polarized)

n_layers           = 4;          % 1.core || 4.Ti || 2.Au || 5.
    SiO2 || 3.water
th_Ti              = 20;         % Ti thickness nm
th_Au              = 40;         % Au thickness nm
th_Sio2            = 15;         % SiO2 thckness nm
```

```
18 [n,th]           = nth_profile(n_layers, lambda, fiber_type,
       th_Ti, th_Au, th_Sio2); % creates a matrix with
       corresponding RIs and thicnkesses
19 power_distr_law = 'n';        % n=normal, i= inverted, c=
       constant
20 %dn               = 0;
21 dn                = [0 0.0043 0.0086 0.0172];
22
23
24 %% Calculate the reference (sensor is sorrunded by air)
25 n(:, n_layers) = n_air(lambda); % add the external medium (
       air)
26 [Ptot_air]      = multiple_refl (power_distr_law, NA,...
27           lambda, th, W_TM, d_core, l_sens, n);
28
29
30 endloop         = length(dn); % preallocation
31 depth(endloop) = 0;
32 fwhm(endloop)  = 0;
33 DA(endloop)    = 0;
34 peaks(endloop) = 0;
35
36 %% Plot of the SPR spectra for each dn
37 figure
38  for ii=1:endloop
39       n(:,n_layers) = n_water(lambda,25) + dn(ii);
40       [Ptot_water]  = multiple_refl (power_distr_law, NA,...
41            lambda, th, W_TM, d_core, l_sens, n);
42
43       SPR_plot      = 100* Ptot_water./ Ptot_air;
44       depth(ii)     = max(SPR_plot) - min(SPR_plot);
45       hdepth        = 100-depth(ii)/ 2;
46       [temp,index]  = find(SPR_plot<hdepth);
47       fwhm (ii)     = (index(end)-index(1))* res;
48       DA (ii)       = depth/ fwhm; % Detection accuracy
49       [minimum, m]  = min (SPR_plot);
50       peaks(ii)     = lambda_nm(m);
51
52       plot(lambda_nm, SPR_plot, 'r')
53       ylim ([50 110])
54       xlim ([500 800])
55       hold on
```

```
56        grid on
57        title('SPR Transmission plot')
58        ylabel('Transmission intensity [%]')
59        xlabel('Wavelength [nm]')
60    end
61
62    S   =diff(peaks)./ diff(dn); % Sensitivity
63    FOM = S(1)/fwhm(1);          % Figure of Merit
64    QP    = FOM * DA(1);         % Quality Parameter
```

2. The function which considers the multiple reflections within the sensitive length of the fiber.

```
1  function [Ptot] = multiple_refl (power_distr_law, NA,
       lambda, th, W_TM, d_core, l_sens, n)
2      format long
3
4      teta_accept_max = asind(NA);
5      teta_air_core   = linspace (0, teta_accept_max, 100); %
           acceptance angle
6
7      if (teta_air_core(1) == 0)
8          teta_air_core(1) = 0.000001;
9      end
10
11     W_TE    = 1-W_TM;
12     endloop = length (teta_air_core);
13     Ptot    = 0;
14
15     if (power_distr_law == 'n')    % normal law
16         P_in          = tand(max(teta_air_core))/ ((cosd(
               max(teta_air_core)))^2); % the power section
               carried by angles
17         y             = P_in.* ((sind(teta_air_core+45).*
               cosd(teta_air_core+45))+0.5);
18         power_distrib = y./sum(y); % Normalize to integral
               = 1
19
20     elseif  (power_distr_law == 'i') % inverted law
21         power_distrib = tand(teta_air_core)./((cosd(
               teta_air_core)).^2);
```

```
22          power_distrib = power_distrib./sum(power_distrib);
              % Normalize (P tot =1)
23          for step = 1: floor(endloop/2)
24              tmp1 = power_distrib(step);
25              power_distrib(step)= power_distrib(endloop - (
                    step-1));
26              power_distrib(endloop - (step-1))= tmp1;
27          end
28
29      elseif (power_distr_law == 'c') % Costant
30          for step = 1: endloop
31              power_distrib(step) = 1/endloop ;
32          end
33      end
34
35  for step = 1: endloop
36      [Rs_step, Rp_step, teta_core_metal_range] = single_refl
            (teta_air_core(step), lambda, th, n);
37      % Core-Metal angle is calculated over every single
            wavelength
38
39      length_lambda    = length (teta_core_metal_range);
40      teta_core_metal = teta_core_metal_range(floor(
            length_lambda/2));
41
42      % Polarization is maintained, Nref can be also non
            integer.
43      Nrefl  = l_sens./ (d_core.* tand(teta_core_metal));
44
45      P_step = ((W_TE* (Rs_step.^Nrefl) + W_TM* (Rp_step .^
            Nrefl))* power_distrib(step));
46      Ptot = Ptot + P_step;
47
48  end
49
50  end
```

2. The function which calculates the reflectivity of a multilayered structure.

```
1  function [Rs, Rp, teta_core_metal_range] = single_refl(
       teta_air_core, lambda, th, n)
```

```
2
3  format long
4
5  [n_lambda, n_layers] = size(n);
6  th                   = th*10^-9;
7  Z0                   = 376.7303;
8
9  % pre-allocate variables for faster simulation
10 k0(n_lambda)                          = 0;
11 kx(n_lambda)                          = 0;
12 k(n_layers)                           = 0;
13 kz(n_lambda, n_layers)                = 1+1i;
14 Z_TE(n_lambda, n_layers)              = 1+1i;
15 Z_TM(n_lambda, n_layers)              = 1+1i;
16 p_TE(n_lambda, n_layers-1)            = 1+1i;
17 p_TM(n_lambda, n_layers-1)            = 1+1i;
18 gamma_TE(n_lambda, n_layers-1)        = 1+1i;
19 gamma_TM(n_lambda, n_layers-1)        = 1+1i;
20 teta_core_metal_range(n_lambda)       = 0;
21 Rs(n_lambda)                          = 0;
22 Rp(n_lambda)                          = 0;
23
24 % Calculate paramters with respect to wavelength
25 for i = 1:n_lambda
26
27     %different wavelength => different RI => different
       angle of
28     %incidence in glass/metal interface
29     %n(i,1) refractive index of core wrt lambda
30     teta_core_metal_range(i) = acosd(sind(teta_air_core)*
       (1/n(i, 1)));
31
32     %calculate propagation constants and characteristic
       impedance in each layer
33     % kx is the same in all media
34     k0(i) = 2* pi/ lambda(i);
35     kx(i) = k0(i)* n(i, 1)* sind(teta_core_metal_range(i));
36
37     for h = 1:n_layers
38         k(h)       = k0(i)* n(i, h);
39         kz(i, h)   = kz_const(k(h), kx(i));
40         Z_TE(i, h) = Z0* k0(i)/ kz(i, h);
```

```
41          Z_TM(i, h) = (Z0* kz(i, h))/ (k0(i)* (n(i, h)^2));
42      end
43
44      %calculate the elementary reflection coefficients "rho"
            between
45      %each two consecutive layers
46      for h = 1:(n_layers-1)
47          p_TE(i, h) = (Z_TE(i, (h+1)) - Z_TE(i, h))/ (Z_TE(i
                , (h+1)) + Z_TE(i, h));
48          p_TM(i, h) = (Z_TM(i, (h+1)) - Z_TM(i, h))/ (Z_TM(i
                , (h+1)) + Z_TM(i, h));
49      end
50
51      %calculate the reflection coefficients of the multi-
            layered structure
52      gamma_TE(i, (n_layers-1)) = p_TE(i, (n_layers-1));
53      gamma_TM(i, (n_layers-1)) = p_TM(i, (n_layers-1));
54      temp                      = n_layers-2;
55
56      while(temp >= 1)
57          gamma_TE(i, temp) = reflection_coeff(p_TE(i, temp),
                ...
58              gamma_TE(i, (temp+1)), kz(i, temp+1), th(temp+1))
                    ;
59          gamma_TM(i, temp) = reflection_coeff(p_TM(i, temp),
                ....
60              gamma_TM(i, (temp+1)), kz(i, temp+1), th(temp+1))
                    ;
61          temp              = temp - 1;
62      end
63
64      Rs(i) = (abs(gamma_TE(i, 1))^2);    % Reflectivity s-
            polarized wave
65      Rp(i) = (abs(gamma_TM(i, 1))^2);    % Reflectivity p-
            polarized wave
66  end
67  end
```

Bibliography

[1] Unicef/WHO. *Progress on household drinking water, sanitation and hygiene 2000-2017: Special focus on inequalities*. 2019. URL: https://www.who.int/water_sanitation_health/publications/jmp-report-2019/en/.

[2] Meena Palaniappan et al. *Clearing the waters: a focus on water quality solutions*. 2010.

[3] Fourth Edition. "Guidelines for drinking-water quality". In: *WHO chronicle* 38.4 (2011), pp. 104–8.

[4] WYW Yusmawati and W Mahmood Mat Yunus. "Optical properties and kinetic behavior of chlorine in pure water and swimming pool water using surface plasmon resonance technique". In: *American Journal of Applied Sciences* 4.12 (2007), pp. 1024–1028.

[5] Anuj K Sharma and BD Gupta. "Theoretical model of a fiber optic remote sensor based on surface plasmon resonance for temperature detection". In: *Optical Fiber Technology* 12.1 (2006), pp. 87–100.

[6] Ernst Abbe. *"U on the determination of the refraction ratios ä of solid bodies using the refractometer*. 1879.

[7] Daniel Colladon. "Sur les réflexions d'un rayon de lumière à l'intérieur d'une veine liquide parabolique". In: *Comptes rendus* 15.1800 (1842).

[8] John Tyndall. "Total Reflexion". In: *Notes about Light* (1870).

[9] Jeff Hecht. *City of light: the story of fiber optics*. Oxford University Press on Demand, 2004.

[10] Dong Wang et al. "Ultra-low-loss and large-effective-area fiber for 100 Gbit/s and beyond 100 Gbit/s coherent long-haul terrestrial transmission systems". In: *Scientific reports* 9.1 (2019), pp. 1–7.

[11] Xiaoyi Bao, David J Webb, and David A Jackson. "32-km distributed temperature sensor based on Brillouin loss in an optical fiber". In: *Optics letters* 18.18 (1993), pp. 1561–1563.

[12] Claude Belleville and Gaetan Duplain. "White-light interferometric multimode fiber-optic strain sensor". In: *Optics letters* 18.1 (1993), pp. 78–80.

[13] Kiyoshi Komoriya and Eiinei Oyama. "Position estimation of a mobile robot using optical fiber gyroscope (OFG)". In: *Proceedings of IEEE/RSJ International Conference on Intelligent Robots and Systems (IROS'94)*. Vol. 1. IEEE. 1994, pp. 143–149.

[14] Chun-Fan Chan et al. "Optical fiber refractometer using narrowband cladding-mode resonance shifts". In: *Applied optics* 46.7 (2007), pp. 1142–1149.

[15] Alessio Stefani et al. "High sensitivity polymer optical fiber-Bragg-grating-based accelerometer". In: *IEEE Photonics Technology Letters* 24.9 (2012), pp. 763–765.

[16] Shaorui Gao et al. "All-optical fiber anemometer based on laser heated fiber Bragg gratings". In: *Optics express* 19.11 (2011), pp. 10124–10130.

[17] Valérie Voisin et al. "Highly sensitive detection of molecular interactions with plasmonic optical fiber grating sensors". In: *Biosensors and Bioelectronics* 51 (2014), pp. 249–254.

[18] CR Zamarreño et al. "Optical fiber pH sensor based on lossy-mode resonances by means of thin polymeric coatings". In: *Sensors and Actuators B: Chemical* 155.1 (2011), pp. 290–297.

[19] Lukas Novotny and Bert Hecht. *Principles of nano-optics*. Cambridge university press, 2012.

[20] Anatoly V Zayats, Igor I Smolyaninov, and Alexei A Maradudin. "Nano-optics of surface plasmon polaritons". In: *Physics reports* 408.3-4 (2005), pp. 131–314.

[21] Erwin Kretschmann and Heinz Raether. "Notizen: radiative decay of non radiative surface plasmons excited by light". In: *Zeitschrift für Naturforschung A* 23.12 (1968), pp. 2135–2136.

[22] Andreas Otto. "Excitation of nonradiative surface plasma waves in silver by the method of frustrated total reflection". In: *Zeitschrift für Physik* 216.4 (1968), pp. 398–410.

[23] Yuzhi Chen et al. "Experimental comparison of fiber-optic surface plasmon resonance sensors with multi metal layers and single silver or gold layer". In: *Plasmonics* 10.6 (2015), pp. 1801–1808.

[24] Hitoshi Suzuki et al. "Effects of gold film thickness on spectrum profile and sensitivity of a multimode-optical-fiber SPR sensor". In: *Sensors and Actuators B: Chemical* 132.1 (2008), pp. 26–33.

[25] Yusser Al-Qazwini et al. "Refractive index sensor based on SPR in symmetrically etched plastic optical fibers". In: *Sensors and Actuators A: Physical* 246 (2016), pp. 163–169.

[26] Joel Villatoro, David Monzón-Hernández, and Efrain Mejia. "Fabrication and modeling of uniform-waist single-mode tapered optical fiber sensors". In: *Applied optics* 42.13 (2003), pp. 2278–2283.

[27] Nunzio Cennamo et al. "Easy to use plastic optical fiber-based biosensor for detection of butanal". In: *PLoS One* 10.3 (2015), e0116770.

[28] Christophe Caucheteur, Valérie Voisin, and Jacques Albert. "Near-infrared grating-assisted SPR optical fiber sensors: design rules for ultimate refractometric sensitivity". In: *Optics Express* 23.3 (2015), pp. 2918–2932.

[29] Yong Zhao et al. "Smart hydrogel-based optical fiber SPR sensor for pH measurements". In: *Sensors and Actuators B: Chemical* 261 (2018), pp. 226–232.

[30] Anuj K Sharma and Baljinder Kaur. "Chalcogenide fiber-optic SPR chemical sensor with MoS2 monolayer, polymer clad, and polythiophene layer in NIR using selective ray launching". In: *Optical Fiber Technology* 43 (2018), pp. 163–168.

[31] Anuj K Sharma, Baljinder Kaur, and Vasile A Popescu. "On the role of different 2D materials/heterostructures in fiber-optic SPR humidity sensor in visible spectral region". In: *Optical Materials* 102 (2020), p. 109824.

[32] Katarzyna Gasior et al. "Fiber-optic surface plasmon resonance sensor based on spectral phase shift interferometric measurements". In: *Sensors and Actuators B: Chemical* 257 (2018), pp. 602–608.

[33] Kort Bremer and Bernhard Roth. "Fibre optic surface plasmon resonance sensor system designed for smartphones". In: *Optics express* 23.13 (2015), pp. 17179–17184.

[34] Yun Liu et al. "Surface plasmon resonance biosensor based on smart phone platforms". In: *Scientific reports* 5 (2015), p. 12864.

[35] Yogendra S Dwivedi, Anuj K Sharma, and Banshi D Gupta. "Influence of skew rays on the sensitivity and signal-to-noise ratio of a fiber-optic surface-plasmon-resonance sensor: a theoretical study". In: *Applied optics* 46.21 (2007), pp. 4563–4569.

[36] Dalibor Ciprian and Petr Hlubina. "Theoretical model of the influence of oxide overlayer thickness on the performance of a surface plasmon fibre-optic sensor". In: *Measurement Science and Technology* 24.2 (2013), p. 025105.

[37] BD Gupta and CD Singh. "Evanescent-absorption coefficient for diffuse source illumination: uniform-and tapered-fiber sensors". In: *Applied optics* 33.13 (1994), pp. 2737–2742.

[38] Yu Xu et al. "Analytical estimates of the characteristics of surface plasmon resonance fibre-optic sensors". In: *Journal of Modern Optics* 47.6 (2000), pp. 1099–1110.

[39] M Kanso, Stéphane Cuenot, and G Louarn. "Sensitivity of optical fiber sensor based on surface plasmon resonance: modeling and experiments". In: *Plasmonics* 3.2-3 (2008), pp. 49–57.

[40] Rana Tabassum and Banshi D Gupta. "SPR based fiber-optic sensor with enhanced electric field intensity and figure of merit using different single and bimetallic configurations". In: *Optics Communications* 367 (2016), pp. 23–34.

[41] Anuj K Sharma and BD Gupta. "On the sensitivity and signal to noise ratio of a step-index fiber optic surface plasmon resonance sensor with bimetallic layers". In: *Optics Communications* 245.1-6 (2005), pp. 159–169.

[42] Jose V Herráez and R Belda. "Refractive indices, densities and excess molar volumes of monoalcohols+ water". In: *Journal of Solution Chemistry* 35.9 (2006), pp. 1315–1328.

[43] Benjawan Kjornrattanawanich et al. "Temperature dependence of the EUV responsivity of silicon photodiode detectors". In: *IEEE transactions on electron devices* 53.2 (2006), pp. 218–223.

[44] PL Fulmek et al. "Time dependent and temperature dependent properties of the forward voltage characteristic of InGaN high power LEDs". In: *AIP Advances* 7.3 (2017), p. 035206.

[45] Carmelo Fallauto et al. "Compensated surface plasmon resonance sensor for long-term monitoring applications". In: *IEEE Transactions on Instrumentation and Measurement* 63.5 (2013), pp. 1287–1292.

[46] Andon Bano et al. "SPR fiber based sensor for long-term monitoring of aqueous media". In: *2018 IEEE International Instrumentation and Measurement Technology Conference (I2MTC)*. IEEE. 2018, pp. 1–6.

[47] Bahaa EA Saleh and Malvin Carl Teich. *Fundamentals of photonics*. john Wiley & sons, 2019.

[48] Luc Thevenaz. *Advanced fiber optics: concepts and technology*. EPFL press, 2011.

[49] Wei Chen et al. "Performance assessment of FBG temperature sensors for laser ablation of tumors". In: *2015 IEEE International Symposium on Medical Measurements and Applications (MeMeA) Proceedings*. IEEE. 2015, pp. 324–328.

[50] Massimo Olivero et al. "Single-mode–multimode–single-mode optical fiber sensing structure with quasi-two-mode fibers". In: *IEEE Transactions on Instrumentation and Measurement* 67.5 (2017), pp. 1223–1229.

[51] Massimo Olivero et al. “Single mode-multimode-single mode optical fiber sensors: Review and application to temperature measurements using a bend-insensitive fiber”. In: *2017 IEEE International Instrumentation and Measurement Technology Conference (I2MTC)*. IEEE. 2017, pp. 1–5.

[52] Jesús Salvador Velázquez-González et al. “Simultaneous measurement of refractive index and temperature using a SPR-based fiber optic sensor”. In: *Sensors and Actuators B: Chemical* 242 (2017), pp. 912–920.